INTEGRATING MULTI-SENSOR EXPERIMENTAL AND NUMERICAL APPROACHES FOR DAMAGE LOCALIZATION AND CRACK PROPAGATION MONITORING IN COMPOSITE LAMINATES

by
IBRAHIM BAHADIR

Submitted to the Graduate School of Engineering and Natural Sciences
in partial fulfilment of
the requirements for the degree of Master of Science
in Manufacturing Engineering

Sabancı University
July 2026

INTEGRATING MULTI-SENSOR EXPERIMENTAL AND NUMERICAL APPROACHES FOR DAMAGE LOCALIZATION AND CRACK PROPAGATION MONITORING IN COMPOSITE LAMINATES

Approved by:

Assoc. Prof. ADNAN KEFAL .....
(Thesis Supervisor)

Asst. Prof. BEKIR DIZMAN .....

Assoc. Prof. BERTAN BEYLERGIL .....

Date of Approval: July 16, 2026

ABSTRACT

INTEGRATING MULTI-SENSOR EXPERIMENTAL AND NUMERICAL APPROACHES FOR DAMAGE LOCALIZATION AND CRACK PROPAGATION MONITORING IN COMPOSITE LAMINATES

IBRAHIM BAHADIR

Manufacturing Engineering, M.Sc. Thesis, July 2026

Thesis Supervisor: Assoc. Prof. ADNAN KEFAL

Keywords: Digital image correlation; Acoustic emission; Composite laminates; Crack propagation; Damage localization

This thesis presents an integrated methodology for damage characterization and crack propagation monitoring in pre-cracked carbon/epoxy composite laminates. To address the numerical sensitivity of full-field optical measurements, a dual-stage smoothing element analysis (SEA) assisted digital image correlation (DIC) methodology is developed to formulate a gradient-enhanced, bounded damage-sensitive localization index. This numerical formulation identifies spatially localized damage zones without relying on constitutive material models. Utilizing a unified experimental campaign on seven composite laminates with varying stacking sequences (0/90/0, 90/0/90, 0/0/0, 90/90/90) and initial crack orientations (45^{o} and 90^{o}), the crack propagation behavior is comprehensively investigated through a multi-instrument approach combining DIC, acoustic emission (AE), and strain gauges. Results demonstrate that the macroscopic mechanical response and microscopic damage evolution are strongly governed by both ply architecture and initial crack angle. Specifically, 0^{o}-dominated laminates exhibit progressive horizontal crack propagation, whereas 90^{o}-dominated laminates display delayed but abrupt vertical fracture. AE clustering analysis identifies two distinct acoustic event populations corresponding to tensile crack-tip activity and high-energy mixed-mode sliding mechanisms. By synthesizing the spatial deformation from DIC, temporal damage activity from AE,

and local mechanical response from strain gauges, the proposed assessment provides a comprehensive evaluation of progressive, delayed, and fracture-dominated damage stages. Ultimately, this thesis establishes a robust, physically consistent basis for monitoring spatial and temporal crack evolution in composite structures.

ÖZET

KOMPOZIT MALZEMELERDE HASAR LOKALIZASYONU VE ÇATLAK İLERLEMESININ İZLENMESINE YÖNELIK ÇOKLU SENSÖR TABANLI DENEYSEL VE SAYISAL YAKLAŞIMLARIN ENTEGRASYONU

IBRAHIM BAHADIR

Üretim Mühendisliği, Yüksek Lisans Tezi, Temmuz 2026

Tez Danışmanı: Doç. Dr. ADNAN KEFAL

Anahtar Kelimeler: Dijital görüntü korelasyonu; Akustik emisyon; Kompozit laminatlar; Çatlak ilerlemesi; Hasar lokalizasyonu

Bu tez, başlangıç çatlağı barındıran karbon/epoksi kompozit laminatlarda hasar karakterizasyonu ve çatlak ilerlemesinin izlenmesi için entegre bir metodoloji sunmaktadır. Tam alan optik ölçümlerin sayısal hassasiyet problemlerini çözmek amacıyla, sınırlandırılmış bir hasar lokalizasyon indeksi oluşturmak için çift aşamalı yumuşatma elemanı analizi (SEA) destekli dijital görüntü korelasyonu (DIC) yaklaşımı geliştirilmiştir. Geliştirilen bu sayısal formülasyon, herhangi bir malzeme modeline ihtiyaç duymadan, kırılma öncesinde oluşan hasar bölgelerini uzamsal olarak tespit edebilmektedir. Bu amaçla üretilen ve farklı dizilim sıralarına (0/90/0, 90/0/90, 0/0/0, 90/90/90) ve çatlak açılarına (45^o ve 90^o) sahip yedi adet kompozit numune kullanılarak ortak bir deneysel çalışma yürütülmüştür. Aynı numuneler üzerinde DIC, akustik emisyon (AE) ve gerinimölçer verilerinin birleştirildiği çoklu enstrümanlı bir yöntemle çatlak ilerleme davranışları kapsamlı biçimde incelenmiştir. Elde edilen bulgular, makroskopik mekanik tepkinin ve mikroskobik hasar gelişiminin hem katman mimarisi hem de çatlak açısına güçlü bir şekilde bağlı olduğunu göstermektedir. 0^o ağırlıklı laminatlarda aşamalı ve yatay yönde bir çatlak ilerlemesi gözlemlenirken, 90^o ağırlıklı laminatlarda kırılma anına kadar belirgin bir hasar göstermeyen, ani ve dikey yönde ilerleyen bir kırılma saptanmıştır. AE kümeleme analizi sayesinde çekme kaynaklı çatlak ucu aktivitesi ile yüksek enerjili

karışık modlu kayma mekanizmalarını temsil eden iki farklı akustik olay popülasyonu tanımlanmıştır. Önerilen bu yaklaşım; DIC tabanlı uzamsal deformasyon, AE tabanlı zamansal hasar aktivitesi ve gerinimölçerlerden alınan yerel mekanik tepkileri sentezleyerek hasar evrelerinin bütüncül bir analizini sunmaktadır. Sonuç olarak bu çalışma, kompozit yapılarda çatlak gelişiminin hem uzamsal hem de zamansal olarak izlenebilmesi için fiziksel açıdan tutarlı ve sağlam bir temel oluşturmaktadır.

ACKNOWLEDGEMENTS

I would like to express my deepest gratitude to my thesis advisor, Assoc. Prof. Dr. Adnan Kefal, for his unwavering support, invaluable guidance, and continuous mentorship throughout the course of this research. His expertise and insightful supervision have played a fundamental role in shaping this study and have provided me with the opportunity to engage deeply with advanced topics in experimental mechanics, structural health monitoring, and composite materials.

I am also profoundly grateful to my girlfriend and my family for their endless encouragement, patience, and support throughout this journey. Their belief in my abilities, together with the sacrifices they have made, has been a constant source of motivation and strength during the most challenging stages of this work.

I would like to extend my sincere thanks to Mahmut Hüdayi Bilgin for his valuable assistance throughout the entire process, from the very beginning to the final stages of this research journey.

Finally, I gratefully acknowledge Sabancı University for providing the academic environment, research facilities, and resources that made this thesis possible.

TABLE OF CONTENTS

LIST OF TABLES

LIST OF FIGURES

LIST OF SYMBOLS

$\mathbf{A}^e$ Element coefficient matrix.

$\boldsymbol{AF_i}$ Average frequency of the i-th acoustic emission hit.

$\boldsymbol{A_i}$ Amplitude of the i-th acoustic emission hit.

$\boldsymbol{\alpha}$ Dimensionless coefficient of the derivative-control term.

$\mathbf{B}_\alpha$ Derivative matrix for the derivative-consistency term.

$\mathbf{B}_\beta$ Derivative matrix for the curvature-control term.

$\boldsymbol{\beta}$ Dimensionless curvature-control parameter.

$\mathbf{D}_\beta$ Coefficient matrix relating the reconstructed field to auxiliary derivative variables.

$\boldsymbol{D_1}$ Gradient-based localization index.

$\boldsymbol{D_2}$ Threshold-gradient localization index.

$\boldsymbol{D_3}$ Nonlinearly normalized damage-sensitive localization index.

$\boldsymbol{\Delta t}$ Time interval.

$\boldsymbol{\Delta\theta}$ Orientation difference.

$\boldsymbol{D_i}$ Duration of the i-th acoustic emission hit.

$\boldsymbol{d_{\min}}$ Minimum distance from the initial crack tip.

$\boldsymbol{E_{11}}$ Longitudinal elastic modulus.

$\boldsymbol{E_{22}}$ Transverse elastic modulus.

$\boldsymbol{E_c}$ Cumulative acoustic emission energy.

$\boldsymbol{E_f}$ Flexural modulus.

$\boldsymbol{E_i}$ Energy of the i-th acoustic emission hit.

$\boldsymbol{\ell}$ Characteristic length.

$\boldsymbol{F}$ Penalized discrete least-squares functional.

$\boldsymbol{F_b}$ Flexural strength at failure.

$\boldsymbol{G_{12}}$ In-plane shear modulus.

$\mathbf{H}^e$ Right-hand side vector of element unknowns.

$\boldsymbol{H_j}$ Acoustic emission hit rate in the j-th time bin.

$\boldsymbol{K}$ Number of clusters.

$\boldsymbol{\kappa_1}$ Auxiliary field representing the first-order derivative with respect to the 1-direction.

$\boldsymbol{\kappa_2}$ Auxiliary field representing the first-order derivative with respect to the 2-direction.

$\boldsymbol{MAD_k}$ Median absolute deviation of the k-th feature.

$\mathbf{N}$ Shape-function matrix.

$\boldsymbol{N_i}$ Counts of the i-th acoustic emission hit.

$\boldsymbol{n_j}$ Number of acoustic emission hits in the j-th time bin.

$\boldsymbol{\nu_{12}}$ Major Poisson's ratio.

$\boldsymbol{PF_i}$ Peak frequency of the i-th acoustic emission hit.

$\mathbf{q}^e$ Element nodal unknown vector.

$\boldsymbol{RA_{50,j}}$ Median RA value in the j-th time bin.

$\boldsymbol{RA_{90,j}}$ 90th percentile RA value in the j-th time bin.

$\boldsymbol{RA_i}$ RA value of the i-th acoustic emission hit.

$\boldsymbol{R_{E,j}}$ Acoustic emission energy rate in the j-th time bin.

$\boldsymbol{S}$ Area of the smoothing element.

$\boldsymbol{\tau}$ Threshold ratio.

$\boldsymbol{\theta_{\mathrm{crack}}}$ Experimentally observed crack-propagation direction.

$\boldsymbol{\theta_{D_3}}$ Dominant orientation of the high-index band.

$\boldsymbol{t_i}$ Acquisition time of the i-th acoustic emission hit.

$\boldsymbol{u}$ In-plane displacement component in 1-direction.

$\boldsymbol{v}$ In-plane displacement component in 2-direction.

$\boldsymbol{\varepsilon}$ Normal strain.

$\boldsymbol{\varepsilon^h}$ Discrete experimental field value.

$\boldsymbol{\varepsilon_{vm}}$ von Mises equivalent strain.

$\boldsymbol{x_i}$ Multi-parameter feature vector of the i-th acoustic emission hit.

$\boldsymbol{x_1}$ Cartesian coordinate in 1-direction.

$\boldsymbol{x_2}$ Cartesian coordinate in 2-direction.

$\boldsymbol{x_{ik}}$ Original value of the k-th feature for the i-th acoustic emission hit.

$\boldsymbol{x_k}$ Median of the k-th feature.

$\boldsymbol{X_t}$ Longitudinal tensile strength.

$\boldsymbol{Y_t}$ Transverse tensile strength.

$\boldsymbol{\zeta}$ Area coordinate of the triangular smoothing element.

$\boldsymbol{z_{ik}}$ Standardized value of the k-th feature for the i-th acoustic emission hit.

LIST OF ABBREVIATIONS

AE Acoustic Emission.

AF Average Frequency.

CFRP Carbon Fiber Reinforced Polymer.

DIC Digital Image Correlation.

MAD Median Absolute Deviation.

PCA Principal Component Analysis.

PF Peak Frequency.

RA Rise Time to Amplitude Ratio.

SEA Smoothing Element Analysis.

SG Strain Gauge.

1. INTRODUCTION

Laminated composite structures are widely used in aerospace, marine, automotive, wind-energy, and civil engineering applications because of their high specific stiffness, high specific strength, and corrosion resistance (Soutis, 2005), and because they combine the possibility of tailoring the mechanical response through fiber orientation and stacking sequence design (Daniel & Ishai, 2006; Hull & Clyne, 1996; Jones, 1999). This design flexibility, however, is accompanied by complex damage behavior governed by anisotropy, ply-level architecture, interlaminar load transfer, and local stress redistribution (Daniel & Ishai, 2006; Herakovich, 1998). Unlike homogeneous materials, laminated composites generally do not fail through a single dominant fracture event. Their damage evolution may involve matrix cracking, fiber/matrix debonding, fiber fracture, delamination, and progressive stiffness degradation (Talreja, 1994; Talreja & Singh, 2012). These mechanisms may initiate locally, interact with the laminate architecture, and evolve progressively under mechanical loading before final macroscopic failure becomes visible. This distinction is further supported by failure criteria and physically based failure models, which show that matrix- and fiber-dominated failure modes should be interpreted separately in fiber-reinforced laminates (Hashin, 1980; Puck & Schürmann, 1998). Among these mechanisms, delamination is particularly critical because it weakens the connection between adjacent plies and reduces the laminate's ability to transfer load through the thickness (Wisnom, 2012). Therefore, crack propagation in composite laminates should be understood as a progressive and interacting damage process rather than only as the visible extension of a pre-existing crack, and reliable crack propagation monitoring and crack-sensitive localization are essential for the structural health monitoring of composite components (Farrar & Worden, 2007; Güemes et al., 2020).

This progressive character becomes more difficult to interpret when the laminate contains an initial crack, notch, hole, or similar geometric discontinuity. Stress concentration studies on laminated composites have shown that such discontinuities disturb the local stress field and create preferred regions for damage initiation

(Nuismer & Whitney, 1975; Whitney & Nuismer, 1974). The subsequent damage path depends not only on the presence of the discontinuity, but also on the laminate configuration, fiber direction, and loading direction (Bilgin & Kefal, 2025; Chang & Chang, 1987; Tan, 1991). More general progressive damage formulations have shown that matrix cracking, fiber failure, and stiffness degradation may develop before final rupture and may interact with the local stress concentration field (Camanho & Matthews, 1999; Lapczyk & Hurtado, 2007). In this context, Camanho and Matthews (1999) demonstrated the importance of progressive damage modelling for local damage accumulation in mechanically fastened composite laminates, while Lapczyk and Hurtado (2007) emphasized the representation of stiffness degradation in progressive failure modelling. Ubaid et al. (2014) combined three-dimensional finite element analysis with digital image correlation for CFRP laminates containing multiple interacting holes and showed that local deformation fields are essential for understanding progressive failure. These studies indicate that crack-related damage cannot be reliably interpreted from global failure data alone, especially when local strain redistribution and damage accumulation occur before macroscopic fracture becomes visible.

Damage mechanics studies provide a complementary theoretical basis for this interpretation. Barbero and De Vivo (2001) formulated an elastic damage model for fiber-reinforced polymer matrix laminae, showing how damage can be represented through degraded constitutive behavior. Okabe et al. (2018) developed a continuum damage mechanics model for composite laminates containing transverse cracks and related effective stiffness reduction to crack density. Li et al. (2019) discussed the identification of damage-related material constants in continuum damage mechanics formulations for unidirectional composites with matrix cracks. Onodera and Okabe (2020) proposed an analytical model for predicting effective stiffness and mechanical behavior of polymer matrix composite laminates using continuum damage mechanics. Extending this mechanics-based discussion beyond elastic stiffness alone, Ahmadi et al. (2022) showed that ply cracking and delamination can also affect the effective thermo-elastic constants of damaged composite laminates. These works clarify the mechanics of damage progression, but they also highlight the need for experimental evidence capable of showing how crack-related deformation and damage activity develop during loading.

The final failure state alone is not sufficient for this purpose. Fractographic observations can identify important features of the fracture surface after testing (Greenhalgh, 2009; Purslow, 1986). However, the fracture surface mainly represents the terminal state of a damage process that has already passed through several inter-

mediate stages (Greenhalgh, 2009). Standard tensile test outputs are also necessary because they provide global indicators such as stiffness, ultimate strength, failure strain, and nonlinear mechanical response (Adams et al., 2003; *Standard Test Method for Tensile Properties of Polymer Matrix Composite Materials*, n.d.). Nevertheless, global load–displacement or stress–strain curves cannot directly show where damage localizes over the specimen surface. They also cannot determine whether a change in the mechanical response is mainly associated with matrix cracking, delamination, fiber fracture, or local strain redistribution. For this reason, structural health monitoring and nondestructive evaluation studies increasingly emphasize in-situ measurements that can observe damage development during loading rather than only after final rupture (Farrar & Worden, 2007; Gholizadeh, 2016; B. Wang et al., 2020).

Following this need, crack propagation in composite laminates can be interpreted more reliably when its spatial, temporal, and local mechanical aspects are considered together. The spatial aspect is related to the heterogeneous deformation field that develops around a crack, notch, or stress concentration region. Full-field optical measurements have been used to capture high strain gradients and damage-related deformation in composite specimens with localized stress concentrations (Lagattu et al., 2004; Pierron et al., 2007a). The temporal aspect is related to the fact that damage activity does not remain constant throughout the test, but may initiate, accumulate, and accelerate at different loading stages. Acoustic emission testing provides a direct way to monitor this damage activity through transient elastic waves generated by active damage events (Grosse & Ohtsu, 2008; Miller et al., 2005). The local mechanical aspect is related to strain redistribution or stiffness degradation at selected points near critical regions. Strain gauge studies in composite materials have shown that local strain measurements remain useful when the interpretation of the mechanical response requires pointwise confirmation (Ajovalasit, 2010; Tuttle & Brinson, 1984). Therefore, digital image correlation, acoustic emission, and strain gauges provide different but complementary forms of experimental evidence.

Several sensing techniques have been used for monitoring composite structures, including strain gauges and fiber-optic sensors for local or distributed deformation measurements (Güemes et al., 2020; Rocha et al., 2021), acoustic-emission systems for detecting transient damage-related events during loading (Willberry et al., 2020), and piezoelectric transducers or guided-wave approaches for wave-based damage interrogation (Memmolo et al., 2018; Su et al., 2006). These approaches are valuable for structural health monitoring; however, their measurements are usually available only at discrete sensor locations or along predefined sensing paths. This limitation

becomes important when the target phenomenon evolves spatially, as in crack initiation, crack-tip deformation, and crack propagation in heterogeneous composite laminates. The spatial limitation of discrete sensing has also motivated the development of inverse reconstruction strategies, in which sparse sensor measurements are used to estimate continuous deformation fields. In this context, the Particle Inverse Method has been proposed for full-field displacement and crack propagation monitoring from discrete sensor data and has subsequently been experimentally validated for composite laminates (Bilgin & Kefal, 2025; Kefal et al., 2024). These studies show that crack-related deformation can be reconstructed even when only sparse measurements are available. However, when the specimen surface is optically accessible, full-field measurement techniques provide a more direct experimental route for observing the spatial evolution of deformation. This makes optical full-field methods particularly suitable for crack propagation studies, where the response is not confined to a single sensor location but develops over a region surrounding the crack tips.

Among optical full-field techniques, digital image correlation (DIC) has become one of the most widely used experimental methods for measuring deformation in composite materials and structures. Early image-correlation studies established the basis for extracting displacement information from digital image sequences (Peters & Ranson, 1982; Sutton et al., 1983). Chu et al. (1985) demonstrated the applicability of DIC to experimental mechanics, and Bruck et al. (1989) improved the correlation procedure using a Newton–Raphson-based correction strategy. Later studies consolidated DIC as a full-field deformation measurement method and discussed its theoretical background, subset selection, calibration requirements, and strain calculation procedures (Hild & Roux, 2006; Pan et al., 2009; Sutton et al., 2009). In composite materials and structures, DIC is particularly useful because it provides spatially dense measurements over the region of interest and allows local deformation mechanisms to be observed during crack growth and failure evolution (Grediac, 2004; Janeliukstis & Chen, 2021). Since the reliability of DIC results depends on calibration, facet/subset selection, spatial resolution, correlation quality, and data-processing choices, good-practice recommendations emphasize the importance of reporting DIC acquisition and processing parameters (International Digital Image Correlation Society et al., 2018). For damage studies, the value of DIC is not limited to measuring displacement. McNeill et al. (1987) demonstrated the use of DIC for stress intensity factor estimation in cracked specimens. More generally, Wattrisse et al. (2001) showed, through tensile tests on metallic specimens, that DIC can capture strain localization during deformation.

DIC and related full-field optical techniques have been widely used to characterize deformation and failure processes in fiber-reinforced composites (Holmes et al., 2023). In open-hole tensile laminates, DIC has been applied to examine full-field strain localization, progressive failure, and the interaction between intra-laminar and inter-laminar mechanisms (Oz et al., 2020; Pierron et al., 2007a, 2007b). Other studies have combined DIC with acoustic emission or progressive damage modelling to interpret damage evolution and identify dominant failure modes in composite laminates (Han et al., 2020; Özaslan et al., 2021; M. Wang et al., 2023). In composite laminates, Tabrizi et al. (2022) used experimental in-situ optical strain measurements for damage growth and failure detection in hybrid fiber composites. In a related composite fracture study, Tabrizi, Kefal, Zanjani, et al. (2019) combined experimental observations, acoustic emission analysis, and refined zigzag theory to investigate fracture behavior in glass/carbon hybrid composites. DIC-based measurements have also been used to characterize delamination onset, fatigue delamination growth, and delamination-driven failure under compressive loading (Calvo et al., 2022; Zhu et al., 2020). In addition, multi-instrumentation studies combining DIC, acoustic emission, and microscopy have shown that full-field optical measurements can support the interpretation of complex composite failure mechanisms under different loading conditions (Ali et al., 2019; Hamdi et al., 2021). Beyond these studies, DIC has also been used for bonded repairs, multiscale matrix-crack detection, combined full-field damage investigation, and strain measurement in heterogeneous composite systems (Caminero et al., 2013; del Rey Castillo et al., 2019; Goidescu et al., 2013; Mehdikhani et al., 2018). In fracture-related applications, DIC displacement fields have been used to estimate crack-tip quantities such as stress intensity factors and J-integral values, demonstrating the potential of full-field measurements for crack-sensitive analysis (Becker et al., 2012; McNeill et al., 1987). These studies show that optical full-field strain data is well suited for observing the surface manifestation of crack-related deformation. However, DIC mainly represents the visible surface response and cannot independently identify the internal damage mechanism responsible for the observed localization.

These studies collectively show that DIC provides valuable information about spatially evolving deformation and fracture processes. However, using DIC data for crack-sensitive localization still involves important numerical challenges. The main challenge is that displacement is the primary measured quantity in DIC, whereas strain is obtained by differentiating the measured displacement field. This displacement-to-strain transition is sensitive to measurement noise, local correlation fluctuations, and the selected strain-calculation procedure; therefore, dedicated differentiation or filtering strategies are often required to obtain stable DIC-derived

strain fields (Lagattu et al., 2004; Pan et al., 2007; Qiu et al., 2022). This issue becomes more critical when DIC data are used not only to visualize strain contours, but also to identify localized crack-sensitive regions. High strain gradients are commonly observed around stress concentrations and crack-tip regions, and strain-gradient information has been shown to provide useful indications of crack initiation and subsequent crack propagation in heterogeneous composite systems (Lagattu et al., 2004; Qiu et al., 2022). In such analyses, reconstructed strain components may be reduced to a scalar equivalent strain field, and spatial gradients of this scalar field may then be evaluated to detect localization. Therefore, the localization workflow contains two successive sensitivity points: first, the displacement-to-strain transition, and second, the equivalent-strain-to-gradient transition.

Several post-processing strategies have been proposed to improve DIC-derived strain fields, including polynomial-based smoothing, radial-basis-function interpolation, weak regularization, and anisotropic diffusion smoothing (Dai et al., 2015; Groth et al., 2022; Rouwane et al., 2022; Z. Wang et al., 2024). These methods improve the stability of reconstructed strain fields, but they generally focus on regularizing the displacement field, the strain field, or the correlation procedure itself. In crack propagation monitoring, however, the final localization map depends not only on the strain magnitude around the crack tips, but also on the stability of the spatial gradients used to identify crack-sensitive regions. Therefore, the stabilization of strain reconstruction and the stabilization of equivalent-strain gradient evaluation should be treated as two separate steps of the same crack-localization workflow. Smoothing element analysis (SEA) provides a suitable basis for such a staged processing strategy. SEA is rooted in penalized discrete least-squares and variational recovery formulations originally developed for stress recovery and error estimation in finite element analysis (Riggs et al., 1997; Tessler et al., 1994, 1998, 1999). Its key feature is that it reconstructs continuous field quantities from discrete data while introducing derivative consistency through auxiliary derivative fields. Previous work has shown the effectiveness of SEA-based smoothing in inverse mechanics and shape-sensing applications involving composite structures (Kefal et al., 2021).

Gradient-based quantities are also relevant for crack-sensitive analysis because strain localization, crack initiation, and crack propagation are generally associated with strong spatial variations in the strain field. In computational mechanics, gradient-enhanced damage models have been used to regularize strain localization and describe size-sensitive damage evolution (Askes & Sluys, 2002; de Borst et al., 1995; Peerlings et al., 1996). However, the objective of the present work is not to introduce a constitutive damage model. Instead, gradient information is used as an experimen-

tally derived localization feature obtained directly from full-field DIC measurements. In this way, the proposed approach remains data-driven and does not require finite element damage modelling, constitutive damage laws, or material degradation parameters.

Acoustic emission (AE) provides a complementary damage-sensitive measurement by recording elastic waves generated by sudden energy release during active damage events. de Groot et al. (1995) investigated real-time frequency determination for different fracture mechanisms in carbon/epoxy composites, and Bohse (2000) examined AE characteristics of micro-failure processes in polymer blends and composites. Huguet et al. (2002) used AE to identify damage modes in glass-fiber-reinforced polyester, while Ramirez-Jimenez et al. (2004) related the primary frequency content of AE events to failure modes in glass/polypropylene composites. These early studies show that AE can provide mechanism-sensitive information, but they also indicate that the interpretation depends on signal features, material system, and experimental conditions. AE parameters are commonly used to evaluate the onset and progression of damage activity during mechanical loading. Godin et al. (2004) used supervised and unsupervised classifiers to process AE signals collected during tensile tests on unidirectional glass/polyester composites. Godin et al. (2005) later integrated a self-organising map and k-means algorithm for AE data segmentation in cross-ply composites. Gutkin et al. (2011) investigated failure in CFRP using pattern recognition and peak frequency analysis. McCrory et al. (2015) compared different AE-based techniques for damage classification in carbon fiber composites. Bussiba et al. (2008) used AE to follow damage evolution and fracture event sequences in different composite systems. Saeedifar and Zarouchas (2020) reviewed AE-based damage characterization in laminated composites and discussed the use of parameters such as amplitude, energy, duration, frequency-related quantities, hit activity, and cumulative trends. These studies indicate that AE is particularly useful for identifying when damage activity initiates, accumulates, or accelerates. Despite this advantage, AE-based mechanism identification should not be treated as a standalone proof of a specific damage mechanism. Sause (2016) emphasized that AE interpretation in fiber-reinforced composites is affected by source characteristics, wave propagation, attenuation, and sensor response. Öz et al. (2017) showed that high-frequency AE events do not always directly represent fiber failure in CFRP laminates. Romhány et al. (2017) reviewed the use of AE event location for evaluating damage development and crack growth in polymer composites and highlighted the complexity of AE-based crack interpretation. Assarar et al. (2015) used AE to monitor damage mechanisms in sandwich composite materials, and Alimirzaei et al. (2022) used AE to characterize damage mechanisms in filament-wound com-

posite tubes with different winding angles. These studies confirm the value of AE as a damage-activity indicator, but they also support the need to correlate AE results with independent spatial or mechanical observations when crack propagation is evaluated.

Strain gauges provide the third experimental perspective by recording local strain directly at the bonded gauge location. Ajovalasit and Pitarresi (2011) discussed the effect of strain gauge misalignment in composite strain measurement, while Hoffmann (1989) provided detailed guidance on strain gauge installation and measurement interpretation. Dally and Riley (2005) also described experimental stress analysis procedures relevant to local strain measurements. In composite laminates, these issues become important when strong strain gradients develop near cracks, notches, holes, or ply interfaces, because the recorded response represents an averaged strain over the active gauge length rather than a complete local deformation field. Brunbauer and Pinter (2014) discussed strain measurement and stiffness calculation in carbon-fiber-reinforced composites under quasi-static and fatigue loading. Arena et al. (2020) reviewed strain detection strategies in composite structures and highlighted the continuing importance of reliable local strain measurement. In a multi-instrument framework, strain gauges should therefore not be considered as an alternative to DIC or AE. Instead, they provide local mechanical confirmation when surface strain localization and acoustic activity indicate a comparable damage stage.

Several studies have demonstrated the value of combining optical and acoustic techniques for composite damage assessment. Flament et al. (2016) combined DIC and AE to relate local strain evolution to acoustic damage activity in composite specimens. Öz et al. (2018) used a multi-instrument in-situ approach to investigate damage development in quasi-isotropic CFRP laminates under tension. Tabrizi, Khan, et al. (2019) combined DIC and AE to evaluate the effect of tab material on the tensile response and failure of CFRP laminates. Han et al. (2020) used AE and DIC to support progressive damage analysis of open-hole tensile laminated composites. Özaslan et al. (2021) applied AE and DIC for damage mode identification in open-hole composite laminates. Hamdi et al. (2021) combined DIC, AE, and in-situ microscopy to investigate damage development in composite specimens under compression. These works show that full-field strain data and acoustic activity can support each other, especially when the aim is to relate damage localization to damage activity during loading. More recent studies have extended the combined AE–DIC concept to additional damage scenarios. Habibi and Laperrière (2023) used DIC and AE to characterize the flexural behavior of flax biocomposites. Andraju and Raju (2023) used AE and DIC for damage characterization, clustering,

identification, and classification in CFRP laminates. M. Wang et al. (2023) applied AE and DIC to monitor fatigue damage in composite laminates. Yuan et al. (2025) integrated AE and DIC to study damage in composite panels with different layup sequences. These studies confirm that AE and DIC can provide mutually supportive information. However, their main emphasis is often placed on damage mode classification, fatigue monitoring, open-hole behavior, compression damage, flexural response, or layup-dependent damage comparison. A dedicated interpretation framework for pre-cracked laminates still requires a clearer link between surface strain localization, temporal AE activity, and local strain response.

Despite significant progress in full-field optical monitoring, AE-based damage characterization, and combined AE-DIC assessment, two interconnected gaps remain in the monitoring of crack propagation in pre-cracked composite laminates. The first gap concerns the numerical stability of the DIC-based localization chain. Existing DIC post-processing strategies commonly focus on improving the displacement field, the strain field, or the correlation procedure, whereas the stabilization of strain reconstruction and the stabilization of equivalent-strain gradient evaluation are usually not handled as two distinct steps within the same crack-localization workflow. This distinction is particularly important for cracked composite laminates, because the final localization response depends not only on the strain magnitude around the crack tips, but also on the stability of the spatial gradients used to identify localized crack-sensitive regions. Moreover, crack-path agreement is often discussed mainly through visual comparison, while quantitative pre-failure indicators are still needed to support the interpretation of localization maps. The second gap concerns the experimental interpretation of crack propagation. A localized DIC strain field can reveal the surface manifestation of crack-related deformation, but it does not directly indicate whether the observed localization corresponds to active crack growth, delayed fracture, or local strain redistribution. Similarly, AE activity can identify the timing and intensity of damage events, but it cannot describe the spatial path of crack propagation. Strain gauges can provide local mechanical evidence near critical regions, but their response is limited to selected measurement points. Therefore, the remaining challenge is not simply to collect multiple measurements during the same experiment, but to establish a consistent interpretation framework in which spatial localization, temporal acoustic activity, and local strain redistribution are evaluated together for the same crack-propagation process.

1.1 Contributions Beyond the State of the Art

This thesis addresses the identified research gaps through two complementary studies conducted on the same set of pre-cracked carbon/epoxy composite laminate specimens with different stacking sequences and initial crack orientations. The main contributions beyond the state of the art are summarized as follows:

1. A dual-stage SEA-assisted DIC framework is introduced for full-field crack-sensitive localization in pre-cracked composite laminates. Unlike conventional DIC post-processing strategies that generally focus on smoothing a single field quantity, the proposed framework treats the two critical sensitivity stages of the localization chain separately. The measured in-plane displacement field is first regularized before strain reconstruction, and the von Mises equivalent strain field is then smoothed before spatial-gradient evaluation. This staged formulation improves the stability of both DIC-based strain reconstruction and gradient-based localization.

2. A gradient-enhanced, thresholded, and nonlinearly normalized damage-sensitive localization index is formulated directly from full-field experimental DIC measurements. The proposed index is model-free because it is derived from measured displacement data and does not require a constitutive damage law, finite element damage simulation, or material degradation parameters. Therefore, the crack-sensitive localization response is obtained directly from experimental full-field deformation data.

3. A quantitative pre-failure localization assessment is introduced to evaluate the agreement between high-index localization regions and experimentally observed crack-propagation behavior. In addition to visual comparison, crack-tip proximity and localization-band orientation metrics are used to assess whether the detected localization regions are physically consistent with the observed crack path. This provides a more objective basis for evaluating pre-failure crack-sensitive localization.

4. An integrated multi-instrument framework is developed for damage characterization and crack propagation monitoring in pre-cracked composite laminates. This framework correlates full-field DIC strain localization, AE activity trends, cluster-wise cumulative energy evolution, and strain gauge measurements within a stage-wise interpretation strategy. In this way, crack propagation is interpreted through the combined evaluation of spatial deformation

evidence, temporal acoustic damage activity, and local mechanical strain response.

5. The proposed methodologies are experimentally assessed on seven cracked composite laminate configurations with different stacking sequences and initial crack orientations. This unified experimental campaign enables the interpretation of progressive crack growth, delayed high-energy propagation, and abrupt fracture-dominated transitions under the same tensile loading condition. As a result, the thesis establishes a model-free, experimentally driven, and multi-instrument basis for monitoring spatial and temporal crack evolution in pre-cracked composite laminates.

1.2 Structure of the Thesis

This thesis is organized into five chapters.

Chapter 1 presents the general introduction, background, motivation, research gaps, and main contributions of the thesis. It discusses the need for reliable crack propagation monitoring in composite laminates and explains why spatial, temporal, and local mechanical evidence should be evaluated together.

Chapter 2 describes the material system, specimen configurations, manufacturing procedure, and experimental preparation. The carbon/epoxy laminate system, stacking sequences, initial crack orientations, tab bonding procedure, speckle pattern preparation, and instrumentation strategy are introduced. The tensile testing setup, DIC system, acoustic emission system, strain gauge implementation, and multi-instrument synchronization approach are also presented.

Chapter 3 presents the full-field crack propagation monitoring framework based on digital image correlation and smoothing element analysis. The mathematical formulation of the dual-stage SEA-assisted DIC methodology is explained, including displacement-field smoothing, strain reconstruction, equivalent strain smoothing, gradient evaluation, and the formulation of the damage-sensitive localization index. The chapter then validates the proposed approach on the seven cracked laminate configurations and evaluates the pre-failure localization performance through both visual crack-path comparison and quantitative localization metrics.

Chapter 4 presents the integrated multi-instrument analysis framework for damage characterization and crack propagation monitoring. In this chapter, DIC-based strain localization, acoustic emission activity, AE clustering, cluster-wise cumulative energy evolution, global stress–strain response, and strain gauge measurements are evaluated together. The chapter provides a stage-wise interpretation of crack propagation and compares the effects of stacking sequence and initial crack orientation on progressive, delayed, and fracture-dominated damage evolution.

Chapter 5 summarizes the main conclusions of the thesis. It highlights the principal findings obtained from the SEA-assisted DIC framework and the integrated DIC–AE–strain gauge analysis. The chapter also discusses the broader implications of the proposed methodology for structural health monitoring of composite laminates and outlines possible directions for future research.

1.3 Research Outputs

The work conducted during the author's graduate studies has resulted in the following journal manuscripts:

1. **I. Bahadır**, M. H. Bilgin, A. Al-Nadhari, M. Yildiz, and A. Kefal, "Full-field crack propagation monitoring in composite laminates using digital image correlation and smoothing element analysis," submitted to *Composite Structures*. This manuscript is based on Chapter 3 of this thesis.

2. **I. Bahadır**, M. H. Bilgin, A. Al-Nadhari, M. Yildiz, and A. Kefal, "Integrated multi-instrument analysis for damage characterization and crack propagation monitoring in pre-cracked composite laminates," submitted to *International Journal of Damage Mechanics*. This manuscript is based on Chapter 4 of this thesis.

3. E. Yıldırım, **I. Bahadır**, J. Bardiani, C. Sbarufatti, and A. Kefal, "Experimental shape sensing of a NACA-profile composite wing with FBG sensors on a single surface using inverse finite element method," submitted to *Structural Control and Health Monitoring*. This manuscript represents an additional related research output in the field of composite structural health monitoring.

2. MATERIALS AND SPECIMEN PREPARATION

2.1 Material System and Laminate Manufacturing

The experimental study is carried out on cracked carbon/epoxy composite laminate specimens. The laminates are manufactured from unidirectional carbon/epoxy prepreg supplied by Kordsa. The prepreg material is UD300 35% 34700 24K with AX-201XL resin. It has a fiber weight of 300 g/m^2 and a resin content of 35%. Before manufacturing, the prepreg rolls are stored at -18°C and kept at room temperature for 24 h before lay-up. The prepreg sheets are cut to the required dimensions and stacked according to the selected fiber orientations. Prior to lay-up, the mold surface is cleaned with ethanol and acetone, and a release agent is applied to obtain a smooth laminate surface and facilitate demolding after curing. After lay-up, the laminate stack is covered with peel ply and breather layers and sealed inside a vacuum bag. The stack is kept under vacuum before curing to improve laminate consolidation. The curing process is performed in an autoclave under controlled pressure and temperature conditions. A full vacuum is initially applied together with an autoclave pressure of 5.5 bar. When the autoclave pressure reaches 1 bar, the vacuum pressure is reduced to 0.2 bar. The temperature then increased to 120°C at a heating rate of 3°C/min, held at this temperature for 90 min, and finally decreased to room temperature at a cooling rate of 3°C/min. After curing, the composite plates are cut into cracked plate specimens and prepared for tensile testing.

2.2 Specimen Configuration

The experimental setup includes seven cracked laminate configurations designed to examine the combined effect of stacking sequence and initial crack orientation on damage localization and crack propagation. Four laminate families are considered: two mixed-orientation laminates, (0/90/0) and (90/0/90), and two single-orientation laminates, (0/0/0) and (90/90/90). The initial crack is introduced at the center of the plate with either a 45° or 90° in-plane orientation. The resulting test matrix is given in Table 2.1. The configurations are selected to compare crack propagation in laminates where the crack direction is aligned differently with respect to the dominant fiber direction. This enables the effect of both ply sequence and crack orientation to be evaluated under the same tensile loading condition. The geometry of the specimen is shown in Figure 2.1.

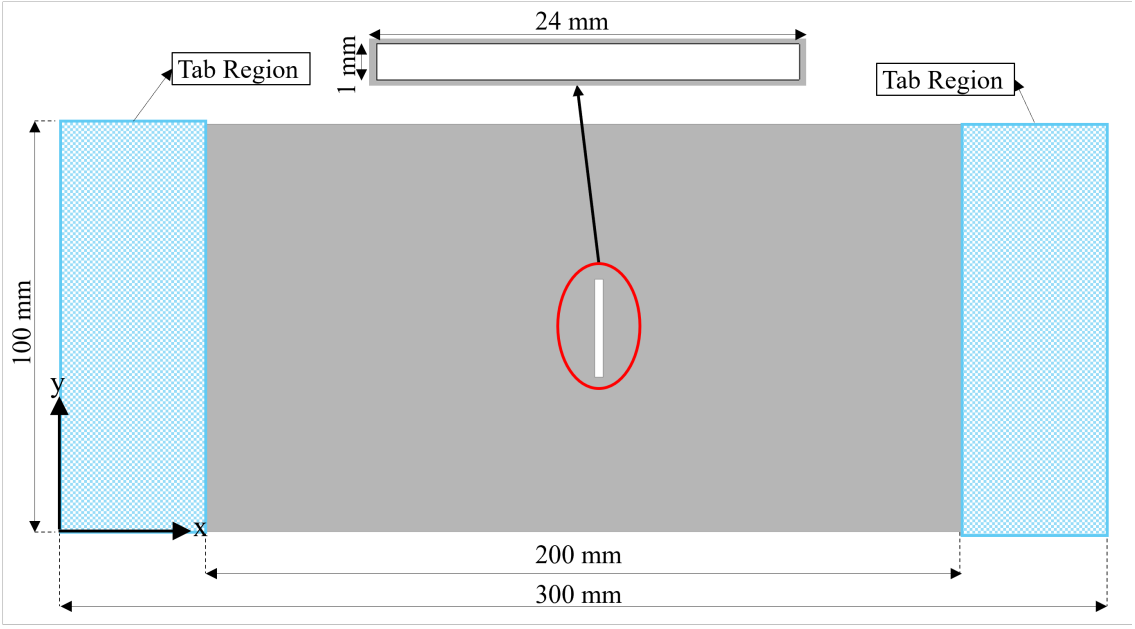

Figure 2.1 Representative geometry of the pre-cracked composite laminate specimen, including the tab regions, specimen dimensions, central initial crack.

All configurations are tested with digital image correlation and acoustic emission monitoring. Therefore, each specimen provides full-field surface deformation data and time-dependent acoustic damage activity. Strain gauges are applied to three selected configurations: (0/0/0) with a 90° crack, (0/0/0) with a 45° crack, and (90/90/90) with a 90° crack. These configurations provide an additional local strain response for the multi-instrument interpretation.

Table 2.1 Specimen Configurations and Measurement Systems

Specimen Number	Ply Sequence	Crack Orientation	DIC / AE	Strain Gauge
Specimen 1	(0/90/0)	90°	Yes / Yes	No
Specimen 2	(0/90/0)	45°	Yes / Yes	No
Specimen 3	(90/0/90)	45°	Yes / Yes	No
Specimen 4	(0/0/0)	90°	Yes / Yes	Yes
Specimen 5	(0/0/0)	45°	Yes / Yes	Yes
Specimen 6	(90/90/90)	45°	Yes / Yes	No
Specimen 7	(90/90/90)	90°	Yes / Yes	Yes

The elastic mechanical properties and strength values of the carbon/epoxy material system are summarized in Tables 2.2 and 2.3, respectively. The elastic properties include the longitudinal and transverse elastic moduli E_{11} and E_{22}, the in-plane shear modulus G_{12}, the major Poisson's ratio ν_{12}, and the flexural modulus E_{f}. The strength values include the longitudinal tensile strength X_{t}, the transverse tensile strength Y_{t}, and the flexural strength at failure F_{b}. These properties characterize the material system used in the experimental program and support the interpretation of the mechanical response of the cracked laminate specimens.

Table 2.2 Elastic Mechanical Properties of the Carbon/Epoxy Material

Material	E_{11} (GPa)	E_{22} (GPa)	G_{12} (GPa)	ν_{12}	E_{f} (GPa)
Carbon/epoxy	120	7.45	3	0.29	198

Table 2.3 Strength Properties of the Carbon/Epoxy Material

Material	X_{t} (MPa)	Y_{t} (MPa)	F_{b} (MPa)
Carbon/epoxy	2000	48	1000

2.3 Material Preparation

Before tensile testing, composite tabs are bonded to the gripping regions of each specimen to improve load transfer and reduce premature damage near the clamping zones. The tabs are prepared from the same composite material as the main specimens and have dimensions of 50 mm × 100 mm. A high-strength adhesive is used for tab bonding, and the specimens are kept under controlled conditions until the adhesive is fully cured. This preparation step provides a more stable gripping condition during tensile loading and helps ensure that the damage evolution is mainly observed around the central cracked region rather than near the grips.

After tab bonding, the specimen surfaces are prepared according to the requirements of the measurement systems. The front surface of each specimen is prepared for digital image correlation measurements. First, a uniform white base layer is applied using Belton Spectral RAL 9010 pure white acrylic spray paint. This base layer provides a bright and homogeneous background for optical tracking. After the white layer dries, a random black speckle pattern is applied using Belton Spectral RAL 9005 black acrylic spray paint. The black speckles are distributed over the measurement surface to create a high-contrast random pattern. The final configuration of front surface is shown in Figure 2.2. This pattern allows the DIC system to track the surface displacement field and calculate the corresponding strain distribution during tensile loading.

Figure 2.2 Representative front surface preparation of the pre-cracked composite laminate specimen with a random black-and-white speckle pattern used for digital image correlation measurements.

For the selected configurations, strain sensors are bonded to predefined locations on the specimen surface using a dedicated strain-gauge adhesive. The bonding regions are carefully prepared before installation to ensure good contact between the sensor

and the composite surface. Uniaxial strain gauges are used for the (0/0/0) laminate with a 90° initial crack and the (90/90/90) laminate with a 90° initial crack, while strain rosettes are used for the (0/0/0) laminate with a 45° initial crack to obtain additional in-plane strain information. The sensors are positioned to provide local strain measurements at mechanically relevant points around the cracked region, shown in Figure 2.3. These measurements are later compared with the full-field DIC response and the AE activity to support the stage-wise interpretation of crack propagation.

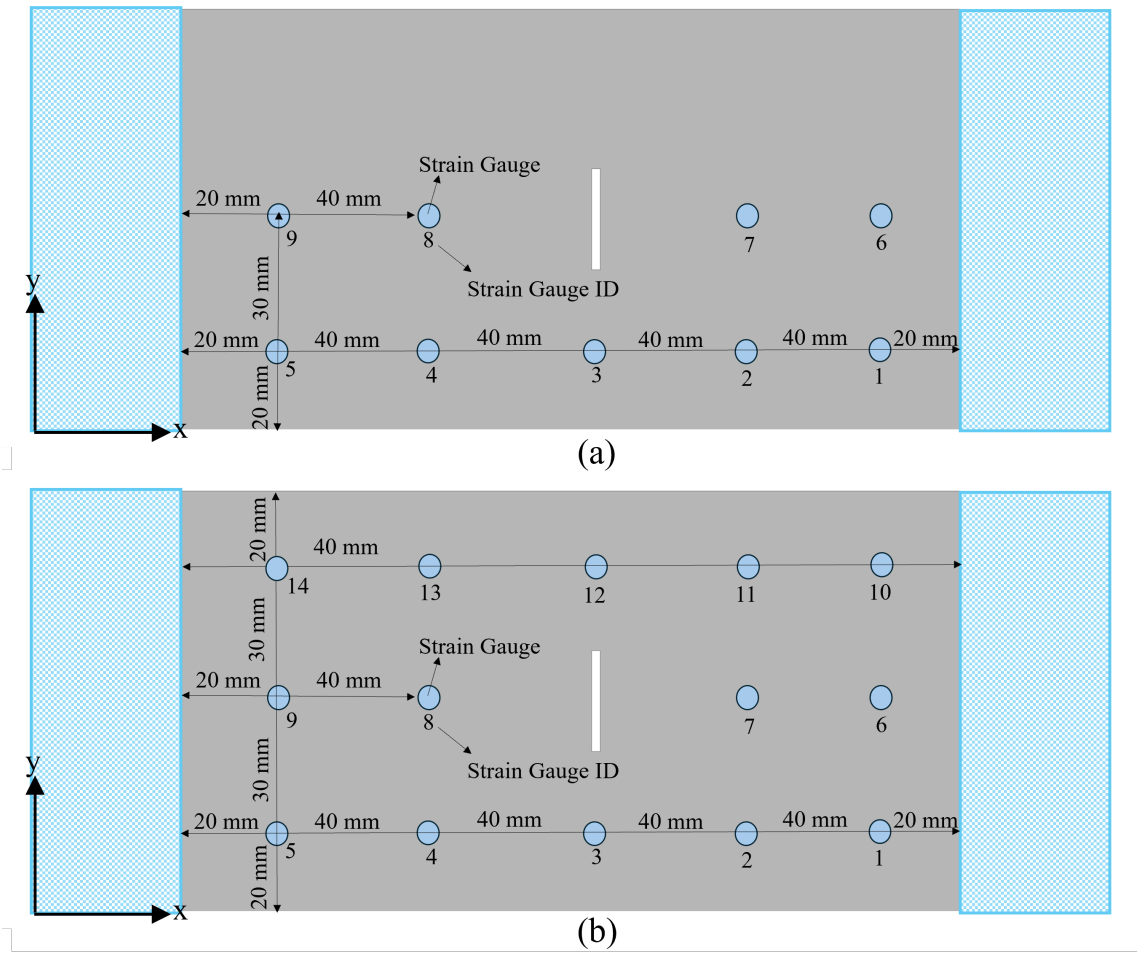

Figure 2.3 Strain gauge layouts used for local strain measurements on the pre-cracked composite laminate specimens: (a) layout used for the (0/0/0) laminate with a 90° initial crack and the (90/90/90) laminate with a 90° initial crack, and (b) layout used for the (0/0/0) laminate with a 45° initial crack.

Acoustic emission sensors are also attached to the specimens before testing. The AE sensors are mounted using silicone-based adhesive to provide stable contact with the specimen surface during tensile loading. This mounting approach allows the sensors to detect acoustic activity generated by damage events while maintaining sufficient coupling between the sensor and the composite plate. The AE system records the

time-dependent acoustic response of the specimens, while the DIC system captures full-field deformation and the strain gauges provide local mechanical measurements.

With this preparation procedure, each specimen is equipped for synchronized multi-instrument monitoring. The DIC speckle pattern provides the optical basis for full-field deformation tracking, the AE sensors provide temporal information related to damage activity, and the strain gauges provide local strain measurements for the selected configurations.

2.4 Experimental Setup and Instrumentation

2.4.1 Tensile Testing Setup

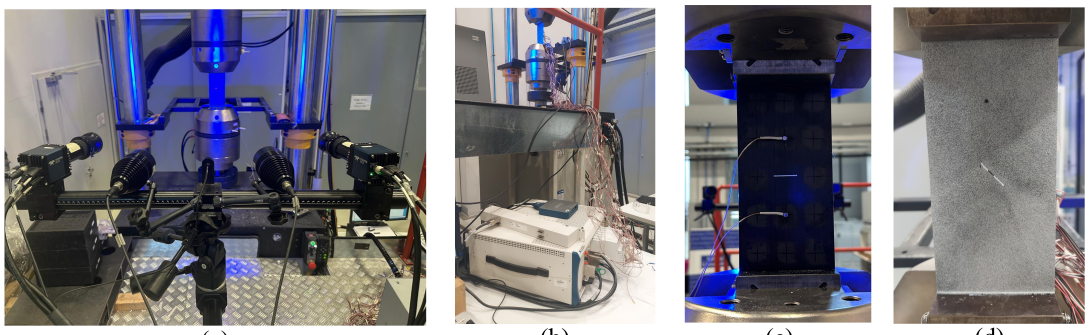

Figure 2.4 Experimental setup for synchronized multi-instrument tensile testing of pre-cracked composite laminate specimens: (a) tensile test configuration with the DIC camera system, (b) strain gauge data acquisition unit, (c) AE sensor implementation on the specimen surface, and (d) specimen mounting.

The tensile tests are performed using an Instron 8853 hydraulic universal testing machine. The specimens are loaded under displacement control with a crosshead speed of 1 mm/min. The tests are continued until final fracture so that the complete mechanical response and the crack propagation behavior can be recorded. During each test, the global mechanical response is obtained from the testing machine. The applied load, crosshead displacement, and test time are recorded throughout the experiment. These data provide the common mechanical reference for the DIC, AE, and strain gauge measurements. The laboratory conditions are kept stable during testing, with a room temperature of approximately 22.1°C and a relative humidity

of approximately 50.1%. The tensile tests are designed not only to obtain the global load-displacement response, but also to monitor the development of crack-related damage. Therefore, each specimen is tested under a multi-instrument measurement setup. DIC is used to capture the full-field surface deformation, AE is used to record damage-related acoustic activity, and strain gauges are used in selected configurations to measure local strain response. Test configuration is shown in Figure 2.4.

2.4.2 Digital Image Correlation Setup

The DIC system is used to measure the full-field surface displacement and strain evolution during tensile loading. The system is positioned to observe the front surface of the specimen, where the random speckle pattern is applied. The main region of interest includes the initial crack and the surrounding deformation zone. The DIC setup, calibration, and data preparation are performed using the ARAMIS/GOM software environment. Although the main region examined in the tests has dimensions close to 100 mm $\times$ 200 mm, the system is calibrated using a 300 mm $\times$ 230 mm measuring volume. This larger measurement volume is selected to keep the region of interest away from possible boundary effects and to obtain a more stable optical measurement field during loading. For the 300 mm $\times$ 230 mm measuring volume, the optical setup follows the calibration parameters recommended for the ARAMIS system. The measuring distance is set to 1455 mm, the slider distance is set to 616 mm, and the camera angle is adjusted to 25°. The minimum camera support length for this configuration is 800 mm. A CP20 250 mm $\times$ 200 mm calibration object is used for system calibration. During the optical setup, the aperture value is selected as 11. Calibration setup of DIC is shown in Figure 2.5.

During the tensile test, the DIC system records the deformation of the speckled surface. The main outputs of the DIC measurement are the in-plane displacement components in the x-direction and y-direction. These displacement fields are later used to evaluate the development of strain localization around the initial crack region. In this study, the DIC data provides the spatial evidence required for the multi-instrument interpretation of crack propagation. The DIC images are processed in ARAMIS/GOM to obtain the full-field deformation and strain response during tensile loading. The camera resolution is 4224 $\times$ 3264 pixels, and the calibrated measuring volume is approximately 300 $\times$ 230 mm. Based on this measuring volume, the image scale is approximately 0.071 mm/pixel. The DIC evaluation is performed using a facet size of 30 pixels and a point distance of 27 pixels. These

settings correspond to approximately 2.13 mm and 1.92 mm in the object plane, respectively. The "more points" computation option is used in ARAMIS/GOM to obtain a denser measurement field over the region of interest. No additional filtering or tolerance-based post-processing is applied in ARAMIS/GOM before the DIC results are evaluated. The resulting full-field strain data are used to examine the spatial development of strain localization around the initial crack region. In the subsequent analysis, the equivalent strain field is used as a scalar visualization measure for comparing crack-sensitive localization among different laminate configurations.

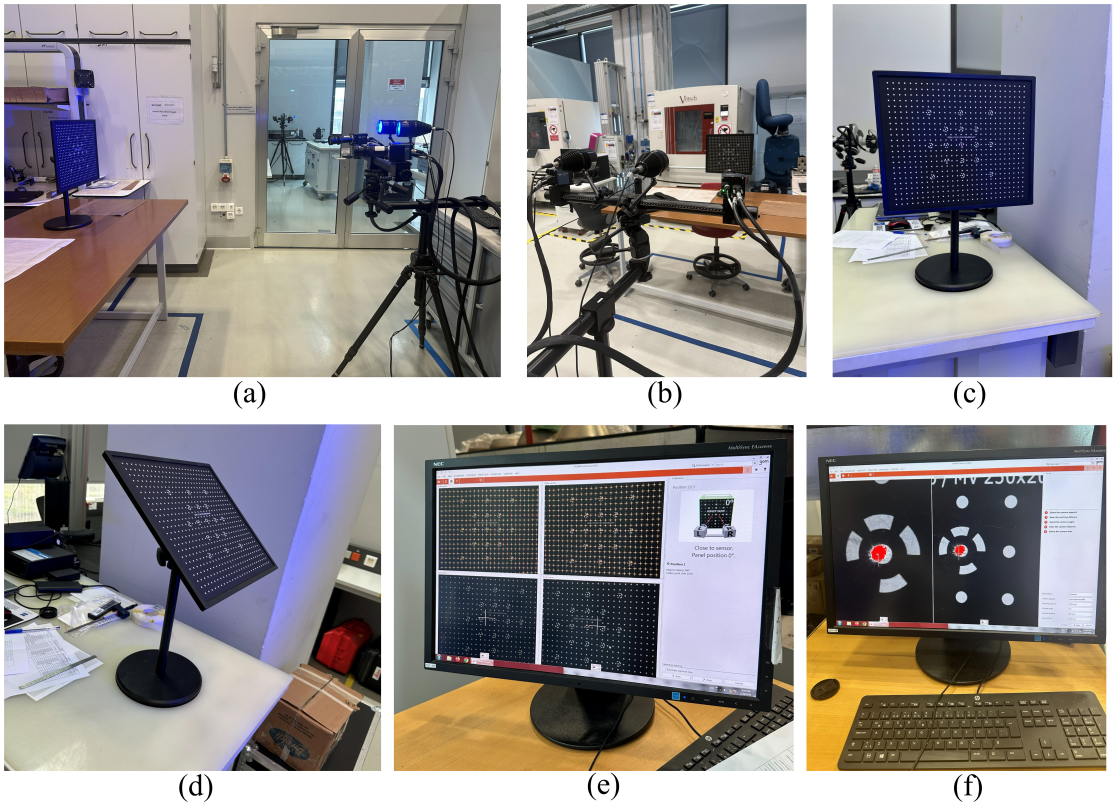

Figure 2.5 DIC calibration and optical setup procedure: (a) overall ARAMIS/GOM camera setup, (b) stereo-camera system positioned with the calibration panel, (c) CP20 250×200 calibration panel used for system calibration, (d) inclined positioning of the calibration panel during the calibration procedure, (e) ARAMIS/GOM calibration interface showing camera alignment and image acquisition, and (f) calibration image of the CP20 250×200 object used during the calibration process.

2.4.3 Acoustic Emission Setup

The AE system is used to monitor damage-related acoustic activity during tensile loading. Two AE sensors are attached to the back surface of each specimen before testing. The sensors are positioned so that they do not obstruct the DIC field of view, strain gauge connections, or gripping region. The sensor positions are selected as $x = 60$ mm, $y = 60$ mm and $x = 140$ mm, $y = 60$ mm on the back surface of the specimen. The AE sensors are mounted using silicone-based adhesive. This mounting approach provides stable contact between the sensor and the composite surface during the test while allowing the sensors to be removed after testing. The same sensor layout is used to maintain consistency between the tests. During loading, the AE system records acoustic signals generated by damage-related events inside the material. The AE data are used to evaluate the temporal development of damage activity. In the post-processing stage, parameters such as hit activity, signal amplitude, energy, and cumulative acoustic trends are examined and compared with the DIC and strain gauge responses. In this framework, AE provides temporal evidence for damage initiation, accumulation, and acceleration.

The acoustic emission response is recorded using two active AE channels. Before the tensile tests, both channels are operated with a fixed threshold of 42 dB and a pre-amplifier gain of 20 dB. The analog acquisition filter is set between 1 kHz and 3000 kHz. The waveform acquisition parameters are defined with a sampling rate of 2000 kHz, a pre-trigger time of 100 μs, and a waveform length of 2048 samples. The peak definition time, hit definition time, and hit lockout time are set to 50 μs, 150 μs, and 200 μs, respectively. The energy reference gain is set to 20 dB, the RMS/ASL time constant is set to 500 ms, and the time-driven rate is set to 1000 ms. After acquisition, AE feature extraction is performed using the recorded waveforms. The same threshold value of 42 dB and pre-amplifier gain of 20 dB are used during feature extraction, while the energy gain is set to 0 dB. The waveform data are processed using an eighth-order Bessel band-pass filter between 20 kHz and 800 kHz. Records without waveforms and waveforms below the threshold are removed before further analysis. Adaptive thresholding and multiple-hit extraction are not used.

2.4.4 Strain Gauge Setup

Strain gauges are used in selected laminate configurations to obtain local strain measurements during tensile loading. The gauges are bonded to predefined locations on the specimen surface using a dedicated strain gauge adhesive. The selected positions are chosen to provide local mechanical information that can be compared with the DIC strain field and AE activity. For the strain-gauged specimens, the strain gauge system is connected to a National Instruments data acquisition unit and recorded using NI SignalExpress 2015. Before testing, the strain gauge channels are checked and calibrated under zero-strain conditions. The gauge factor is set to 2.06, and the resistance value is defined as 350 Ω. The measurement configuration is selected as Quarter Bridge I, and the excitation voltage is set to 2.5 V using the internal excitation source. The sampling frequency is set to 1 kHz, and the data is recorded in continuous sampling mode. Offset nulling and shunt calibration are applied before the tests to reduce initial measurement errors and verify the measurement circuit. During the test, the strain gauge response is recorded continuously and synchronized with the mechanical test data. These measurements provide local mechanical evidence, especially when a deviation from the initial linear response or a change in local strain trend occurs near a damage stage.

2.4.5 Multi-Instrument Data Synchronization

The experimental setup is arranged to record the mechanical response, DIC images, AE signals, and strain gauge data during the same tensile loading process. The testing machine provides the load, crosshead displacement, and test time, which are used as the main reference quantities for comparing the different measurement outputs. The DIC system records the deformation of the speckled surface at selected time intervals, while the AE system continuously records damage-related acoustic events during loading. For the strain-gauged configurations, local strain data is also acquired continuously through the data acquisition system. During post-processing, the different data streams are aligned using the test time and the corresponding load level. This allows selected DIC frames to be compared with the AE activity and strain gauge response at the same loading stage. In particular, the development of strain localization in the DIC field is evaluated together with changes in AE and local strain response. This synchronized data set forms the basis for the stage-wise interpretation procedure presented in the following sections.

3. FULL-FIELD CRACK PROPAGATION MONITORING IN COMPOSITE LAMINATES USING DIGITAL IMAGE CORRELATION AND SMOOTHING ELEMENT ANALYSIS

3.1 Mathematical Formulation

3.1.1 General Framework

The present study proposes a dual-stage SEA-assisted DIC framework for constructing damage-sensitive localization index from full-field displacement measurements. The methodology is designed as a displacement-driven post-processing approach in which the measured in-plane DIC displacement field is used as the primary input.

The framework consists of two consecutive SEA stages. In the first stage, the measured in-plane displacement components are regularized using smoothing element analysis (SEA), and the in-plane strain components are reconstructed from the smoothed displacement field (Kefal et al., 2021). This stage is introduced to stabilize the displacement-to-strain transition, where direct differentiation of raw DIC data may amplify local measurement fluctuations. In the second stage, the von Mises equivalent strain field obtained from the reconstructed strain components is smoothed before spatial differentiation. This stage is introduced to reduce the sensitivity of the gradient calculation to residual local fluctuations in the equivalent strain field. The resulting strain-gradient information is then used to construct the damage-sensitive localization index.

In addition to the localization maps, a quantitative pre-failure localization assessment is introduced to evaluate the agreement between the high-index regions and the experimentally observed crack-propagation behavior. This assessment considers the minimum distance between the crack tip and the nearest high-index element, together with the orientation difference between the high-index localization band and the observed crack-propagation direction. Thus, the proposed framework provides both visual localization maps and quantitative indicators for assessing crack-sensitive regions before final fracture.

3.1.2 DIC Displacement Field

For a given loading stage, discrete in-plane displacement measurements are provided by the DIC system over the observed surface of the specimen. Let the measured dataset be written as:

$$\{x_{1i}, x_{2i}, u_i, v_i\}, \qquad i = 1, 2, \ldots, n \tag{3.1}$$

where x_{1i} and x_{2i} denote the in-plane coordinates of the i-th measurement point in the reference configuration, while u_i and v_i are the displacement components measured along the x_1 and x_2 directions, respectively. The associated displacement field is expressed as:

$$\boldsymbol{u}(\boldsymbol{x}) = \begin{bmatrix} u(x) \\ v(x) \end{bmatrix}, \qquad \boldsymbol{x} = \begin{bmatrix} x_1 \\ x_2 \end{bmatrix} \tag{3.2}$$

Since the valid DIC points may locally disappear in regions of severe deformation, crack opening, or decorrelation, the measured displacement field is not directly differentiated. Direct differentiation of the raw DIC data may amplify local measurement fluctuations and produce unstable strain contours. Therefore, the experimental displacement components are first regularized through SEA before strain reconstruction.

3.1.3 Smoothing of the Displacement Field

The measured displacement components are smoothed independently. For this purpose, let ε_i^h denote a generic discrete experimental field associated with the i-th DIC point, where ε represents either u or v. Over a single smoothing element S, the penalized discrete least-squares functional is written as:

$$F = \frac{1}{n}\sum_{i=1}^{n}\left[\varepsilon(\boldsymbol{x}_i) - \varepsilon_i^h\right]^2 + \alpha\int_S\left[(\varepsilon_{,1} - \kappa_1)^2 + (\varepsilon_{,2} - \kappa_2)^2\right]dS \\ + \beta S\int_S\left[\dot{\kappa}_{1,1}^2 + \dot{\kappa}_{2,2}^2 + \frac{1}{2}(\kappa_{1,2} - \kappa_{2,1})^2\right]dS \tag{3.3}$$

In Eq. (3.3), $\varepsilon(\boldsymbol{x}_i)$ is the analytical counterpart of the discrete quantity ε_i^h, whereas κ_1 and κ_2 are the auxiliary fields representing the first-order derivatives of ε with respect to the x_1 and x_2 directions. The first term enforces the fit between the smoothed field and the measured data. The second term constrains the derivatives of the reconstructed field through the auxiliary derivative variables κ_1 and κ_2. The third term is a curvature-control term introduced to suppress spatial oscillations and improve stability of the reconstructed field.

The weighting parameters in Eq. (3.3) are adopted following the SEA-based smoothing strategy reported by Kefal et al. (Kefal et al., 2021). Accordingly, the dimensionless coefficient of the derivative-control term is set to $\alpha = 1$, while the dimensionless curvature-control parameter is set to $\beta = 10^{-3}$. These parameters are not treated as specimen-dependent calibration variables and are not adjusted according to the observed crack path or damage pattern. Instead, the same α and β values are kept constant for all specimens and loading stages to maintain a consistent SEA-based post-processing procedure. In this formulation, α controls the consistency between the reconstructed field and its auxiliary derivative fields, whereas β controls the curvature-regularization contribution and helps suppress local oscillatory variations in the reconstructed field. The use of fixed parameters reduces the risk of specimen-specific smoothing bias in the subsequent strain reconstruction.

A three-node triangular smoothing element is adopted as shown in Figure 4.26. Within each smoothing element, the scalar field is approximated by using the nodal field values together with the auxiliary derivative degrees of freedom. Accordingly,

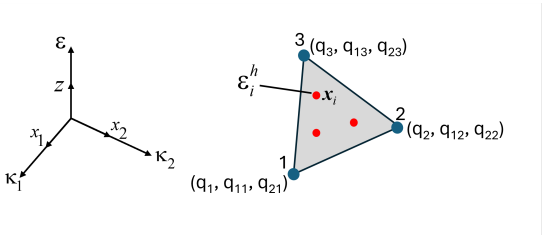

Figure 3.1 Three-node triangular smoothing element represented by its nodal DOFs.

the smoothed field is expressed as:

$$\varepsilon(\boldsymbol{x}) = \sum_{i=1}^{3} [\zeta_i(\boldsymbol{x})\, q_i + \zeta_{1i}(\boldsymbol{x})\, q_{1i} + \zeta_{2i}(\boldsymbol{x})\, q_{2i}] = \boldsymbol{N}\boldsymbol{q}^e \tag{3.4}$$

where q_i denotes the nodal value of the reconstructed field at node i, while q_{1i} and q_{2i} denote the auxiliary derivative degrees of freedom in the x_1 and x_2 directions, respectively. The interpolation is written in compact matrix form through the shape-function matrix $\boldsymbol{N}$ and the element nodal unknown vector $\boldsymbol{q}^e$. The auxiliary derivative fields are also interpolated over the same triangular element as:

$$\kappa_j(\boldsymbol{x}) = \sum_{i=1}^{3} \zeta_i(\boldsymbol{x})\, q_{ji}, \qquad j = 1, 2 \tag{3.5}$$

where κ_1 and κ_2 represent the reconstructed first-order derivative fields associated with the x_1 and x_2 directions. This formulation allows the field variable and its derivatives to be reconstructed within the same smoothing element in a consistent manner.

The matrix $\boldsymbol{N}$ and the element unknown vector $\boldsymbol{q}^e$ are defined as:

$$\boldsymbol{N} = \begin{bmatrix} \boldsymbol{N}_1 & \boldsymbol{N}_2 & \boldsymbol{N}_3 \end{bmatrix}, \qquad \boldsymbol{N}_i = \begin{bmatrix} \zeta_i & \zeta_{1i} & \zeta_{2i} \end{bmatrix}, \qquad i = 1, 2, 3 \tag{3.6}$$

$$\boldsymbol{q}^e = \begin{bmatrix} \boldsymbol{q}_1 & \boldsymbol{q}_2 & \boldsymbol{q}_3 \end{bmatrix}^T, \qquad \boldsymbol{q}_i = \begin{bmatrix} q_i & q_{1i} & q_{2i} \end{bmatrix}, \qquad i = 1, 2, 3 \tag{3.7}$$

where $\boldsymbol{N}_i$ contains the interpolation functions associated with node i, and $\boldsymbol{q}_i$ groups the nodal field value and the two auxiliary derivative degrees of freedom at the same node. In this way, each node carries three unknowns: the field value and its two directional derivatives.

The area coordinates of the triangular smoothing element are defined as:

$$\zeta_i = \frac{b_i x_1 + a_i x_2 + c_i}{2S}, \qquad i = 1,2,3 \tag{3.8}$$

with

$$a_i = x_{1k} - x_{1j}, \qquad b_i = x_{2j} - x_{2k}, \qquad c_i = x_{1j}x_{2k} - x_{1k}x_{2j} \tag{3.9}$$

$$S = \frac{1}{2}(a_3 b_2 - a_2 b_3) \tag{3.10}$$

This area is used in the construction of the element-level SEA matrices and in the integration of the smoothing functional over the triangular element. Using the cyclic permutation $(i,j,k) = (1,2,3),(2,3,1),(3,1,2)$, the quadratic enrichment functions are written as:

$$\zeta_{1i} = \frac{\zeta_i}{2}(a_k\zeta_j - a_j\zeta_k), \qquad \zeta_{2i} = \frac{\zeta_i}{2}(b_j\zeta_k - b_k\zeta_j) \tag{3.11}$$

where the enrichment terms are defined from the area coordinates and the geometric coefficients of the triangular element. These functions enrich the standard linear interpolation and allow the reconstructed field to include derivative-related contributions within the smoothing element. By substituting Eqs. (3.4)–(3.11) into Eq. (3.3) and minimizing the functional with respect to the nodal unknowns, the element-level SEA system is obtained as:

$$\frac{\partial F(\boldsymbol{q}^e)}{\partial \boldsymbol{q}^e} = 0 \Rightarrow \boldsymbol{A}^e \boldsymbol{q}^e = \boldsymbol{H}^e \tag{3.12}$$

where $\boldsymbol{A}^e$ is the element coefficient matrix and $\boldsymbol{q}^e$ is the vector of element unknowns. The element matrix is constructed from the data-fitting, derivative-consistency, and curvature-control contributions as:

$$\boldsymbol{H}^e = \frac{1}{n}\sum_{i=1}^{n}\left[\boldsymbol{N}^T(\boldsymbol{x}_i)\,\varepsilon_i^h\right] \tag{3.13}$$

and

$$\boldsymbol{A}^e = \frac{1}{n}\sum_{i=1}^{n}\left[\boldsymbol{N}^T(\boldsymbol{x}_i)\boldsymbol{N}(\boldsymbol{x}_i)\right] + \alpha\int_S \boldsymbol{B}_\alpha^T\boldsymbol{B}_\alpha\,dS + \beta S\int_S \boldsymbol{B}_\beta^T\boldsymbol{D}_\beta\boldsymbol{B}_\beta\,dS \tag{3.14}$$

with

$$\boldsymbol{D}_\beta = \begin{bmatrix} 1 & 0 & 0 \\ 0 & 1 & 0 \\ 0 & 0 & 0.5 \end{bmatrix} \quad \text{and} \quad \boldsymbol{B}_X = \begin{bmatrix} \boldsymbol{B}_X^1 & \boldsymbol{B}_X^2 & \boldsymbol{B}_X^3 \end{bmatrix}^T \quad (X = \alpha, \beta) \tag{3.15}$$

Here, $\boldsymbol{D}_\beta$ relates the reconstructed field to the auxiliary derivative variables, while $\boldsymbol{B}_\alpha$ and $\boldsymbol{B}_\beta$ contain the derivative terms associated with the derivative-consistency and curvature-control parts of the formulation. These matrices are given by:

$$\boldsymbol{B}_\alpha^i = \begin{bmatrix} \varepsilon_{i,1} & \zeta_{1i,1} - \zeta_i & \zeta_{2i,1} \\ \varepsilon_{i,2} & \zeta_{1i,2} & \zeta_{2i,2} - \zeta_i \end{bmatrix} \tag{3.16}$$

$$\boldsymbol{B}_\beta^i = \begin{bmatrix} 0 & \zeta_{1i,1} & 0 \\ 0 & 0 & \zeta_{2i,2} \\ 0 & \zeta_{2i,2} & \zeta_{1i,1} \end{bmatrix} \tag{3.17}$$

After assembling all smoothing elements over the measurement domain, the resulting global SEA system is solved independently for $u(\boldsymbol{x})$ and $v(\boldsymbol{x})$. Thus, the raw displacement data are converted into continuous smoothed displacement fields. These smoothed displacement fields provide the basis for the strain reconstruction step described in the following section.

3.1.4 Reconstruction of the In-Plane Strain Field

Once the smoothed displacement field is obtained, the in-plane strain components are reconstructed under the infinitesimal-strain assumption. The normal and engineering shear strain components are given by:

$$\begin{aligned} \varepsilon_{11} &= u_{,1} \\ \varepsilon_{22} &= v_{,2} \\ \gamma_{12} &= u_{,2} + v_{,1} \end{aligned} \tag{3.18}$$

The resulting strain vector is written as:

$$\boldsymbol{\varepsilon}(\boldsymbol{x}) = \begin{bmatrix} \varepsilon_{11}(x) \\ \varepsilon_{22}(x) \\ \gamma_{12}(x) \end{bmatrix} \tag{3.19}$$

This first SEA stage therefore serves a clear purpose: it stabilizes the displacement-to-strain transition. Since the strain components are obtained by differentiating the displacement field, a direct evaluation from raw DIC outputs could lead to local oscillations and unstable strain contours. By reconstructing the strain field from smoothed displacement components, the resulting strain quantities become more suitable for scalar strain reduction and subsequent gradient-based localization analysis.

3.1.5 Equivalent Von Mises Strain

After obtaining the in-plane strain components, an equivalent strain measure is introduced to represent the multi-component strain state by a single scalar field. In the present study, the von Mises equivalent strain is adopted and written in terms of the in-plane strain components as:

$$\varepsilon_{vm} = \sqrt{\varepsilon_{11}^2 - \varepsilon_{11}\varepsilon_{22} + \varepsilon_{22}^2 + \frac{3}{4}\gamma_{12}^2} \tag{3.20}$$

The von Mises equivalent strain was used as a scalar measure of the overall in-plane deformation intensity. In this study, it is not intended to represent an isotropic yielding criterion or a failure criterion for composite laminates. Since the tested specimens are anisotropic laminated composites, their damage and failure behavior depends on ply orientation, crack direction, and local strain distribution. Therefore, the von Mises equivalent strain is used only as a convenient scalar field for post-processing the reconstructed strain components.

This scalar representation is useful because the dominant strain component may vary depending on the laminate configuration and crack orientation. For this reason, using only one strain component, such as ε_{11}, ε_{22}, or γ_{12}, may not provide a consistent basis for comparing different specimens. The von Mises equivalent strain combines the reconstructed in-plane normal and shear strain components into a sin-

gle continuous field, which can then be smoothed and differentiated in a consistent way. In addition, this choice avoids the need for orthotropic stiffness parameters or ply-level constitutive assumptions, which would be required for strain-energy-based quantities. Thus, the equivalent strain field is used here as a practical input for the gradient-based localization index, rather than as a material failure model.

3.1.6 Smoothing of the Von Mises Strain Field

Although the strain field has already been reconstructed from a smoothed displacement field, the von Mises strain field may still contain local irregularities inherited from the strain combination step. This becomes especially important because the final localization index is not based only on the strain level itself, but also on the spatial gradient of the equivalent strain field. Since gradient computation is particularly sensitive to local fluctuations, a second smoothing stage is introduced at this point.

Accordingly, the equivalent strain field ε_{vm} is treated as a scalar experimental field and smoothed once again by using the same SEA formulation given in Eqs. (3.3)–(3.17). In this second application, the role of SEA is no longer to stabilize the displacement-to-strain transition, but to regularize the scalar equivalent-strain field before gradient evaluation. The output of this stage is the smoothed von Mises strain field, denoted here by $\bar{\varepsilon}_{vm}(\boldsymbol{x})$.

The distinction between the two SEA stages is important. The first SEA stage acts on the displacement field and primarily supports reliable strain reconstruction. The second SEA stage acts on the equivalent strain field and primarily supports stable gradient evaluation. In this sense, the present methodology is not based on a repeated use of the same operation for the same purpose; rather, the two SEA stages are introduced at two different sensitivity points of the processing chain.

3.1.7 Gradient of the Smoothed Von Mises Strain Field

Once the smoothed equivalent strain field $\bar{\varepsilon}_{vm}$ is obtained, its spatial gradient is computed as:

$$\nabla \bar{\varepsilon}_{vm} = \begin{bmatrix} \dfrac{\partial \bar{\varepsilon}_{vm}}{\partial x_1} \\ \dfrac{\partial \bar{\varepsilon}_{vm}}{\partial x_2} \end{bmatrix} \tag{3.21}$$

and the corresponding gradient magnitude is written as:

$$\|\nabla \bar{\varepsilon}_{vm}\| = \left[\left(\frac{\partial \bar{\varepsilon}_{vm}}{\partial x_1} \right)^2 + \left(\frac{\partial \bar{\varepsilon}_{vm}}{\partial x_2} \right)^2 \right]^{1/2} \tag{3.22}$$

The gradient magnitude identifies regions where the equivalent strain field changes rapidly in space. In cracked composite laminates, such regions are expected to be associated with crack-tip deformation, strain concentration, and localized damage development.Therefore, the second SEA stage is introduced to ensure that the computed gradient reflects the spatial localization of the equivalent strain field rather than local numerical roughness. In practical implementation, the gradient may be evaluated over the SEA post-processing mesh or over a structured grid derived from the reconstructed field. In either case, the second SEA stage is introduced to reduce the sensitivity of the gradient calculation to residual local fluctuations and to provide a more controlled basis for the localization-amplification term used in the following section.

3.1.8 Gradient-Enhanced Damage-Sensitive Localization Index

The final localization measure is defined through a gradient-enhanced damage-sensitive index that combines a strain-threshold term with a localization-amplification term. Three candidate formulations are considered to clarify the role of strain thresholding, gradient amplification, and bounded normalization.

The first candidate, D_1, is based solely on the gradient magnitude of the smoothed von Mises equivalent strain field:

$$D_1 = \|\nabla \bar{\varepsilon}_{vm}\| \tag{3.23}$$

This formulation identifies regions of rapid spatial variation in the equivalent strain field. However, because it does not include any strain-level criterion, it may activate in regions where the strain magnitude is relatively low but local spatial variation is still present. Therefore, D_1 is useful for visualizing strain-gradient activity, but it is not sufficiently selective for crack-sensitive localization.

The second candidate, D_2, couples a strain-threshold term with a gradient-based localization-amplification term:

$$D_2 = \max\left(0, \frac{\bar{\varepsilon}_{vm} - \varepsilon_c}{\varepsilon_c}\right)\left(1 + \ell \frac{\|\nabla \bar{\varepsilon}_{vm}\|}{\varepsilon_c}\right) \tag{3.24}$$

Here, ε_c is a reference strain threshold, in $\mu\varepsilon$, and ℓ is a characteristic length (element length), in mm, controlling the contribution of spatial localization to the final index. The first factor in Eq. (3.24) acts as a threshold function. It ensures that the damage index remains inactive as long as the equivalent strain stays below the reference initiation level. Once this level is exceeded, the index becomes positive and grows with increasing strain. The second factor amplifies the damage index in regions where the equivalent strain field is spatially localized. Therefore, the index does not respond only to high strain levels, but also to high strain concentration. This is particularly useful in crack-sensitive regions, where both large strain values and strong spatial localization are expected. Because D_2 is unbounded, however, its absolute values are strongly influenced by the magnitude of the gradient term and the choice of ε_c, which complicates direct comparison.

The third candidate, D_3, retains the structure of Eq. (3.24) but introduces a bounded normalization:

$$D_3 = \frac{D_2}{1 + D_2} \tag{3.25}$$

In this formulation, the unbounded D_2 field is transformed into a bounded localization index. As D_2 increases, D_3 approaches unity asymptotically, while lower D_2 values remain proportionally represented. Therefore, normalization does not clip the field abruptly; instead, it compresses large localization values into a consistent range between 0 and 1. This provides a more stable and interpretable scale for comparing different specimens, crack orientations, and loading stages while preserving the spatial localization pattern obtained from D_2.

It is important to note that the present quantities are introduced as damage-sensitive

localization indicators rather than constitutive failure criteria or crack-growth laws. In other words, Eq. (3.24) and Eq. (3.25) are used to identify spatial regions that are more likely to correspond to crack-sensitive localization. The parameter ε_c should therefore be interpreted as a reference initiation threshold for damage sensitivity, not as the final failure strain of the material. Similarly, the characteristic length ℓ serves as a scaling parameter that links the localization contribution to the spatial resolution of the post-processing framework. With the updated D_3 formulation, the final localization map preserves the threshold-gradient sensitivity of D_2 while expressing the response on a bounded and comparable scale.

Accordingly, D_3 should be interpreted as a localization indicator derived from the measured deformation field, not as a ply-level failure index or a constitutive damage variable. Regions with elevated values of D_3 indicate locations where the equivalent strain is both sufficiently high and sufficiently localized. Such regions are therefore regarded as likely damage zones or crack-sensitive regions.

3.1.9 Quantitative Pre-Failure Localization Assessment

To support the visual interpretation of the D_3 localization maps, a quantitative pre-failure localization assessment has been introduced. The analyzed DIC frames correspond to the final reliable pre-failure stages rather than the completely fractured state. Therefore, the aim of this assessment is not to measure the full overlap between the final crack path and the D_3 field. Instead, it evaluates whether the high-D_3 regions have developed close to the initial crack-tip zones and whether their dominant orientations are consistent with the experimentally observed crack-propagation directions.

For each specimen, the final reliable D_3 map has been thresholded to isolate the most strongly activated localization regions. Before applying a single threshold value to all specimens, a threshold assessment has been carried out using $\tau = 0.5$, 0.6, and 0.7. This assessment has shown that the crack-tip proximity distance remains unchanged for the tested threshold values, while the orientation difference remains within a low range. Based on this comparison, the threshold ratio has been selected as $\tau = 0.6$ for the full quantitative evaluation. Accordingly, the high-D_3 elements have been defined as:

$$D_3 \geq \tau \times D_{3,\max} \tag{3.26}$$

where $D_{3,\max}$ is the maximum value of the D_3 field in the corresponding map. The same threshold ratio has been used for all specimens to maintain a consistent quantitative comparison. The selected value $\tau = 0.6$ provides a balanced definition of the high-localization region by retaining the main D_3 bands while avoiding the inclusion of weakly activated regions away from the crack-tip zones. It also preserves enough high-D_3 elements for PCA-based orientation estimation.

After thresholding, the centroid coordinates of the high-D_3 elements have been assigned to the nearest initial crack tip. This allows the localization response around each crack tip to be evaluated separately. For each crack tip, the minimum distance between the initial crack-tip coordinate and the corresponding high-D_3 region has been calculated as:

$$d_{\min} = \min |x_{D3} - x_{tip}| \tag{3.27}$$

where x_{D_3} is the centroid coordinate of a high-D_3 element and x_{tip} is the coordinate of the corresponding initial crack tip. A lower value of $d_{\min}$ indicates that the D_3 field has activated closer to the mechanically critical crack-tip region before final fracture.

In addition to the crack-tip proximity distance, the dominant orientation of each high-D_3 localization band has been calculated using principal component analysis (PCA). PCA has been applied to the centroid coordinates of the thresholded high-D_3 elements assigned to each crack tip. In this calculation, the D_3 value of each element has been used as a weighting factor, so that elements with higher D_3 values have a stronger influence on the estimated localization direction. The dominant orientation θ_{D_3} has been taken as the direction of the principal axis associated with the largest eigenvalue of the weighted covariance matrix.

The calculated D_3 orientation has then been compared with the experimentally observed crack-propagation direction θ_{crack}. The orientation difference has been defined as the smallest angular difference between these two directions:

$$\Delta\theta = |\theta_{D_3} - \theta_{\text{crack}}| \tag{3.28}$$

with the directional equivalence of 0° and 180° considered. To express this angular difference in a normalized form, the percentage orientation difference has been calculated as:

$$\text{Percentage Difference}\,(\%) = (\Delta\theta/180) \times 100 \tag{3.29}$$

Accordingly, smaller d_{tip} and percentage difference values indicate better agreement

between the pre-failure localization band and the experimentally observed crack-propagation direction.

3.2 Results and Discussion

The proposed dual-stage SEA-assisted DIC framework is evaluated using the cracked composite laminate specimens described in Chapter 2. For each specimen and selected loading stage, the full processing chain is applied from raw DIC displacement measurements to the final gradient-enhanced damage-sensitive localization map. The results are presented in two main parts. First, the SEA-based post-processing framework is verified through displacement-field comparison, strain-gauge-supported strain evaluation, interpretation of the von Mises equivalent strain and its spatial derivatives, and comparison of the candidate localization indices. Second, the selected D_3-based formulation is applied to all tested laminate configurations to assess its ability to track crack-sensitive localization patterns and crack propagation. This structure allows the framework to be evaluated at different levels of the processing chain. The displacement comparison examines whether the first SEA stage preserves the measured DIC displacement response. The strain comparison evaluates whether the reconstructed strain fields remain consistent with independent local strain-gauge measurements. The von Mises strain and derivative fields are then examined to interpret the physical basis of the gradient-enhanced index. Finally, the D_3-based localization maps are compared with the experimentally observed crack paths, and quantitative pre-failure localization metrics are used to support the visual interpretation of the results.

3.2.1 Verification of the SEA-Based Processing Framework

The proposed framework is verified by examining the intermediate and final outputs of the SEA-based processing chain. For each selected loading stage, the raw DIC displacement data are mapped onto the SEA post-processing mesh. The first SEA stage is then applied to reconstruct continuous displacement fields, and the corresponding strain components are obtained from the smoothed displacement field. After that, the von Mises equivalent strain field is calculated and regularized by the

second SEA stage before gradient evaluation. This section evaluates the consistency of the reconstructed fields before applying the final damage-sensitive localization index to the full specimen set. The displacement-field comparison assesses whether the first SEA stage preserves the measured DIC response, while the strain-gauge comparison evaluates the consistency of the reconstructed strain fields with independent local measurements. The von Mises strain and derivative fields are then examined to support the use of the gradient-enhanced localization index.

3.2.1.1 Total Displacement Comparison

The first step in the implementation is the construction of a triangular smoothing element mesh over the DIC measurement domain. A structured triangular mesh is generated to cover the region of interest of each specimen, with an element density selected to capture the displacement gradients expected around the crack region. The mesh configuration and the mapping of DIC points onto the SEA mesh are illustrated in Figure 3.2. In this mapping procedure, each valid DIC measurement point is assigned to the triangular element in which it is located. The corresponding in-plane displacement components are then used as discrete experimental inputs for the SEA formulation. In this way, the scattered DIC displacement measurements are transferred to the SEA post-processing mesh while preserving their spatial positions within the measurement domain.

Once the mesh and the discrete displacement data set are established, the first SEA stage is applied independently to each in-plane displacement component. The global SEA system is assembled and solved as described in Section 3.1.3, resulting in continuous smoothed displacement fields over the measurement domain. The total displacement fields obtained by combining the smoothed in-plane components are compared with the corresponding raw DIC fields in Figures 3.3 and 3.4 for two representative specimens: the 0/90/0 laminate with a 90° initial crack orientation and the 0/90/0 laminate with a 45° initial crack orientation. In each figure, the displacement contours are presented at two representative steps, 70 and 100, to evaluate the SEA reconstruction at both an intermediate and a later loading stage. These two specimens are selected because they have the same laminate architecture but different initial crack orientations, allowing the influence of crack direction on the displacement field to be examined under a controlled comparison.

The contour maps show that the SEA-reconstructed displacement fields reproduce

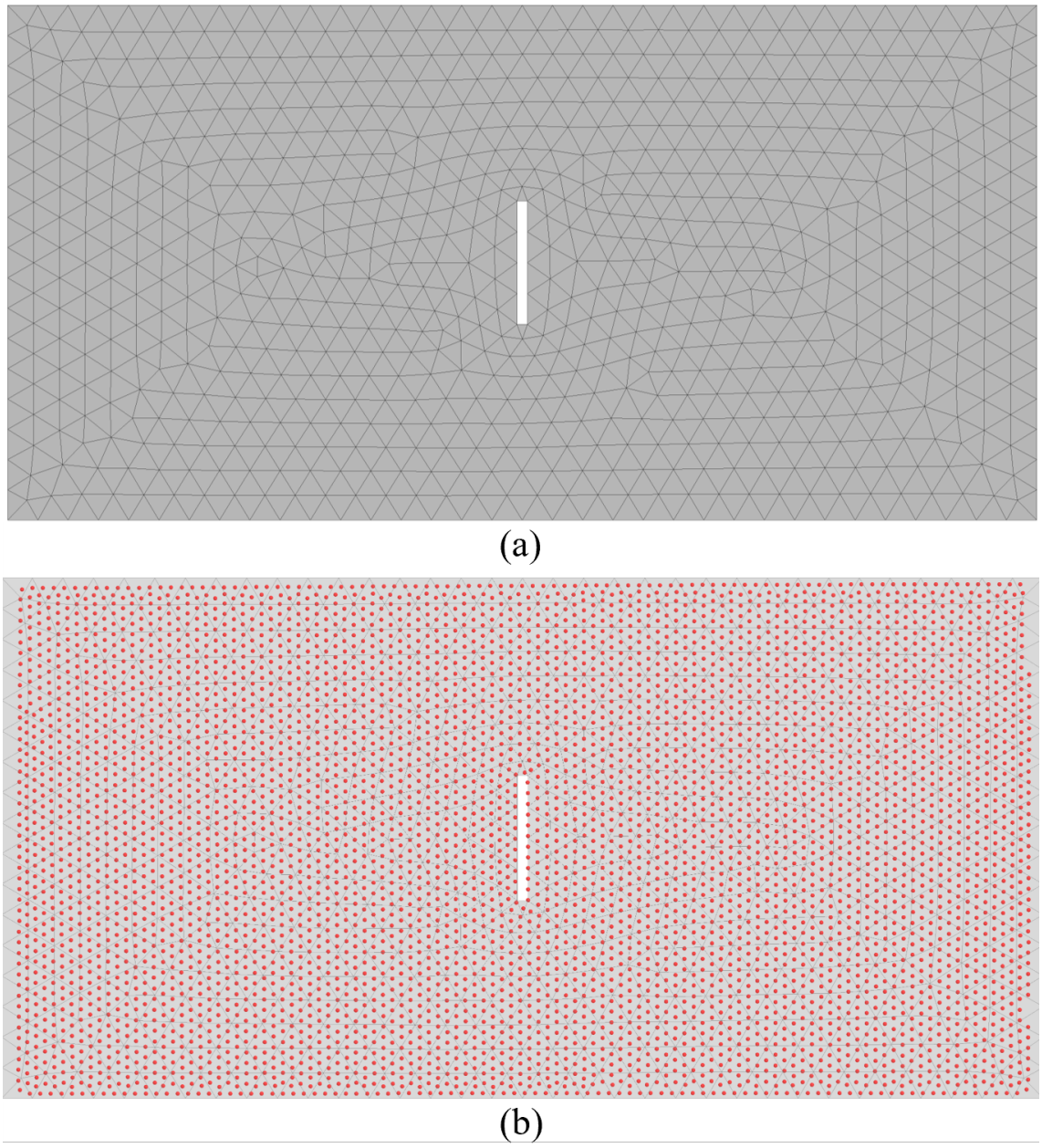

Figure 3.2 SEA-based mapping procedure used for DIC displacement data: (a) triangular smoothing element mesh generated over the specimen region, and (b) raw DIC displacement measurement points projected onto the SEA triangular mesh for subsequent field reconstruction.

the overall spatial distribution of the measured DIC fields with good consistency in both specimens and at both loading stages. For the 0/90/0 specimen with a 90° initial crack orientation, the maximum total displacement at step 70 is 0.376 mm in the DIC field and 0.382 mm in the SEA field, corresponding to a relative difference of approximately 1.57%. At step 100, the maximum displacement increases to 0.499 mm for DIC and 0.510 mm for SEA, with a relative difference of approx-

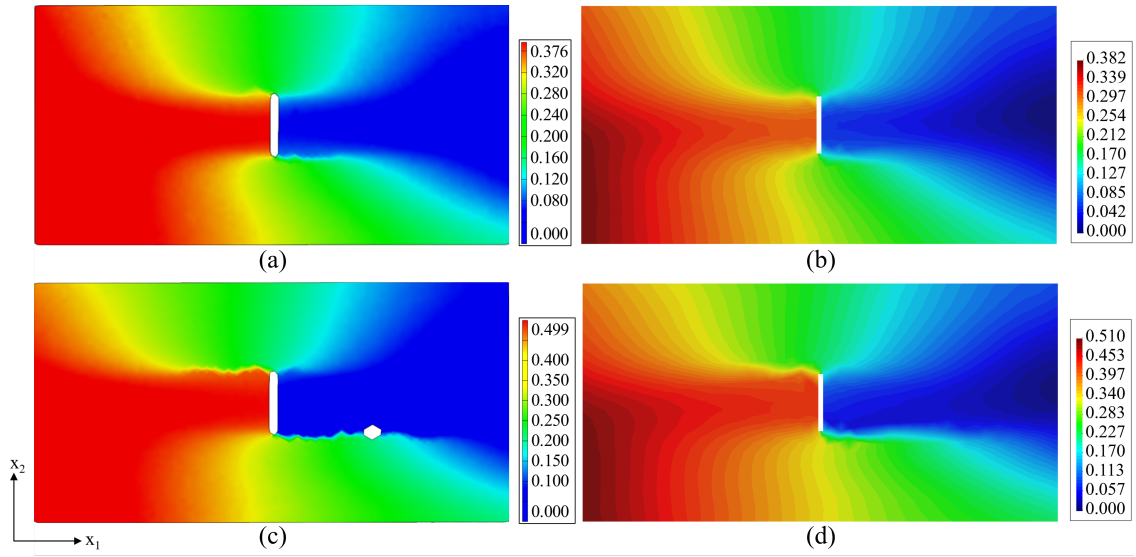

Figure 3.3 Comparison of DIC-measured and SEA-reconstructed total displacement [mm] fields for the 0/90/0 laminate with a 90° initial crack orientation: (a) DIC field at step 70, (b) SEA field at step 70, (c) DIC field at step 100, and (d) SEA field at step 100.

imately 2.15%. For the 0/90/0 specimen with a 45° initial crack orientation, the maximum total displacement at step 70 is 0.409 mm for DIC and 0.410 mm for SEA, corresponding to a relative difference of approximately 0.24%. At step 100, the corresponding maximum values are 0.505 mm and 0.513 mm, with a relative difference of approximately 1.58%.

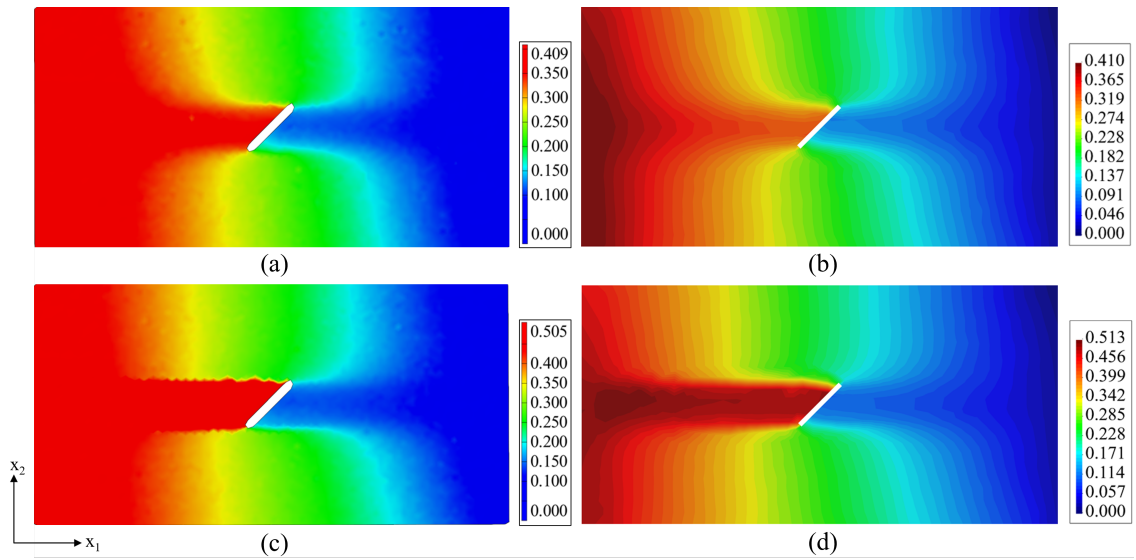

Figure 3.4 Comparison of DIC-measured and SEA-reconstructed total displacement [mm] fields for the 0/90/0 laminate with a 45° initial crack orientation: (a) DIC field at step 70, (b) SEA field at step 70, (c) DIC field at step 100, and (d) SEA field at step 100.

These low relative differences indicate that the SEA reconstruction preserves the displacement magnitude obtained from the DIC measurements with good accuracy. At the same time, the SEA contours retain the overall deformation pattern of the DIC fields while reducing local point-to-point scatter and correlation-induced fluctuations. Therefore, the first SEA does not significantly alter the measured displacement response. Instead, it provides a spatially regularized displacement field that remains quantitatively consistent with the raw DIC data and suitable for the subsequent strain reconstruction step.

To provide a further quantitative assessment, line-based comparisons are performed along the horizontal centerline of each representative specimen, corresponding to the x_1-axis passing through the mid-height of the measurement domain. The DIC and SEA total displacement profiles extracted along this line at step 100 are plotted in Figure 3.5. The mean relative error along the centerline is 1.89% for the 0/90/0 specimen with a 90° initial crack orientation and 2.26% for the 0/90/0 specimen with a 45° initial crack orientation.

These results show that first SEA produces displacement fields that remain in close quantitative agreement with DIC data. At the same time, the reconstructed fields provide spatial regularity required for the subsequent strain reconstruction.

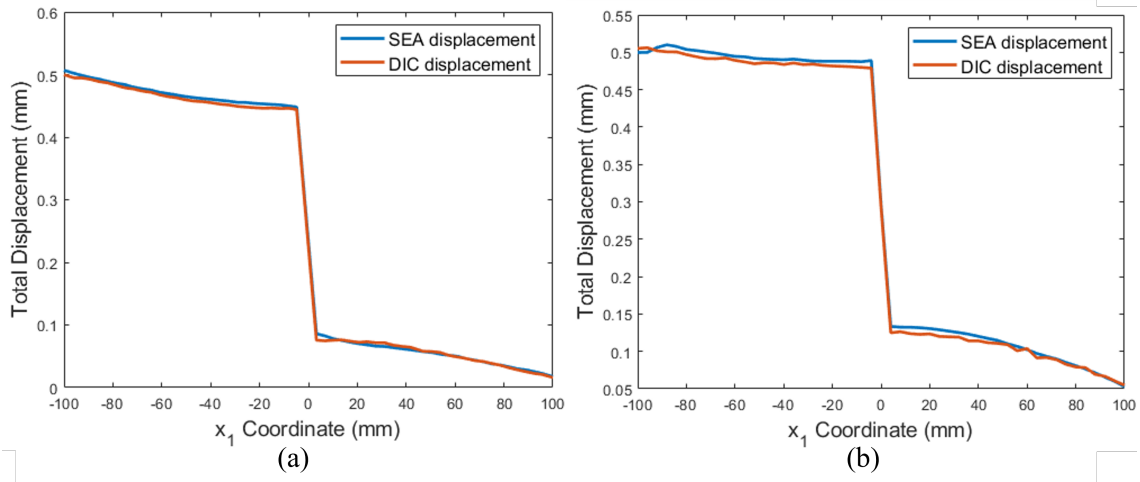

Figure 3.5 Line-based comparison of DIC-measured and SEA-reconstructed total displacement [mm] distributions along the specimen centerline at step 100: (a) 0/90/0 laminate with a 90° initial crack orientation and (b) 0/90/0 laminate with a 45° initial crack orientation.

3.2.1.2 Comparison of SEA-Based Strain with Strain-Gauge Measurements

To assess the consistency of the SEA-reconstructed strain fields with independent local measurements, strain-gauge data is used as a pointwise reference. Two comparison lines are defined across the specimen, and the strain-gauge locations are projected onto these lines, as shown in Figure 3.6. This layout enables the continuous strain distributions obtained from SEA to be evaluated together with the discrete strain-gauge measurements within the same geometrical reference.

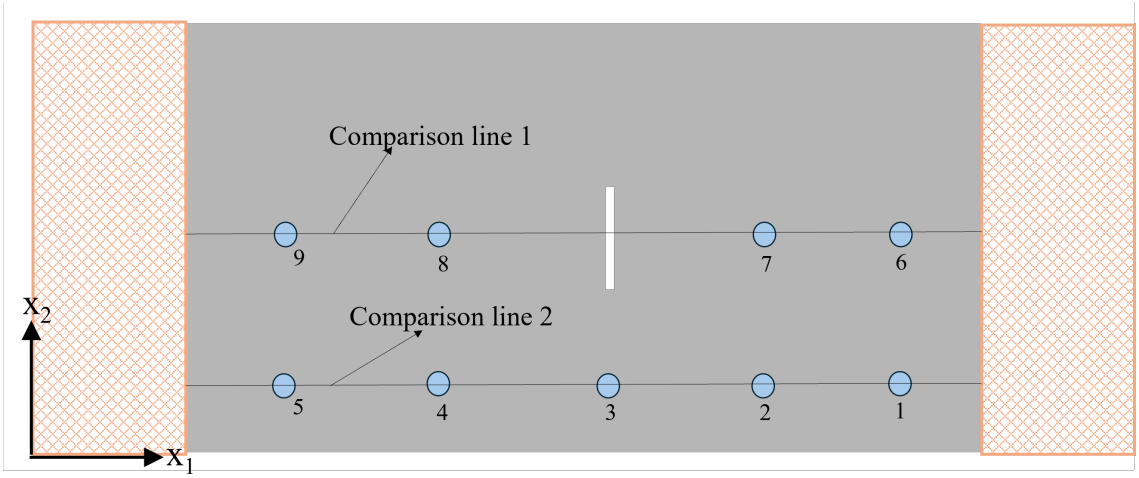

Figure 3.6 Definition of comparison lines used for evaluating SEA-reconstructed strain fields against strain-gauge measurements.

The comparison is presented in detail for the first representative case. The same comparison procedure is also applied to the remaining strain-gauge-instrumented specimens; however, only the representative case is shown here to avoid repetition and to keep the focus on the validation of the reconstructed strain-field trend. In the plots, the notation SEA-i denotes the SEA-reconstructed strain extracted at the location of the corresponding strain gauge SG-i. Therefore, SEA-i does not represent an additional physical sensor.

The comparison is first performed in the time domain at the selected strain-gauge locations for the 0/0/0 laminate with a 90° initial crack orientation. As shown in Figure 3.7(a)-(d), the strain histories extracted from the SEA-reconstructed fields follow the overall evolution of the strain-gauge measurements throughout the loading process. In particular, the SEA-based results reproduce the dominant increasing and decreasing trends observed in the experimental strain histories, indicating that the reconstructed strain field remains consistent with the local strain response measured

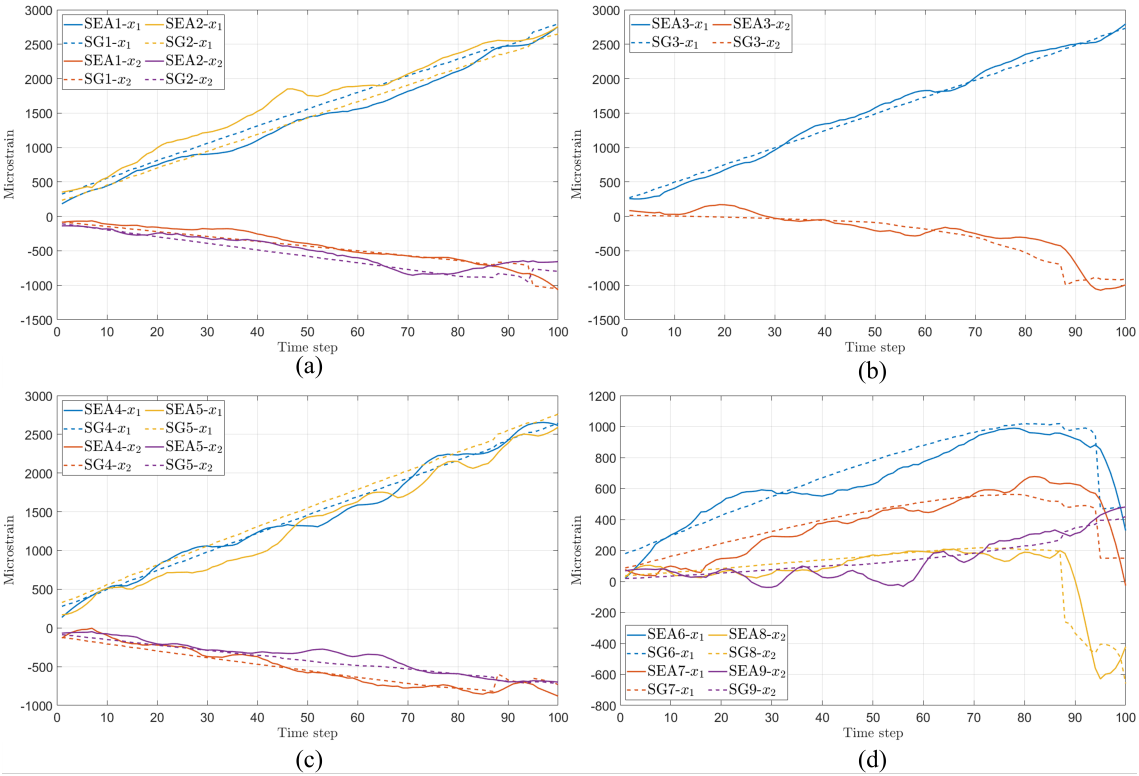

Figure 3.7 Time-history comparison between SEA-reconstructed strains and strain-gauge measurements at selected gauge locations: (a) SG1–SG2, (b) SG3, (c) SG4–SG5, and (d) SG6–SG9. Solid lines represent SEA-reconstructed strain histories extracted at the corresponding gauge locations, while dashed lines represent strain-gauge measurements in the x_1 and x_2 directions.

at representative points of the specimen.

Although local deviations are observed at some loading stages, especially as the deformation field becomes more non-uniform near the crack region, the overall agreement between the two measurement approaches is satisfactory. These deviations are expected because the SEA results represent continuous full-field reconstruction derived from DIC measurements, whereas strain gauges provide local average measurements over finite gauge lengths. Therefore, exact pointwise coincidence is not required; rather, the objective is to verify whether the SEA-reconstructed field captures the experimentally measured strain trends and local strain levels with reasonable consistency.

A complementary comparison is then carried out in the spatial domain at a representative loading stage, step 50, for the same specimen. For this purpose, the strain distribution along each comparison line is plotted together with the strain-gauge values measured at the corresponding locations, as shown in Figure 3.8. In these

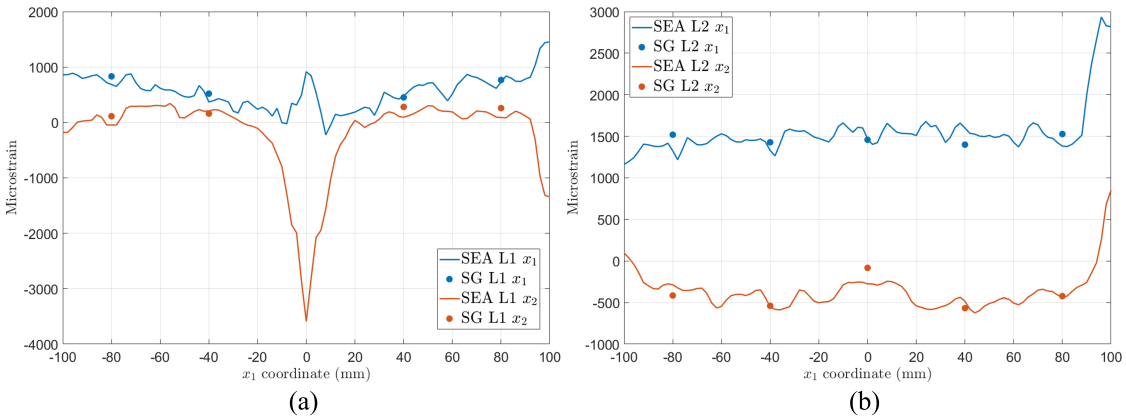

Figure 3.8 Strain comparison between SEA-reconstructed fields and strain-gauge measurements along the selected comparison lines at time step 50: (a) comparison line 1 and (b) comparison line 2.

figures, the SEA results are represented as continuous line distributions, whereas the strain-gauge measurements are shown as discrete points. This representation makes it possible to examine not only the point-wise agreement at the gauge locations, but also the surrounding spatial variation of the reconstructed strain field along the entire line. The line-based comparisons show that the strain-gauge values are generally compatible with the local levels predicted by the SEA-derived strain distributions. At the same time, the continuous SEA fields reveal the broader spatial strain variation along the selected lines, which cannot be captured by discrete strain gauges alone. This is particularly important near the central cracked region, where stronger strain gradients and pronounced spatial non-uniformity are expected. Therefore, the comparison indicates that the SEA reconstruction provides a continuous strain field that remains physically consistent with independent local strain-gauge data.

3.2.1.3 Von Mises Strain and Derivative Fields

Following the first SEA stage, the in-plane strain components are reconstructed from the smoothed displacement fields, as described in Section 3.1.4. The von Mises equivalent strain field is then calculated according to Eq. (3.20). Before evaluating the spatial derivatives, the von Mises strain field is regularized by the second SEA stage to reduce local fluctuations that may affect gradient calculation. The resulting equivalent strain field and its spatial derivatives in the x_1- and x_2-directions are presented in Figure 3.9 for two representative specimens. Figures 3.9(a)–(c) show the 0/90/0 laminate with a 90° initial crack orientation, while Figures 3.9(d)–(f)

show the 0/90/0 laminate with a 45° initial crack orientation.

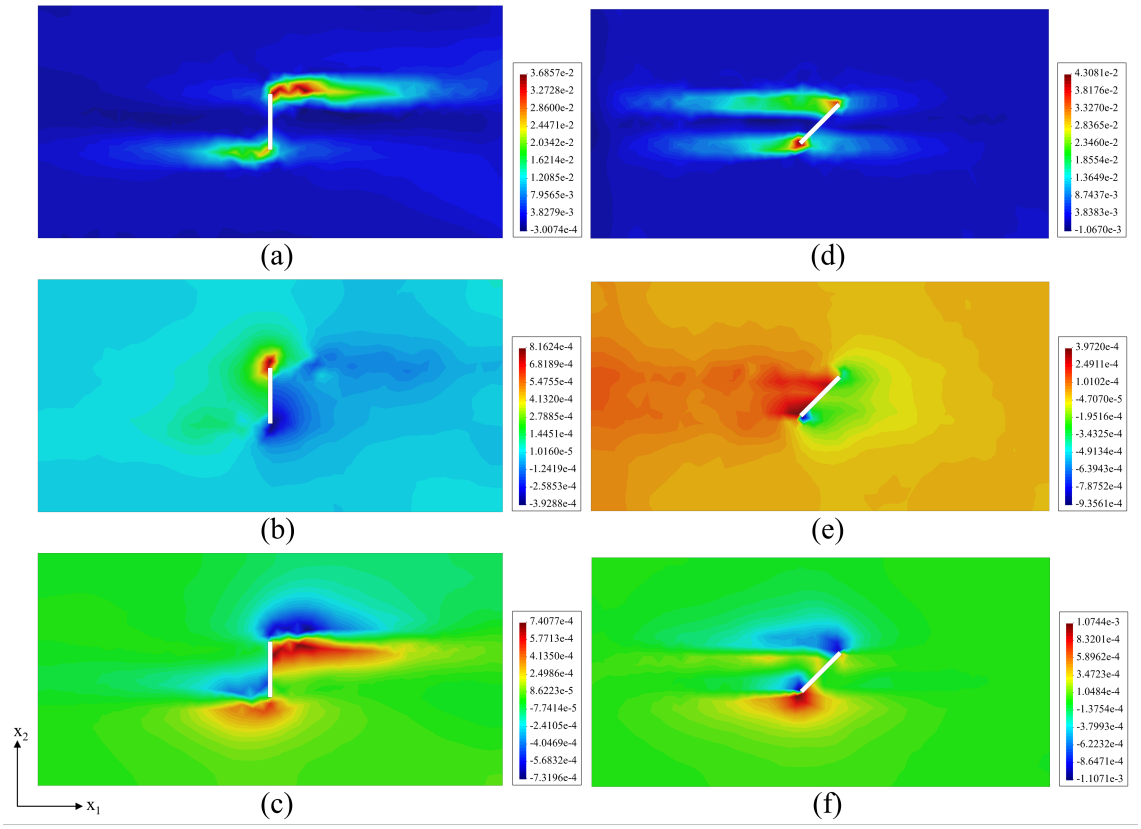

Figure 3.9 Von Mises equivalent strain and spatial derivative fields for the 0/90/0 laminate: (a) von Mises strain, (b) x_1-direction derivative, and (c) x_2-direction derivative for the 90° initial crack orientation; and (d) von Mises strain, (e) x_1-direction derivative, and (f) x_2-direction derivative for the 45° initial crack orientation.

The von Mises strain contours in Figures 3.9(a) and 3.9(d) show that the equivalent strain field is mainly concentrated around the crack-tip regions in both configurations. For the 90° crack case, the maximum von Mises strain reaches 3.69×10^{-2}, and the elevated strain region develops more symmetrically around the two crack tips. This distribution is consistent with the crack being perpendicular to the loading direction, where deformation is expected to localize around both crack-tip regions. For the 45° crack case, the maximum von Mises strain reaches 4.31×10^{-2}, and the strain concentration becomes more asymmetric. In this case, the dominant high-strain region shifts according to the oblique crack orientation, indicating that the initial crack angle affects the spatial distribution of the localized strain field.

The x_1-direction derivative fields in Figures 3.9(b) and 3.9(e) describe the horizontal rate of change of the smoothed von Mises strain field. For the 90° crack case, the derivative map shows a clear sign change around the crack-tip region, with

positive and negative derivative zones developing on opposite sides of the localized strain field. The maximum and minimum derivative values are 8.16×10^{-4} and -3.93×10^{-4}, respectively. For the 45° crack case, a similar sign-changing derivative pattern is observed, but the distribution is rotated and shifted according to the oblique crack geometry. In this case, the maximum and minimum derivative values are 3.97×10^{-4} and -9.36×10^{-4}, respectively.

The x_2-direction derivative fields in Figures 3.9(c) and 3.9(f) represent the vertical rate of change of the smoothed von Mises strain field. For the 90° crack case, the derivative field is concentrated near the crack-tip region, with maximum and minimum values of 7.41×10^{-4} and -7.32×10^{-4}, respectively. For the 45° crack case, the derivative distribution again follows the orientation-dependent localization pattern, with maximum and minimum values of 1.07×10^{-3} and -1.11×10^{-3}, respectively. The larger derivative magnitudes observed in the 45° case indicate a sharper spatial variation of the equivalent strain field at the selected loading stage.

Overall, the results in Figure 3.9 indicate that the derivative fields obtained after the second SEA stage remain spatially coherent and consistent with the localization pattern of the equivalent strain field. The derivative maps highlight regions where the equivalent strain changes rapidly in space, particularly around the crack-tip zones. These observations support the use of the smoothed equivalent strain field as the input for the gradient-enhanced damage-sensitive localization index.

3.2.1.4 Selection of the Damage-Sensitive Localization Index

Before applying the proposed framework to the full specimen set, the three candidate (D_1, D_2, D_3) formulations introduced in Eqs. (3.23)–(3.25) are compared on the same SEA-processed equivalent strain field. In the present implementation, the reference damage-initiation strain is set to $\varepsilon_c = 0.01$ (corresponding to 10,000 $\mu\varepsilon$) and the characteristic length is taken as $\ell = 2$ mm, consistent with the element length of the SEA post-processing mesh.

D_1, which is based only on the gradient magnitude $\|\nabla \bar{\varepsilon}_{vm}\|$, is shown in Figures 3.10(a) and 3.10(d). For both crack orientations, D_1 highlights the regions where the equivalent strain field changes rapidly in space. However, the activated regions are relatively broad and are not limited to the crack-tip zones. Elevated values also appear along the crack flanks and in parts of the surrounding field. This

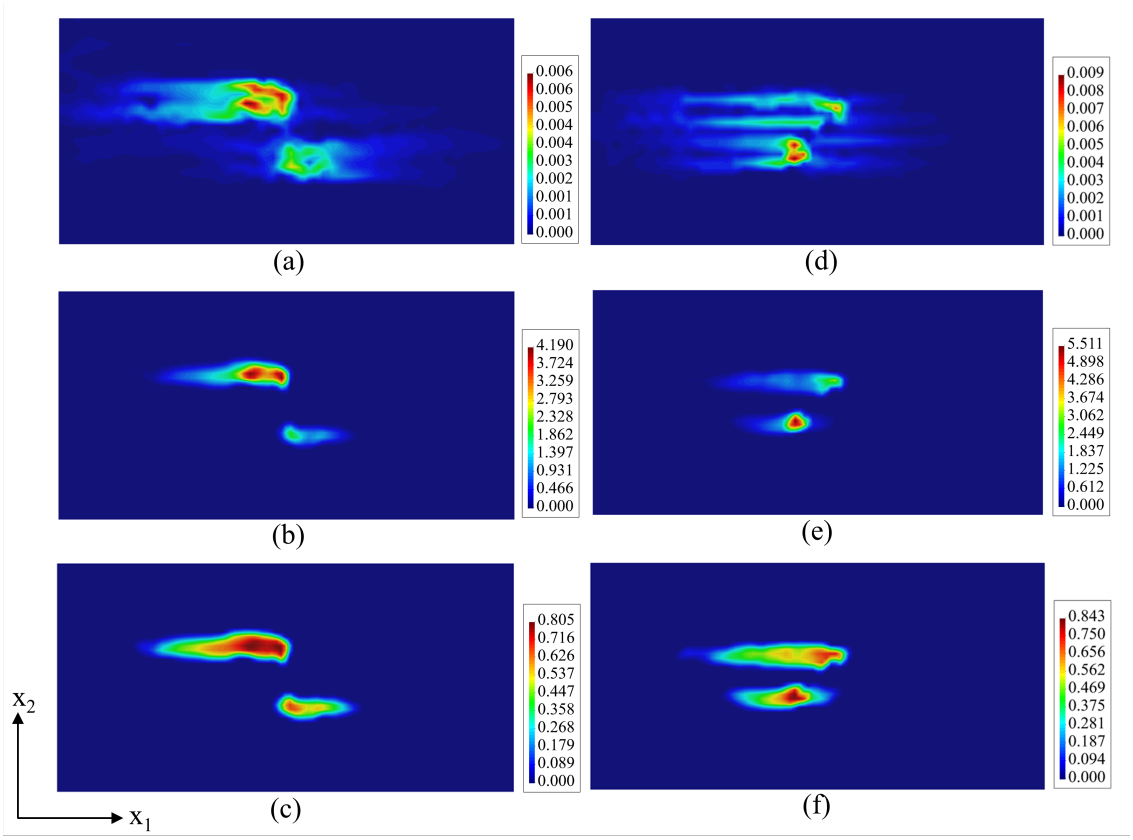

Figure 3.10 Comparison of damage indicator formulations for the 0/90/0 laminate: (a–c) D_1, D_2, and D_3 for the 90° initial crack orientation, and (d–f) D_1, D_2, and D_3 for the 45° initial crack orientation at step 100.

behavior indicates that a purely gradient-based formulation is sensitive to spatial variations in the strain field, but it does not distinguish whether these variations occur in regions of sufficiently high strain. Therefore, D_1 is useful for visualizing gradient activity, but it is not selective enough for crack-sensitive localization.

D_2 combines a strain-threshold term with a gradient-based localization-amplification term, as shown in Figures 3.10(b) and 3.10(e). Compared with D_1, the active regions become more concentrated around the crack tips because the index is activated only where the equivalent strain exceeds the selected reference threshold. For the 90° initial crack orientation, D_2 reaches a maximum value of 4.190, while for the 45° initial crack orientation, the maximum value increases to 5.511. These results show that D_2 provides a clearer response to localization than D_1 by combining strain level and spatial gradient information. However, since D_2 is unbounded, its absolute magnitude is strongly influenced by the local gradient intensity. This makes direct comparison between different specimens, crack orientations, or loading stages less straightforward.

D_3 retains the threshold-gradient structure of D_2 but introduces a bounded nonlinear normalization, as shown in Figures 3.10(c) and 3.10(f). In both crack configurations, the high-index regions remain concentrated near the crack-tip zones, while the index values are transformed into a more interpretable range between 0 and 1. Unlike a direct clipping operation, the adopted normalization compresses the unbounded D_2 response through Eq. (3.25). Therefore, larger D_2 values lead to progressively higher D_3 values, but the index approaches unity asymptotically rather than exceeding it. Based on the maximum D_2 values, the maximum D_3 values are approximately 0.807 for the 90° initial crack orientation and 0.846 for the 45° initial crack orientation. This indicates that D_3 preserves the spatial localization sensitivity of D_2 while reducing the dominance of very large gradient-amplified values. The contour plots in Figure 3.10 are generated using the smoothed post-processing representation available in GiD. During this visualization step, integration-point results are projected and averaged to obtain a continuous contour field. Therefore, the color-scale maximum may slightly differ from the direct numerical maximum of the computed localization field. This difference is only related to the contour-plotting procedure and does not affect the formulation or the interpretation of the crack-sensitive localization pattern.

Based on this comparison, D_3 is selected as the damage-sensitive localization index for the remainder of the study. By converting the unbounded D_2 response into a normalized index, the final maps remain comparable across specimens and loading stages without losing the crack-sensitive spatial pattern. The selected D_3 maps are therefore used in the following section to monitor the evolution of crack-sensitive high-index regions and to compare the predicted localization patterns with the experimentally observed crack paths.

3.2.2 Experimental Validation of D_3-Based Crack Propagation Monitoring

In this section, the selected D_3-based formulation is applied to the tested laminate configurations to evaluate the ability of the proposed framework to monitor crack-sensitive localization and crack propagation. For each specimen, D_3-based damage-sensitive localization maps are presented at selected normalized analysis steps and compared with the experimentally observed crack path. These steps represent successive stages within the reliable DIC interval selected for each specimen and are used to visualize the temporal development of the localization pattern.

The purpose of this comparison is not to reproduce the crack path as a sharp discontinuity, but to examine whether the high-index regions predicted by the proposed framework develop in locations that are consistent with the experimentally observed crack-sensitive zones. Therefore, the following discussion focuses on the spatial evolution, orientation, and connectivity of the localized D_3 regions for different laminate stacking sequences and initial crack orientations.

In addition to the visual comparison of the D_3 maps, a quantitative pre-failure localization assessment is carried out to evaluate the spatial and directional consistency of the high-D_3 regions with the experimentally observed crack-propagation behavior. This assessment is based on two indicators: the minimum distance between the initial crack tip and the nearest high-D_3 element, and the orientation difference between the PCA-based dominant direction of the high-D_3 band and the observed crack-propagation direction. The high-D_3 regions are defined using a threshold ratio of $\tau = 0.6$. Before applying this value to the full specimen set, a threshold assessment is performed for $\tau = 0.5$, 0.6, and 0.7. The results show that the crack-tip proximity distance remains unchanged and that the orientation difference stays within a low range for the tested thresholds. Therefore, $\tau = 0.6$ is adopted for the quantitative evaluation of the remaining specimens.

The step numbers used in the following figures are reported as normalized analysis steps. For each specimen, a reliable DIC frame interval is selected from the original ARAMIS/GOM image sequence by excluding frames affected by advanced crack opening, final rupture, or loss of optical correlation. The selected frames are then processed through the SEA workflow and renumbered for consistent presentation. Therefore, step 100 represents the final reliable analysis stage of the selected interval for each specimen, rather than the same original DIC frame or the same physical loading state for all specimens.

3.2.2.1 Damage Monitoring of 0/90/0 Laminate with 90° Initial Crack

Figure 3.11 presents the D_3-based damage-sensitive localization maps for the 0/90/0 laminate with a 90° initial crack orientation at four representative steps: 70, 80, 90, and 100. The experimentally observed crack path is also provided for comparison. At step 70, the localization pattern is mainly concentrated around two separate regions near the initial crack tips. As loading progresses to steps 80 and 90, these high-index regions become more pronounced and begin to extend laterally. At step 100,

the localization pattern develops into a clearer horizontally elongated form, which is consistent with the experimentally observed crack path. This evolution indicates that, for the 0/90/0 laminate with a 90° initial crack orientation, the proposed D_3 field captures the progressive development of crack-sensitive regions from initially compact zones toward a more extended horizontal damage-localization pattern.

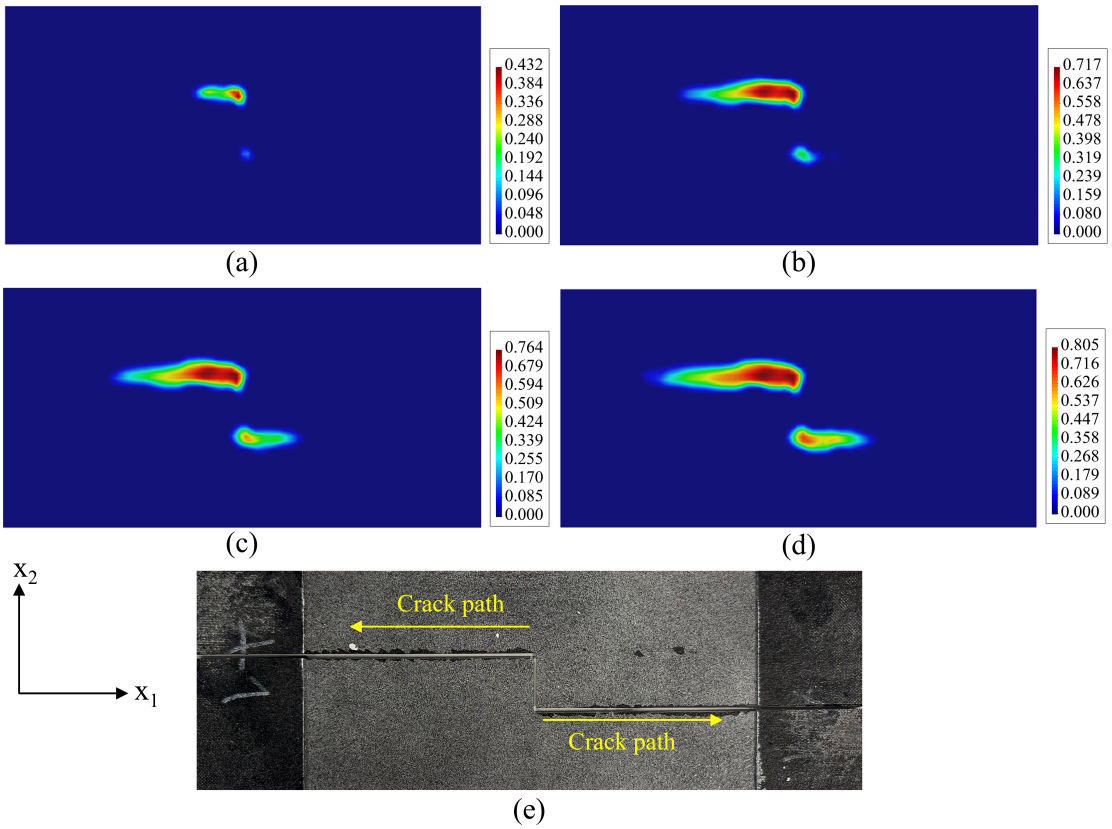

Figure 3.11 D_3-based damage localization maps for the 0/90/0 laminate with a 90° initial crack orientation at different steps: (a) step 70, (b) step 80, (c) step 90, (d) step 100, and (e) experimentally observed crack path.

To quantitatively support the visual interpretation of Figure 3.11, the threshold-based localization metrics described in Section 3.1.9 have been calculated for the 0/90/0 laminate with a 90° initial crack orientation. In this specimen, Tip 1 refers to the upper crack tip and Tip 2 refers to the lower crack tip; the same tip-numbering convention has been used for the remaining specimens. The positive x_1-direction was taken as 0°, the positive x_2-direction as 90°, the negative x_1-direction as 180°, and the negative x_2-direction as 270°. For each specimen, the experimentally observed crack-propagation direction was assigned according to the dominant direction of the corresponding crack branch in this coordinate system.

Table 3.1 presents the threshold assessment performed for $\tau = 0.5$, 0.6, and 0.7. The table includes the number of high-D_3 elements, the minimum distance from

the crack tip, d_{tip}, the PCA-based dominant orientation of the high-D_3 band, θ_{D_3}, the experimentally observed crack-propagation direction, θ_{crack}, the orientation difference, $\Delta\theta$, and the percentage orientation difference. The rows corresponding to $\tau = 0.6$ are highlighted because this threshold has been selected for the full quantitative evaluation.

Table 3.1 Threshold Assessment of the Quantitative Localization Metrics for the 0/90/0 Laminate with a 90° Initial Crack Orientation

Tip	N_{D_3}	d_{tip} (mm)	θ_{D_3} (°)	θ_{crack} (°)	$\Delta\theta$ (°)	% $\Delta\theta$	τ
1	97	1.414	179.068	180	0.932	0.52	0.5
2	33	1.414	2.303	0	2.303	1.28	0.5
1	73	1.414	179.320	180	0.680	0.38	0.6
2	19	1.414	4.776	0	4.776	2.65	0.6
1	58	1.414	179.082	180	0.918	0.51	0.7
2	10	1.414	1.894	0	1.894	1.05	0.7

The threshold comparison shows that the minimum distance from the crack tip remains constant at 1.414 mm for both tips for all threshold values. This indicates that the closest high-D_3 elements are consistently located near the initial crack-tip zones, independent of the selected threshold level. As expected, the number of high-D_3 elements decreases as the threshold increases, since higher threshold values retain only the most strongly activated localization regions. For Tip 1, the number of high-D_3 elements decreases from 97 at $\tau = 0.5$ to 73 at $\tau = 0.6$ and 58 at $\tau = 0.7$. For Tip 2, it decreases from 33 to 19 and then to 10. Although $\tau = 0.5$ retains a larger number of elements, it also includes a broader region. In contrast, $\tau = 0.7$ produces a more restrictive region, but the number of retained elements becomes relatively low, especially for Tip 2. The intermediate value $\tau = 0.6$ therefore provides a balanced selection: it keeps the high-D_3 region sufficiently focused while preserving enough elements for PCA-based orientation estimation. In addition, the percentage orientation difference remains below 3% for both tips at $\tau = 0.6$. Based on these observations, $\tau = 0.6$ was selected for the quantitative evaluation of all specimens.

For the selected threshold value $\tau = 0.6$, the high-D_3 region associated with Tip 1 contains 73 elements and is located 1.414 mm from the upper crack tip. The PCA-based dominant orientation is 179.320°, which is almost parallel to the experimentally observed propagation direction of 180°. The corresponding orientation difference is only 0.680°, with a percentage difference of 0.38%. For Tip 2, 19 high-D_3 elements are retained, again with a minimum crack-tip distance of 1.414 mm. The

dominant orientation is 4.776°, which is close to the experimentally observed propagation direction of 0°, giving an orientation difference of 4.776° and a percentage difference of 2.65%.

It should be noted that this repeated d_{tip} value is primarily associated with the spatial discretization of the post-processing mesh. In the present assessment, d_{tip} is evaluated as the minimum distance between the initial crack-tip coordinate and the centroid of the nearest thresholded high-D_3 element. Therefore, attainable distance values are inherently governed by the mesh resolution and the spacing of element centroids. For this reason, d_{tip} should not be interpreted as a continuous physical measurement of the exact crack-tip-to-localization distance. Instead, it represents a mesh-resolution-limited proximity metric that indicates whether the high-D_3 localization field is activated within the immediate vicinity of the crack-tip zone.

These results are consistent with the D_3 map shown in Figure 3.11. The high-D_3 regions are formed very close to the two initial crack tips and develop mainly along the horizontal direction, matching the observed crack-propagation pattern. Therefore, for the 0/90/0 laminate with a 90° initial crack orientation, the quantitative metrics confirm that the D_3 field captures both the crack-tip proximity and the dominant propagation direction before final fracture.

3.2.2.2 Damage Monitoring of 0/90/0 Laminate with 45° Initial Crack

Figure 3.12 shows the D_3-based localization maps for the 0/90/0 laminate with a 45° initial crack orientation at steps 70, 80, 90, and 100, together with the experimentally observed crack path. In this configuration, two distinct high-index regions are already visible at the earlier stages. These regions remain relatively compact and separated up to step 90, indicating that the localization pattern is established early but does not immediately spread over a large area. At step 100, both regions extend more clearly in the horizontal direction and form a two localization pattern. This final map is compatible with the experimentally observed crack path, which also develops along two approximately parallel crack. Therefore, for the specimen, the D_3 response suggests a later-stage extension of two previously established crack-sensitive zones rather than a sudden redistribution of the localization field.

For the 0/90/0 laminate with a 45° initial crack orientation, the quantitative localization metrics are summarized in Table 3.2. In this specimen, the experimentally

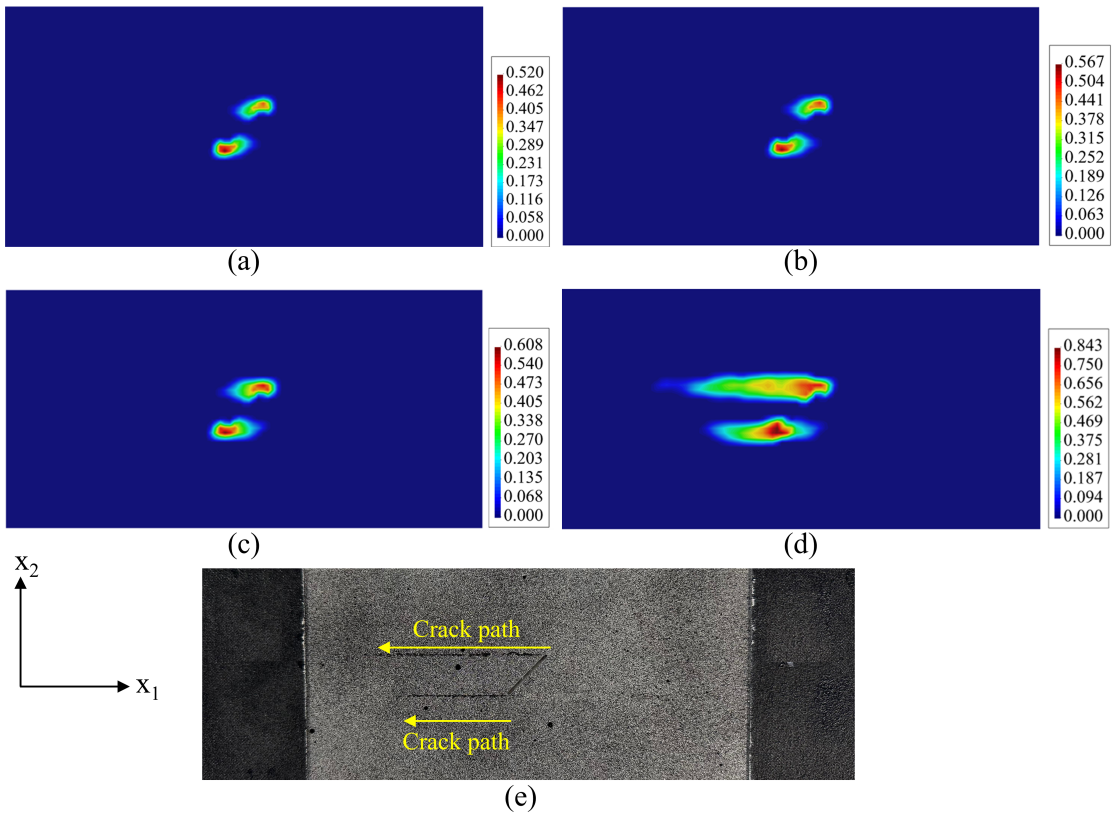

Figure 3.12 D_3-based damage localization maps for the 0/90/0 laminate with a 45° initial crack orientation at different steps: (a) step 70, (b) step 80, (c) step 90, (d) step 100, and (e) experimentally observed crack path.

observed crack-propagation direction was taken as 180° for both tips according to the dominant direction of the crack branches in the specimen coordinate system.

Using the selected threshold value $\tau = 0.6$, 31 high-D_3 elements are assigned to Tip 1, and 41 high-D_3 elements are assigned to Tip 2. For both tips, the minimum distance from the crack tip was 0.728 mm. This indicates that the high-D_3 regions are formed very close to the initial crack-tip zones before final fracture. Therefore, the D_3 field did not activate in arbitrary regions of the specimen but concentrated around the mechanically critical crack-tip locations.

Table 3.2 Quantitative Pre-Failure Localization Metrics for the 0/90/0 Laminate with a 45° Initial Crack Orientation ($\tau = 0.6$)

Tip	N_{D_3}	d_{tip} (mm)	θ_{D_3} (°)	θ_{crack} (°)	$\Delta\theta$ (°)	% $\Delta\theta$
1	31	0.728	178.577	180	1.422	0.79
2	41	0.728	183.471	180	3.471	1.93

The PCA-based dominant orientations were 178.577° for Tip 1 and 183.471° for Tip 2. These values are close to the experimentally observed crack-propagation direction of 180°. The corresponding orientation differences were 1.422° and 3.471°, giving percentage differences of 0.79% and 1.93%, respectively. These low differences show that the high-D_3 localization bands are directionally consistent with the subsequent crack-propagation tendency. Although the initial crack was inclined at 45°, the D_3 field captured the later horizontal propagation tendency observed experimentally. Therefore, the quantitative results support the visual interpretation of Figure 3.12 by confirming both crack-tip proximity and orientation agreement.

3.2.2.3 Damage Monitoring of 90/0/90 Laminate with 45° Initial Crack

Figure 3.13 presents the D_3-based localization maps for the 90/0/90 laminate with a 45° initial crack orientation at Steps 70, 80, 90, and 100, together with the experimentally observed crack path. Up to step 90, the localization field remains mainly concentrated in two separated high-index regions, with only moderate changes in their spatial extent. At step 100, however, a stronger and more extended central localization region appears. This final-stage response should be interpreted with caution. As observed in the Figure 3.13(e), the surface paint layer was locally disturbed and partially detached near the final stage, which reduced the local DIC correlation quality. This effect should be considered when interpreting the final D_3 map, because local decorrelation or pattern degradation may artificially increase the apparent localization response in the affected region. Therefore, the enlarged high-D_3 zone observed at the final step should not be interpreted only as physical damage growth; it may also include a contribution from reduced optical tracking quality. Nevertheless, outside the locally disturbed region, the overall map of the localization pattern remains consistent with the experimentally observed crack path.

For this specimen, the quantitative results shown in Table 3.3 reveal a more extended localization response compared with the previous 0/90/0 cases. Using $\tau = 0.6$, 486 high-D_3 elements were associated with Tip 1 and 443 elements with Tip 2, indicating that the high-D_3 region was not limited to a narrow crack-tip zone but developed as a broader localization band. Nevertheless, the closest high-D_3 elements were still located very near the crack tips, with $d_{\text{tip}} = 0.728$ mm for both tips.

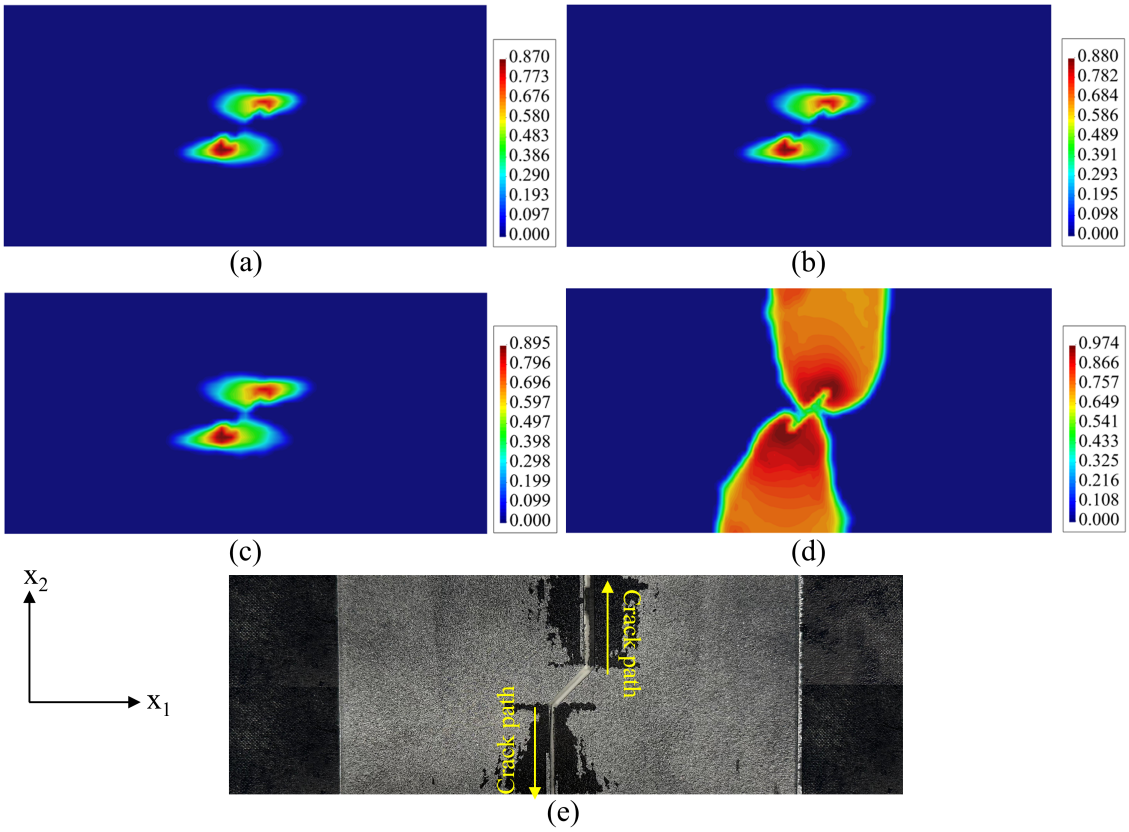

Figure 3.13 D_3-based damage localization maps for the 90/0/90 laminate with a 45° initial crack orientation at different steps: (a) step 70, (b) step 80, (c) step 90, (d) step 100, and (e) experimentally observed crack path.

Table 3.3 Quantitative Pre-Failure Localization Metrics for the 90/0/90 Laminate with a 45° Initial Crack Orientation ($\tau = 0.6$)

Tip	N_{D_3}	d_{tip} (mm)	θ_{D_3} (°)	θ_{crack} (°)	$\Delta\theta$ (°)	% $\Delta\theta$
1	486	0.728	91.975	90	1.975	1.10
2	443	0.728	271.573	270	1.573	0.87

The PCA-based orientations also reflect the dominant vertical character of the localization pattern. The estimated directions were 91.975° for Tip 1 and 271.573° for Tip 2, which are close to the experimentally observed propagation directions of 90° and 270°, respectively. The resulting angular differences were 1.975° and 1.573°, corresponding to percentage differences of 1.10% and 0.87%. Therefore, unlike the 0/90/0 specimens where the D_3 response mainly followed a horizontal propagation tendency, this case shows that the quantitative metric also captures a vertically oriented localization pattern with low directional error.

3.2.2.4 Damage Monitoring of 0/0/0 Laminate with 90° Initial Crack

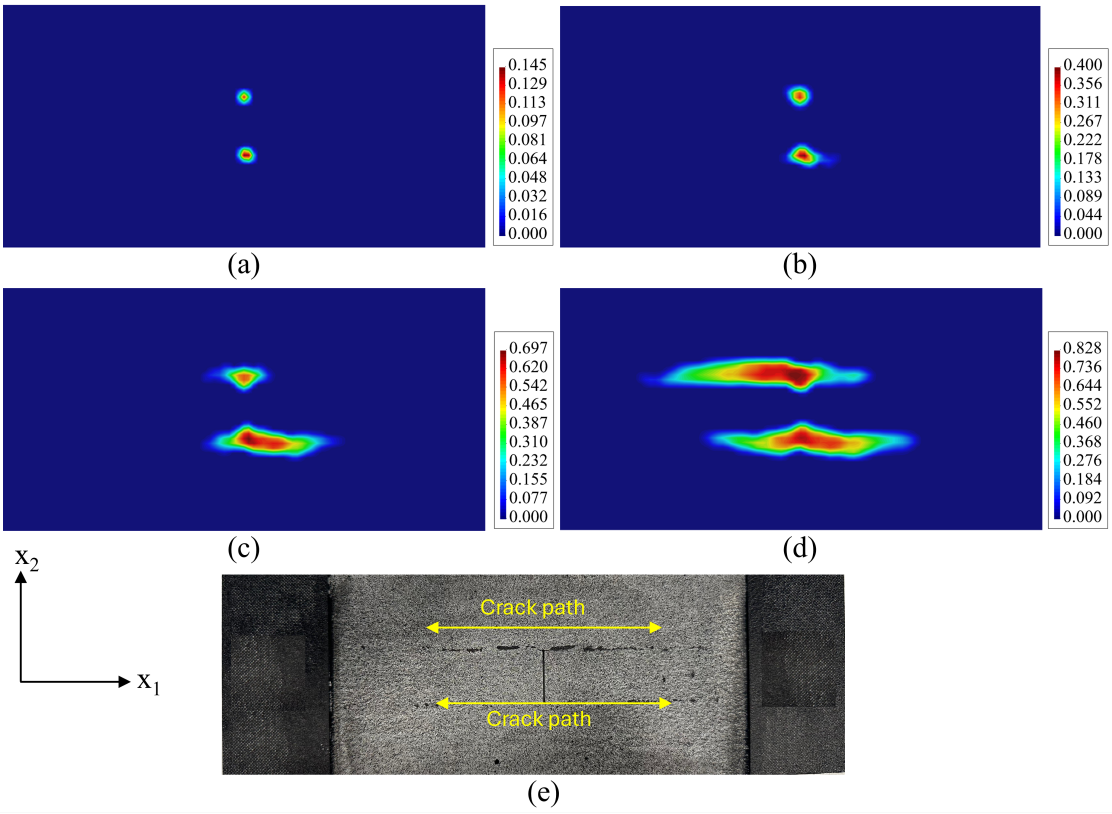

Figure 3.14 D_3-based damage localization maps for the 0/0/0 laminate with a 90° initial crack orientation at different steps: (a) step 70, (b) step 80, (c) step 90, (d) step 100, and (e) experimentally observed crack path.

Figure 3.14 shows the D_3-based localization maps for the 0/0/0 laminate with a 90° initial crack orientation at steps 70, 80, 90, and 100, together with the experimentally observed crack path. At step 70, the response is confined to two small and clearly separated high-index regions near the crack-tip zones. By step 80, the lower region starts to elongate laterally, while the upper region remains more compact. At step 90, both regions become broader and more intense, indicating a more distinct development of the crack-sensitive localization pattern. This trend becomes more pronounced at step 100, where both upper and lower localization zones extend predominantly in the horizontal direction. The final D_3 pattern is consistent with the experimentally observed crack path, which also shows horizontally developed crack branches. Overall, this specimen exhibits a progressive transition from compact crack-tip localization to an extended horizontal damage-sensitive pattern.

For the 0/0/0 laminate with a 90° initial crack orientation, the quantitative localization metrics are summarized in Table 3.4. The results support the progressive

horizontal localization pattern observed in the D_3 maps. Using the selected threshold value $\tau = 0.6$, 83 high-D_3 elements were associated with Tip 1 and 73 elements with Tip 2. For both tips, the minimum distance from the crack tip was 1.4142 mm, indicating that the high-D_3 regions were initiated very close to the initial crack-tip zones.

Table 3.4 Quantitative Pre-Failure Localization Metrics for the 0/0/0 Laminate with a 90° Initial Crack Orientation ($\tau = 0.6$)

Tip	N_{D_3}	d_{tip} (mm)	θ_{D_3} (°)	θ_{crack} (°)	$\Delta\theta$ (°)	% $\Delta\theta$
1	83	1.4142	3.518	0	3.518	1.95
2	73	1.4142	2.022	0	2.022	1.12

The PCA-based dominant orientations were 3.518° for Tip 1 and 2.022° for Tip 2. These values are close to the experimentally observed crack-propagation direction of 0°, which corresponds to the positive x_1-direction. The orientation differences were 3.518° and 2.022°, with percentage differences of 1.95% and 1.12%, respectively. These low angular differences indicate that the high-D_3 bands are well aligned with the experimentally observed horizontal crack-propagation tendency.

This result is mechanically consistent with the 0/0/0 laminate configuration. Since the laminate is dominated by 0° plies aligned with the loading direction, the crack-tip deformation tends to redistribute along the longitudinal direction. Therefore, the D_3 field captures both the near-tip activation and the horizontal propagation tendency of the damage-sensitive region before final fracture.

3.2.2.5 Damage Monitoring of 0/0/0 Laminate with 45° Initial Crack

Figure 3.15 presents the D_3-based localization maps for the 0/0/0 laminate with a 45° initial crack at steps 40, 60, 80, and 100, together with the experimentally observed crack path. In this configuration, two localized high-index regions are visible at the earlier loading stage, indicating an early formation of crack-sensitive zones. From step 40 to step 60, the general pattern remains compact, although the intensity of the two regions increases. A more substantial spatial development is observed at step 80, where both the upper and lower high-index regions broaden, particularly in the horizontal direction. By step 100, this lateral expansion becomes

more evident, and the two regions evolve into elongated bands. This final localization pattern is consistent with the experimentally observed crack path, which also extends predominantly along two horizontal branches. Thus, the 0/0/0 laminate with a 45° initial crack orientation shows early localization followed by pronounced later-stage lateral growth.

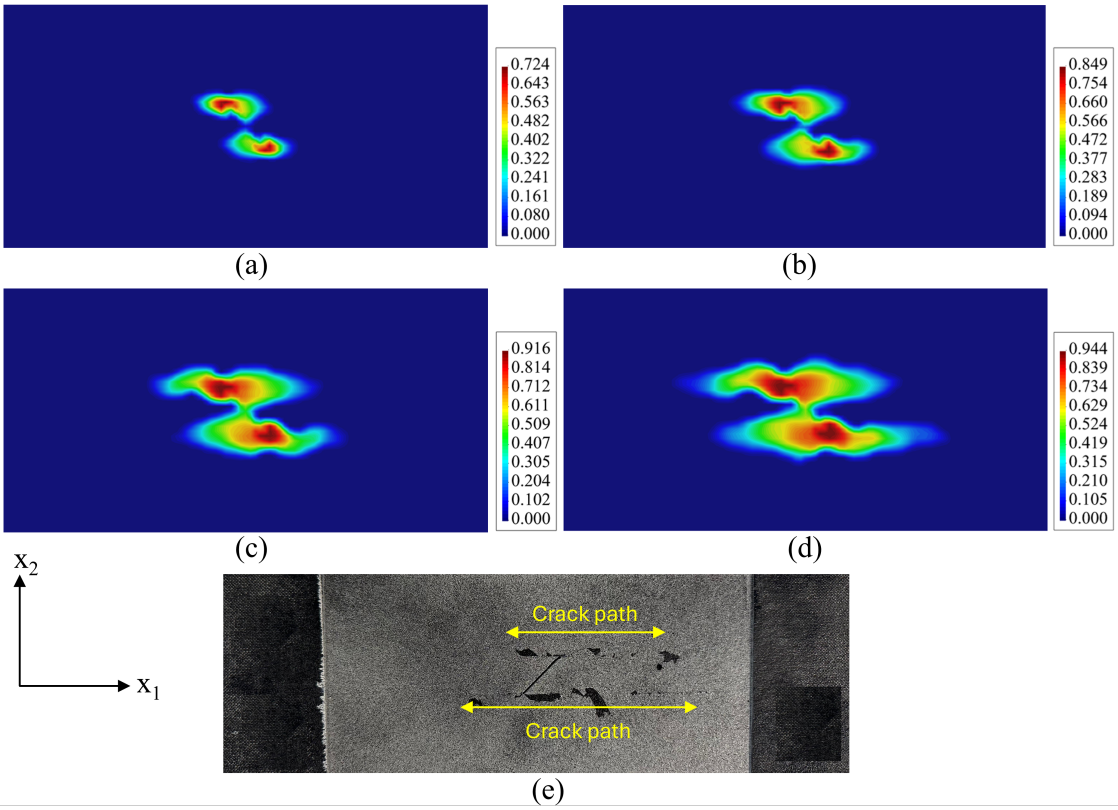

Figure 3.15 D_3-based damage localization maps for the 0/0/0 laminate with a 45° initial crack orientation at different steps: (a) step 40, (b) step 60, (c) step 80, (d) step 100, and (e) experimentally observed crack path.

For the 0/0/0 laminate with a 45° initial crack orientation, Table 3.5 shows that the D_3 response follows the same dominant horizontal tendency observed in the final crack pattern. Although the initial crack is inclined, the high-D_3 regions develop mainly along the x_1-direction, indicating that the localization behavior is governed more by the longitudinal load-carrying response of the 0° plies than by the initial crack angle alone.

Table 3.5 Quantitative Pre-Failure Localization Metrics for the 0/0/0 Laminate with a 45° Initial Crack Orientation ($\tau = 0.6$)

Tip	N_{D_3}	d_{tip} (mm)	θ_{D_3} (°)	θ_{crack} (°)	$\Delta\theta$ (°)	% $\Delta\theta$
1	109	1.4142	0.461	0	0.461	0.26
2	98	1.4142	3.322	0	3.322	1.85

Using $\tau = 0.6$, 109 high-D_3 elements were identified around Tip 1 and 98 around Tip 2. The minimum distance from the crack tip was 1.4142 mm for both tips, showing that the activated D_3 regions remain close to the crack-tip zones. The PCA-based dominant orientations were 0.461° and 3.322°, respectively, both of which are very close to the experimentally observed propagation direction of 0°.

The corresponding orientation differences were 0.461° for Tip 1 and 3.322° for Tip 2, with percentage differences of 0.26% and 1.85%. These low values indicate that the high-D_3 bands are not only located near the initial crack tips but also aligned with the observed horizontal crack-propagation tendency. Therefore, this specimen further supports the interpretation that the proposed D_3 index can identify the dominant pre-failure localization direction even when the initial crack is oblique.

3.2.2.6 Damage Monitoring of 90/90/90 Laminate with 45° Initial Crack

For the 90/90/90 laminate with a 45° initial crack orientation, the localization behavior differs from the previously discussed specimens. Figure 3.16 presents the D_3-based maps at selected steps together with the experimentally observed crack path. In the earlier stages, no clearly developed high-index localization zone observed. Instead, a distinct and highly concentrated D_3 response appears abruptly at the final stage. At step 100, the localization pattern consists of two vertically aligned high-index regions separated by the initial crack path. This behavior is consistent with experimental observation, where the crack path is predominantly oriented in the vertical direction and becomes clearly visible only close to sudden failure. Therefore, in this configuration, the damage-sensitive localization response is characterized less by gradual spatial expansion and more by delayed localization followed by rapid fracture development near the final loading stage.

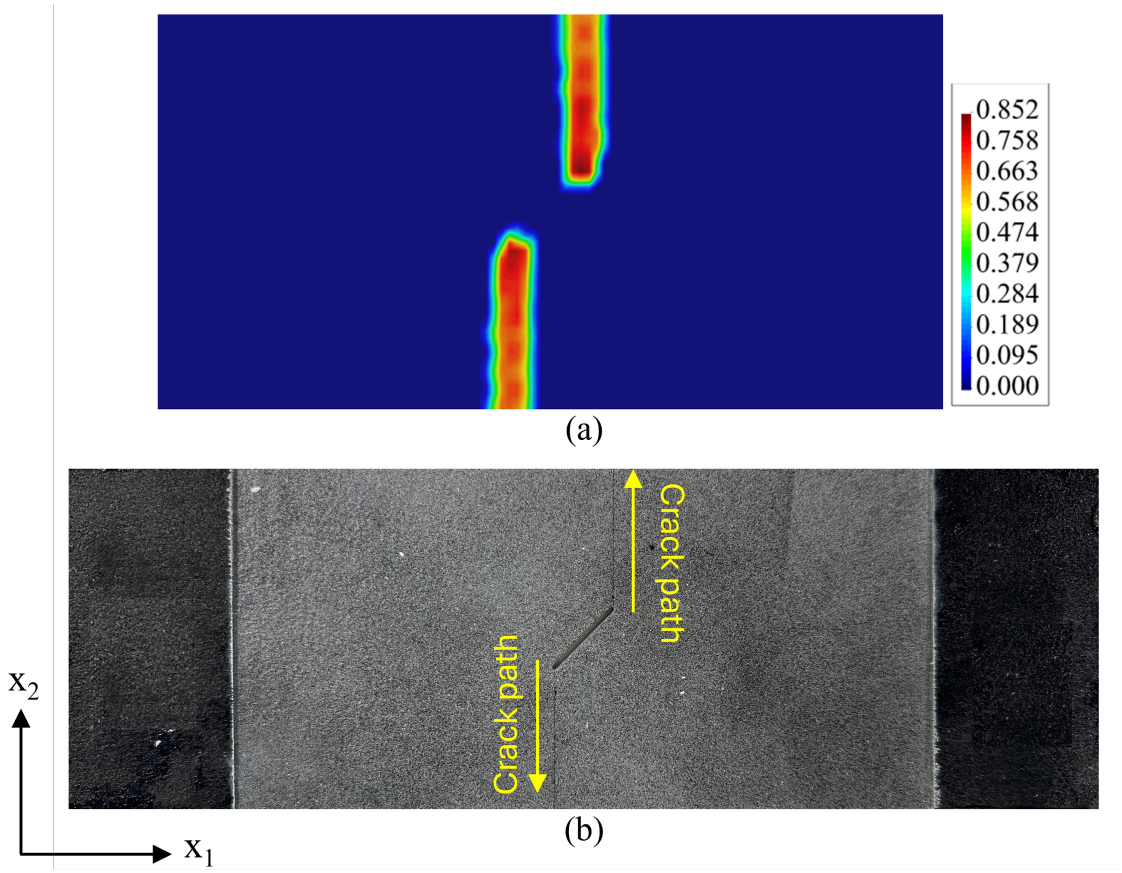

Figure 3.16 D_3-based damage localization maps for the 90/90/90 laminate with a 45° initial crack orientation: (a) step 100 and (b) experimentally observed crack path.

Table 3.6 Quantitative Pre-Failure Localization Metrics for the 90/90/90 Laminate with a 45° Initial Crack Orientation ($\tau = 0.6$)

Tip	N_{D_3}	d_{tip} (mm)	θ_{D_3} (°)	θ_{crack} (°)	$\Delta\theta$ (°)	% $\Delta\theta$
1	91	0.728	89.653	90	0.347	0.19
2	91	0.728	88.253	90	1.745	0.97

For the 90/90/90 laminate with a 45° initial crack orientation, the results in Table 3.6 highlight the vertical character of the delayed localization response. Using $\tau = 0.6$, 91 high-D_3 elements were identified around both Tip 1 and Tip 2. The minimum distance from the crack tip was 0.728 mm for both tips, showing that the localization response developed very close to the initial crack-tip zones. This supports the interpretation that, although the visible localization appeared suddenly near the final reliable stage, the high-D_3 regions were still spatially connected to the mechanically critical crack-tip areas.

The PCA-based dominant orientations reported in Table 3.6 were 89.653° for Tip 1 and 88.253° for Tip 2. These values are very close to the experimentally observed crack-propagation direction of 90°. The corresponding orientation differences were 0.347° and 1.745°, with percentage differences of 0.19% and 0.97%, respectively. These low values indicate strong directional agreement between the high-D_3 localization bands and the experimentally observed vertical crack-propagation tendency. Therefore, Table 3.6 confirms that the D_3 index is not limited to horizontally propagating damage patterns. It also captures the delayed and vertically oriented localization behavior observed in the 90/90/90 laminate before final fracture.

3.2.2.7 Damage Monitoring of 90/90/90 Laminate with 90° Initial Crack

Figure 3.17 presents the D_3-based localization maps for the 90/90/90 laminate with a 90° initial crack orientation at selected Steps, together with the experimentally observed crack path. Like the previous 90/90/90 configuration, no clearly developed localization pattern is observed during the earlier stages. The dominant D_3 response becomes visible only near final failure. At step 100, two vertically aligned high-index regions appear on either side of the initial crack, forming a narrow localization pattern that is consistent with the experimentally observed crack path. This result indicates that, for the 90/90/90 laminate with a 90° initial crack orientation, the crack-sensitive localization pattern does not evolve gradually over multiple loading stages. Instead, it emerges suddenly near final failure, suggesting delayed localization followed by rapid fracture development.

For the 90/90/90 laminate with a 90° initial crack orientation, Table 3.7 further confirms the delayed vertical localization behavior observed in the D_3 maps. Using $\tau = 0.6$, 76 high-D_3 elements were identified around Tip 1 and 85 around Tip 2. The minimum crack-tip distance was 1.4142 mm for both tips, showing that the activated regions remained close to the initial crack tips. The PCA-based dominant orientations were 89.912° and 89.094°, respectively, which are almost coincident with the experimentally observed crack-propagation direction of 90°.

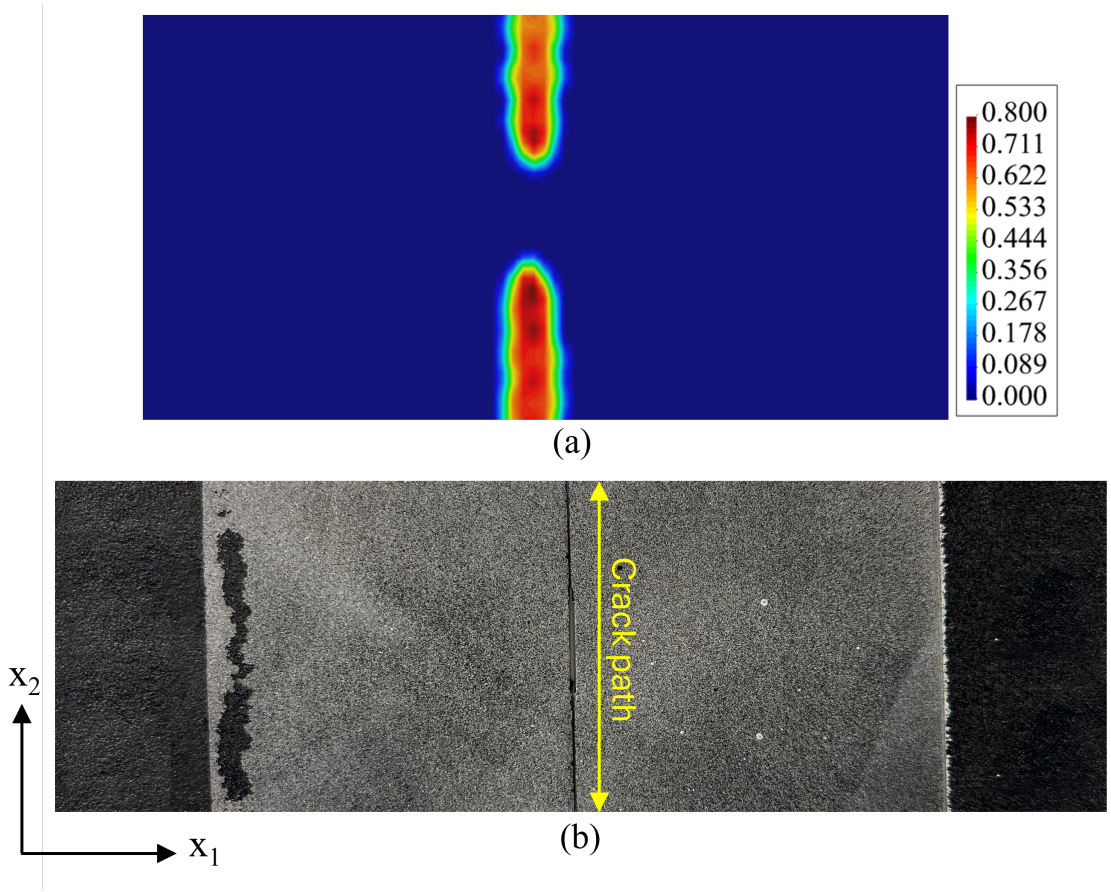

Figure 3.17 D_3-based damage localization maps for the 90/90/90 laminate with a 90° initial crack orientation: (a) step 100 and (b) experimentally observed crack path.

Table 3.7 Quantitative Pre-Failure Localization Metrics for the 90/90/90 Laminate with a 90° Initial Crack Orientation ($\tau = 0.6$)

Tip	N_{D_3}	d_{tip} (mm)	θ_{D_3} (°)	θ_{crack} (°)	$\Delta\theta$ (°)	% $\Delta\theta$
1	76	1.4142	89.912	90	0.088	0.05
2	85	1.4142	89.094	90	0.906	0.50

The corresponding orientation differences were only 0.088° for Tip 1 and 0.906° for Tip 2, with percentage differences of 0.05% and 0.50%. These values represent the lowest directional errors among the evaluated specimens. Therefore, Table 3.7 supports the interpretation that the 90/90/90 laminate with a 90° initial crack orientation develops a sharply defined vertical localization pattern near final failure, and that this behavior is quantitatively captured by the D_3-based metric.

3.2.3 Cross-Specimen Interpretation

Across the tested configurations, the D_3 maps reveal two main localization behaviors: progressive horizontal localization and delayed vertical localization. These behaviors are closely related to the laminate architecture, the initial crack orientation, and the direction of the dominant load-carrying plies. In the 0°-dominated laminates, namely the 0/90/0 and 0/0/0 configurations, the localization generally develops from compact crack-tip regions into horizontally extended bands. In contrast, the 90/90/90 laminates show a delayed response, where the dominant D_3 localization becomes visible only near the final reliable loading stage and follows a predominantly vertical direction.

For the 0/90/0 laminate with a 90° initial crack orientation, the D_3 field shows a gradual development of two crack-tip localization regions. At the earlier stages, the high-D_3 zones remain relatively compact and separated. As loading progresses, these regions become more pronounced and extend laterally, forming a horizontally oriented localization pattern. This behavior is consistent with the experimentally observed crack propagation and indicates that the D_3 field captures the progressive transition from local crack-tip deformation to an extended damage-sensitive band.

The 0/90/0 laminate with a 45° initial crack orientation also shows progressive localization, but the response is less symmetric because of the oblique crack geometry. The high-D_3 regions appear around both crack tips and evolve into two branch-like horizontal localization zones at later stages. Although the initial crack is inclined, the final localization tendency is mainly horizontal. This indicates that the crack angle affects the early strain-gradient distribution, while the laminate architecture and loading direction strongly influence the later propagation tendency.

The 0/0/0 laminates exhibit the clearest progressive horizontal localization behavior. Since all plies are aligned with the loading direction, the longitudinal load-transfer capacity is dominant. As a result, the deformation around the crack tips redistributes mainly along the x_1-direction, and the D_3 regions gradually develop into elongated horizontal bands. This behavior is observed for both 90° and 45° initial crack orientations. Therefore, in the 0/0/0 specimens, the D_3 field reflects the strong influence of the 0° plies on the direction of damage-sensitive localization.

The 90/0/90 laminate with a 45° initial crack orientation shows an intermediate response. The central 0° ply contributes to longitudinal load transfer, while the outer 90° plies promote a more matrix-dominated deformation pattern. This mixed archi-

tecture leads to separated high-D_3 regions during the earlier stages and a broader central localization region near the final stage. However, this final-stage response should be interpreted carefully because local paint detachment and DIC correlation degradation were observed near fracture. This indicates that the D_3 maps should be interpreted together with the quality of the underlying DIC measurement, especially near final fracture where speckle degradation, paint detachment, or local decorrelation may affect the apparent localization field.

In contrast to the 0° dominated laminates, the 90/90/90 specimens show delayed and more abrupt localization. Since the plies are oriented transverse to the loading direction, the axial response is more matrix-dominated and does not promote gradual horizontal redistribution in the same way as the 0°-dominated laminates. Therefore, clearly developed D_3 bands are not observed during the earlier loading stages. Instead, the dominant localization appears close to the final reliable stage and develops mainly in the vertical direction. This behavior is observed for both 45° and 90° initial crack orientations, showing that the 90/90/90 laminate produces a distinctly different localization mode compared with the 0/90/0 and 0/0/0 laminates.

The quantitative metrics support these visual and mechanical interpretations without replacing them. The low crack-tip distances indicate that the high-D_3 regions consistently develop near the mechanically critical crack-tip zones, while the small PCA-based orientation differences show that the dominant D_3 bands are aligned with the experimentally observed crack-propagation directions. Thus, the quantitative results confirm the trends observed in the D_3 maps: horizontal progressive localization in 0°-dominated laminates, broader mixed localization in the 90/0/90 laminate, and delayed vertical localization in 90°-dominated laminates.

Overall, the D_3 response is governed by the combined effect of ply orientation, initial crack orientation, and the resulting strain-gradient distribution. The initial crack defines the local deformation disturbance, but the laminate architecture controls how this disturbance evolves during loading. Therefore, the proposed D_3 index does not only indicate the presence of crack-tip localization; it also reflects the laminate-dependent direction and evolution of damage-sensitive regions before final fracture.

4. INTEGRATED MULTI-INSTRUMENT ANALYSIS FOR DAMAGE CHARACTERIZATION AND CRACK PROPAGATION MONITORING IN PRE-CRACKED COMPOSITE LAMINATES

4.1 Multi-Instrument Data Processing and Interpretation Framework

4.1.1 General Strategy and Time Alignment

The multi-instrument interpretation is based on the combined evaluation of DIC, AE, strain gauge, and mechanical test data. The mechanical test system provides the global load, displacement, and test time, which are used as the common reference for comparing the different measurement outputs.

The DIC data is used to evaluate the spatial development of strain localization around the initial crack region. In this study, the equivalent strain field obtained from the DIC evaluation is used as a scalar visualization measure for crack-sensitive localization. The AE data is used to identify time intervals in which acoustic activity increases during tensile loading. For the strain-gauged configurations, the measured local strain response is used as additional mechanical evidence.

The DIC and AE data are correlated on a common time basis. After the AE time-history indicators are evaluated, the main AE activity intervals are identified. The DIC frames closest to these intervals are then selected and examined to determine whether strain localization or strain redistribution develops around the crack region. For specimens with strain gauges, the strain response is evaluated over the same

intervals.

4.1.2 AE Time-History Indicators

The AE software provides the main hit-based parameters, including acquisition time, amplitude, counts, duration, energy, average frequency, peak frequency, and RA value. These parameters are used as the input for AE post-processing. Before further analysis, incomplete or non-physical records are removed. The retained AE hits satisfy positive time, positive counts, positive duration, positive frequency values, positive RA value, and amplitude above the selected acquisition threshold. Although the AE software provides the energy of each hit, the cumulative AE energy is calculated during post-processing to evaluate the progressive accumulation of acoustic activity. At a given time t, cumulative energy is obtained by summing the energy of all AE hits recorded up to that time:

$$E_c(t) = \sum_{t_i \leq t} E_i t_i \tag{4.1}$$

where E_i is the energy of the i-th AE hit and t_i is its acquisition time. A gradual increase in E_c indicates continuous acoustic activity, whereas a sudden increase or a clear slope change indicates a more active acoustic interval. To identify the time intervals where AE activity becomes more intense, the AE record is divided into fixed time bins. The set of AE hits recorded in the j-th time bin is denoted by the time interval Δt. The hit rate is calculated as:

$$H_j = \frac{n_j}{\Delta t} \tag{4.2}$$

where n_j is the number of AE hits in the j-th time bin. This quantity represents the density of detected AE events per unit time. The energy rate is calculated as:

$$R_{E,j} = \frac{\sum_{i \in A_j} E_i}{\Delta t} \tag{4.3}$$

where $R_{E,j}$ is the acoustic energy released per unit time in the j-th bin. This quantity is used to identify intervals dominated by more energetic AE events. The RA value is also evaluated within the same time bins to monitor changes in the

acoustic event character. For each time bin, the median RA value and the 90th percentile RA value are calculated as:

$$RA_{50,j} = median(RA_i \mid i \in A_j) \tag{4.4}$$

$$RA_{90,j} = P_{90}(RA_i \mid i \in A_j) \tag{4.5}$$

where $RA_{50,j}$ represents the central tendency of the RA values and $RA_{90,j}$ highlights the occurrence of higher-RA events. These RA-based quantities are used as supporting acoustic descriptors. They are not interpreted as direct damage-mode fractions.

4.1.3 Global AE Population Analysis Using K-Means Clustering

In addition to the AE time-history indicators, a global unsupervised clustering analysis is performed to identify characteristic acoustic event populations across all laminate configurations. All retained AE hits from the seven specimens are combined into a single dataset before clustering. Therefore, the same cluster definition is used for every specimen.

Each AE hit is represented by a multi-parameter feature vector composed of RA value, average frequency, peak frequency, amplitude, energy, counts, and duration. Logarithmic transformation is applied to the positive and strongly skewed AE parameters to reduce the influence of extreme values. The feature vector is written as:

$$x_i = \begin{bmatrix} \log(1+RA_i) \\ \log(1+AF_i) \\ \log(1+PF_i) \\ A_i \\ \log(1+E_i) \\ \log(1+N_i) \\ \log(1+D_i) \end{bmatrix} \tag{4.6}$$

where RA_i, AF_i, PF_i, A_i, E_i, N_i, and D_i are the RA value, average frequency, peak

frequency, amplitude, energy, counts, and duration of the i-th AE hit, respectively. Before clustering, the features are robustly standardized using the median and median absolute deviation. For the k-th feature, the standardized value is calculated as:

$$z_{ik} = \frac{x_{ik} - x_k}{1.4826 MAD_k} \tag{4.7}$$

where x_{ik} is the k-th feature of the i-th AE hit, x_k is the median of the k-th feature, and MAD_k is the median absolute deviation of the same feature. K-means clustering is then applied to the standardized feature matrix. The number of clusters is selected by comparing $k = 2$, 3, and 4 using the mean silhouette value. The cluster number with the highest mean silhouette value is selected.

After clustering, the centroid values are transformed back to the original AE parameter space and used to describe the acoustic character of each cluster. The clusters are interpreted as AE event populations rather than direct damage modes. For each specimen, the cluster contributions are evaluated using count-based and energy-based distributions. The energy-based distribution is emphasized because it shows which AE population contributes more strongly to the total acoustic energy released during damage evolution.

4.1.4 Stage-Wise DIC-AE-SG Correlation

The crack propagation process is evaluated by correlating the DIC, AE, and strain gauge responses at selected loading stages. The aim is not to assign a unique damage mechanism to each measurement output. Instead, the aim is to identify the time intervals in which crack-related activity is supported by more than one experimental measurement.

The selected stages are determined from the combined evaluation of the global mechanical response and the AE time-history results. Sudden increases in cumulative AE energy, peaks in AE energy rate, clear increases in hit activity, and the pre-failure region are used to identify damage-active intervals. The DIC frames closest to these intervals are then examined to determine whether strain localization or strain redistribution develops around the initial crack region.

For specimens with strain gauge measurements, the local strain response is evaluated over the same intervals. The strain gauge data are not used to reconstruct the crack path. Instead, they are used to check whether the local strain response shows a change in trend, slope variation, or abrupt strain variation during the same interval in which DIC localization and AE activity are observed. For specimens without strain gauge data, the crack-related stage is interpreted from the agreement between DIC and AE results. For strain-gauged specimens, the strain gauge response provides additional local mechanical confirmation. Therefore, a stage is considered more strongly supported when DIC strain localization, increased AE activity, and local strain response changes occur within the same loading interval.

4.2 Results and Discussion

4.2.1 Global Stress-Strain Response of Cracked Laminate Specimens

The global tensile responses of the cracked laminate specimens are first evaluated using the stress-strain curves obtained from the mechanical testing system. This evaluation provides the mechanical reference for the subsequent DIC-AE-SG correlation. In particular, the peak stress, strain level at peak response, post-peak stress drop, and residual load-carrying behavior are examined for each laminate configuration. Since the main objective of this study is to interpret crack propagation through multi-instrument evidence, the global mechanical response is not treated as a standalone failure analysis. Instead, it is used to identify the main loading stages and to support the interpretation of DIC strain localization, AE activity, and, when available, strain gauge response.

Figure 4.1 shows the stress-strain responses of the mixed-orientation laminates. The (0/90/0) laminate with a 90º initial crack reaches a maximum tensile stress of approximately 294 MPa at a strain of about 0.85%. After the peak response, a sudden stress drop is observed, followed by a partial load recovery and a secondary post-peak response. This indicates that the specimen does not fail through a single instantaneous event, but retains a reduced load-carrying capacity after the first major damage stage. In contrast, the (0/90/0) laminate with a 45º initial crack reaches a similar peak stress, approximately 298 MPa, at a much lower strain level of about 0.43%, followed by abrupt failure. The (90/0/90) laminate with a 45º initial crack

exhibits a lower peak stress of approximately 250 MPa and a more compliant response, with failure occurring at a strain close to 0.90%. These differences show that both the initial crack orientation and the laminate sequence strongly affect the stiffness, strength, and post-peak response of the cracked laminates.

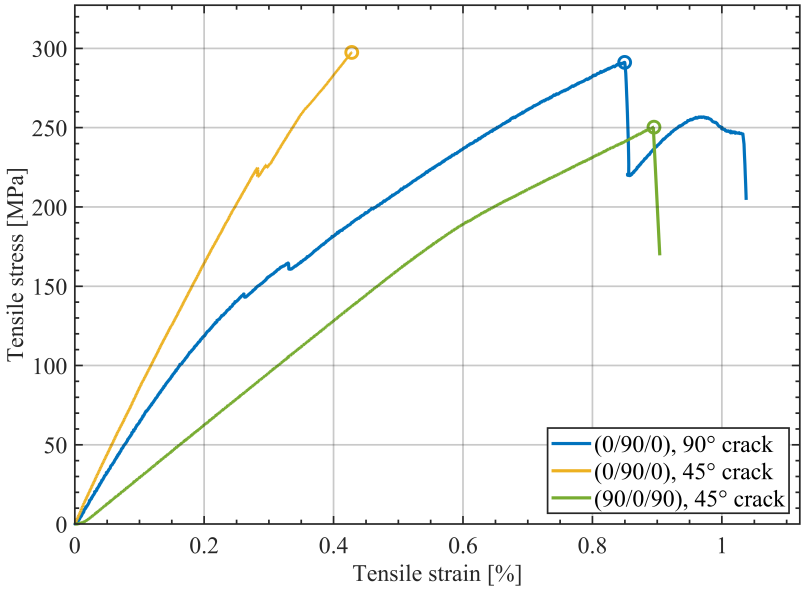

Figure 4.1 Stress-strain responses of the mixed-orientation cracked laminate specimens under tensile loading: (0/90/0) laminate with a 90º initial crack, (0/90/0) laminate with a 45º initial crack, and (90/0/90) laminate with a 45º initial crack.

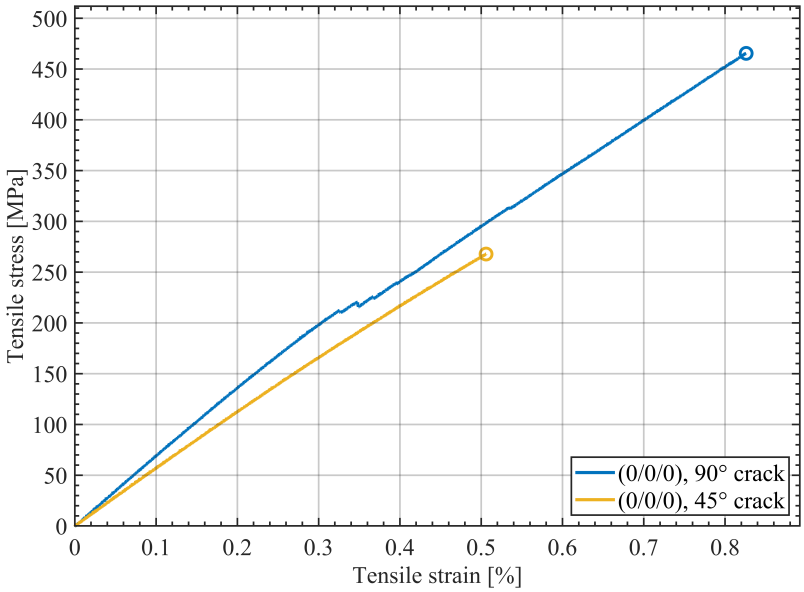

Figure 4.2 Stress-strain responses of the 0º-dominated cracked laminate specimens under tensile loading: (0/0/0) laminate with a 90º initial crack and (0/0/0) laminate with a 45º initial crack.

Figure 4.2 compares the two (0/0/0) laminates with different initial crack orien-

tations. Both specimens exhibit an almost linear tensile response up to failure, reflecting the dominant contribution of the 0º plies under the applied tensile loading. The specimen with a 90º initial crack reaches the highest stress among all tested configurations, approximately 468 MPa, at a strain of about 0.82%. The specimen with a 45º initial crack fails earlier, with a maximum stress of approximately 268 MPa at a strain of about 0.51%. This reduction indicates that the inclined crack introduces a more critical stress state in the 0º-dominated laminate, promoting earlier damage development and reducing the load-carrying capacity.

Figure 4.3 presents the stress-strain responses of the (90/90/90) laminates. Compared with the other laminate families, these specimens show very low tensile strength and limited strain capacity. The 45º and 90º crack configurations reach peak stresses of approximately 7.1 MPa and 8.5 MPa, respectively, followed by abrupt stress drops. This behavior is consistent with the transverse loading condition of 90º plies, where the matrix-dominated response controls the global tensile resistance. Although the 90º crack specimen shows a slightly higher peak stress, both configurations exhibit brittle fracture-dominated behavior with almost no residual load-carrying capacity after the peak.

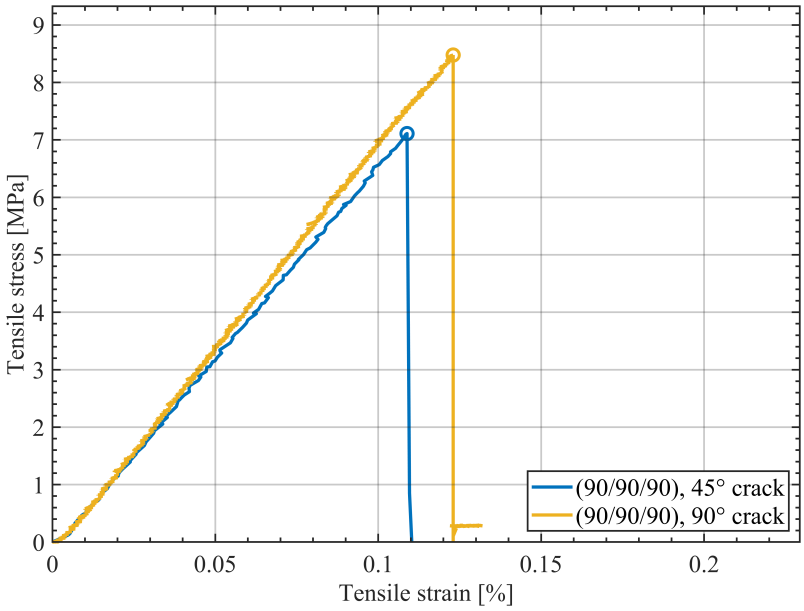

Figure 4.3 Stress-strain responses of the 90º-dominated cracked laminate specimens under tensile loading: (90/90/90) laminate with a 45º initial crack and (90/90/90) laminate with a 90º initial crack.

Overall, the global stress-strain curves reveal three distinct mechanical response groups. The mixed-orientation laminates show intermediate strength with configuration-dependent post-peak behavior. The 0º-dominated laminates provide the highest tensile resistance, but their strength is strongly reduced when the crack

is inclined at 45°. The 90°-dominated laminates exhibit the weakest and most brittle response due to matrix-dominated transverse loading. These global trends provide the mechanical basis for the following multi-instrument interpretation, where DIC, AE, and strain gauge measurements are used to clarify how the observed stress drops and failure transitions are related to crack localization and damage activity.

4.2.2 DIC-Based Crack Propagation Assessment Using Von Mises Equivalent Strain Fields

The spatial development of crack-related deformation is evaluated using DIC-based von Mises equivalent strain fields. Representative configurations are selected to compare the effects of initial crack orientation and laminate sequence on the localization pattern. The selected cases are the (0/90/0) laminate with a 90° initial crack, the (0/90/0) laminate with a 45° initial crack, and the (90/0/90) laminate with a 45° initial crack.

The DIC maps are used to follow the evolution of localized deformation around the initial crack region. Since the objective is to evaluate the crack-related localization path rather than to compare absolute strain magnitudes between different specimens, a fixed color scale is used within each specimen-specific figure. The selected fields show the transition from early crack-tip strain concentration to a more developed crack propagation path.

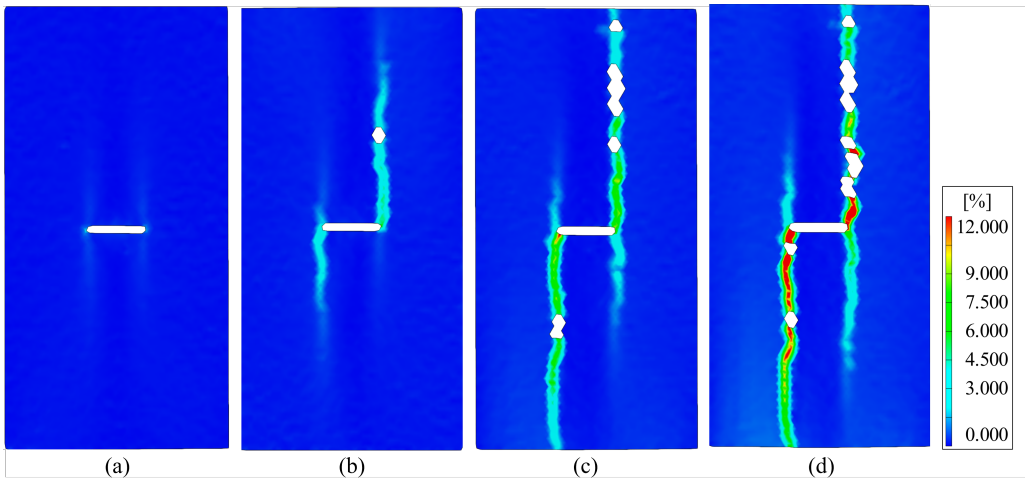

Figure 4.4 DIC-based von Mises equivalent strain evolution of the (0/90/0) laminate with a 90° initial crack at representative times: (a) t = 20 s, (b) t = 40 s, (c) t = 60 s, and (d) t = 95 s.

For the (0/90/0) laminate with a 90º initial crack, the equivalent strain fields at approximately 20, 40, 60, and 95 s are shown in Figure 4.4. At t = 20 s, only weak strain concentration is observed near the crack tips. At t = 40 s, the localization becomes more visible and starts to extend from the initial crack region. At t = 60 s, a clearer localization path develops, indicating progressive crack-related deformation. At t = 95 s, the localization becomes more continuous and intense, showing the developed crack propagation path. The white regions correspond to areas where DIC data is not available due to severe local deformation or correlation loss.

These results show that the crack-related strain localization develops progressively from the initial crack tips into a continuous propagation path. This DIC-based spatial evidence is later compared with the AE activity to evaluate whether the acoustic response supports the same crack propagation process.

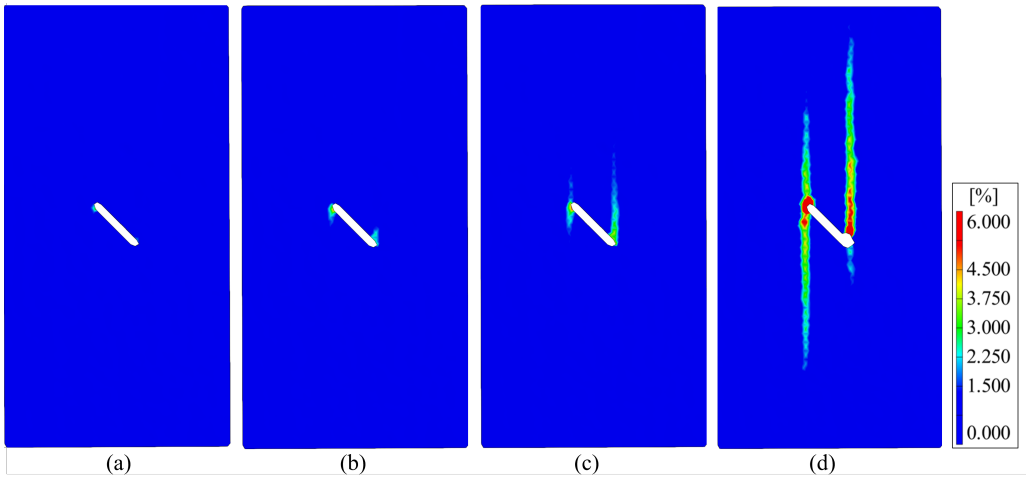

Figure 4.5 DIC-based von Mises equivalent strain evolution of the (0/90/0) laminate with a 45º initial crack at representative times: (a) t = 23 s, (b) t = 34 s, (c) t = 41 s, and (d) t = 49 s.

For the (0/90/0) laminate with a 45º initial crack, the DIC-based von Mises equivalent strain fields show a progressive development of crack-related localization, as presented in Figure 4.5. At t = 23 s, the strain concentration is mainly limited to the vicinity of the initial crack tips, indicating the onset of crack-near localization. At t = 34 s, the localized regions become more pronounced at both crack tips, but the propagation path is still not fully developed. At t = 41 s, the strain field starts to form clearer bands extending away from the initial crack region, showing the development of the crack-related deformation path. In the final stage at t = 49 s, the localization bands become continuous and more intense, indicating advanced crack propagation.

Although the initial crack is oriented at 45º, the dominant localization pattern de-

velops mainly in the horizontal direction from the crack-tip regions. This indicates that the observed crack propagation is governed not only by the initial notch orientation, but also by the laminate lay-up and the deformation path activated under tensile loading.

For the (90/0/90) laminate with a 45º initial crack, the DIC-based von Mises equivalent strain fields are shown in Figure 4.6. The strain localization first appears around the crack-tip regions and progressively intensifies during loading. At t = 60 s, the localized deformation is mainly confined to the crack tips. At t = 80 s and t = 105 s, the localization becomes more pronounced and extends from the crack-tip regions, indicating the development of the crack-related deformation path. Compared with the (0/90/0) laminate with a 45º initial crack, the localization pattern in this specimen tends to develop more along the global vertical direction, indicating that the propagation path is influenced by the laminate sequence in addition to the initial crack orientation.

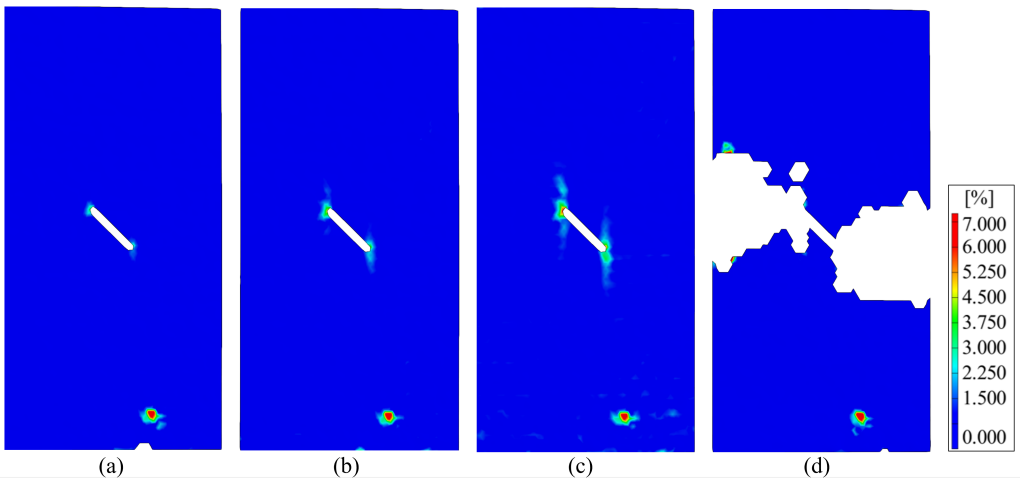

Figure 4.6 DIC-based von Mises equivalent strain evolution of the (90/0/90) laminate with a 45º initial crack at representative times: (a) t = 60 s, (b) t = 80 s, (c) t = 105 s, and (d) t = 107 s.

At the final stage, t = 107 s, the specimen exhibits severe crack opening and extensive local loss of valid DIC data around the propagated crack region. The white regions in the final panel should not be interpreted as low-strain or undamaged areas. They correspond to missing measurement zones caused by surface separation and detachment of the painted speckle layer during fracture, which prevents reliable optical tracking of the affected surface points. Therefore, the final frame is used to identify the fracture-dominated state and the extent of severe crack opening, while the preceding frames are used to evaluate the progressive development of the strain-localization path.

4.2.3 AE-Based Activity Analysis and DIC-Correlated Crack Propagation

The specimen-wise AE-DIC correlation is used to relate the time-dependent acoustic response to the spatial development of crack-related strain localization. All specimens are monitored using DIC and AE, while strain gauge measurements are additionally available for the (0/0/0) laminate with a 90º initial crack, the (0/0/0) laminate with a 45º initial crack, and the (90/90/90) laminate with a 90º initial crack. For these configurations, the strain gauge response is also evaluated as local mechanical evidence.

4.2.3.1 (0/90/0) Laminate with a 90º Initial Crack Specimen

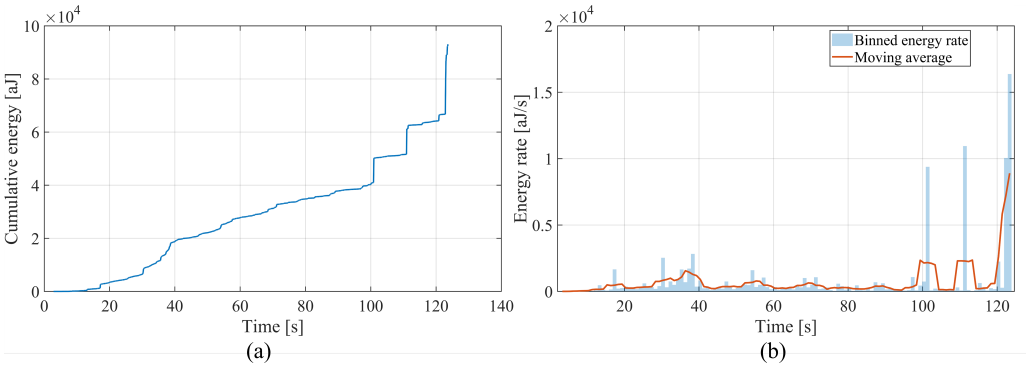

Figure 4.7 AE energy response of the (0/90/0) laminate with a 90º initial crack: (a) cumulative AE energy and (b) binned AE energy rate.

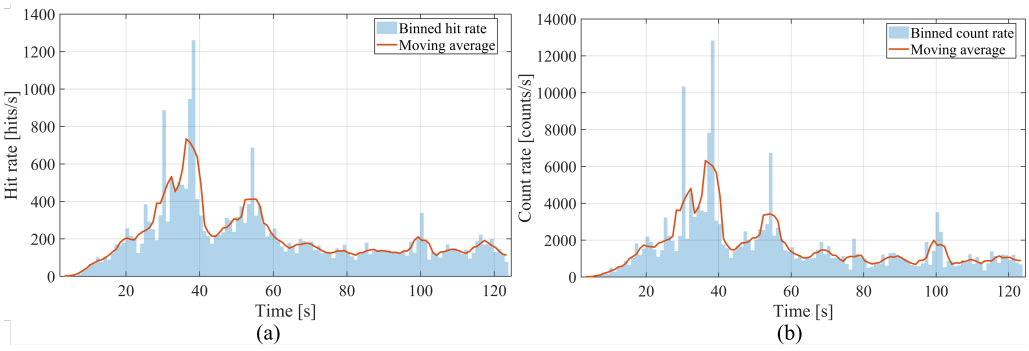

Figure 4.8 AE activity response of the (0/90/0) laminate with a 90º initial crack: (a) binned hit rate and (b) binned count rate.

For (0/90/0) laminate with a 90º initial crack, the first notable acoustic emission

(AE) activity occurs around 35-40 s. At this interval, the cumulative AE energy begins to increase in Figure 4.7(a), while the energy rate in Figure 4.7(b) remains moderate compared with the later peaks. In contrast, the hit rate and count rate in Figure 4.8(a,b) shows a clear early increase, indicating that this interval is dominated by frequent AE activity rather than by major energy release. The corresponding DIC field at t = 40 s in Figure 4.9(a) shows the first visible crack-near strain localization, confirming that the early acoustic activity has a spatial counterpart around the initial crack region.

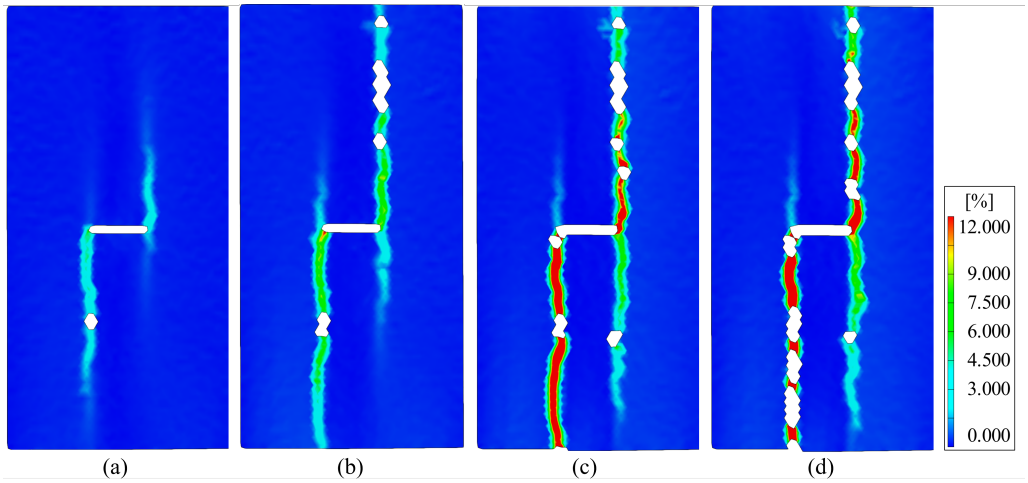

Figure 4.9 DIC-based von Mises equivalent strain fields corresponding to selected AE activity intervals: (a) t = 40 s, (b) t = 60 s, (c) t =100 s, and (d) t = 120 s.

At approximately 60 s, the AE response continues to develop, but without a strong energy-rate peak. The cumulative energy in Figure 4.7(a) increases gradually, and the hit/count activity in Figure 4.8(a,b) remains present but less pronounced than the early activity burst. The DIC field in Figure 4.9(b) shows that the localized strain region becomes more continuous and starts to define a clearer crack-related path. This indicates that the crack path begins to develop spatially before the most energetic AE events are recorded.

Around 100 s, the AE response becomes more energetic. A distinct increase in cumulative energy is observed in Figure 4.7(a), and the energy-rate curve in Figure 4.7(b) shows a clear peak. The hit and count responses in Figure 4.8(a,b) also indicate renewed acoustic activity, but the main difference from the early interval is the stronger energy contribution. The DIC field in Figure 4.9(c) shows a more developed localization band extending from the initial crack region. Therefore, the AE activity around this time corresponds to a clear intensification of the crack-related deformation field.

Near 120 s, the most severe acoustic response is observed. The cumulative energy in Figure 4.7(a) rises sharply, and the energy rate in Figure 4.7(b) reaches its highest level. Although the hit rate and count rate in Figure 4.8(a,b) are not as dominant as the early activity burst, the much higher energy response shows that this interval is governed by fewer but more energetic AE events. The DIC field in Figure 4.9(d) supports this interpretation by showing severe localization along the propagated crack region, together with local DIC correlation loss. These white regions are not interpreted as strain values; they indicate unavailable DIC data caused by severe local deformation, crack opening, or surface discontinuity.

Overall, the combined AE-DIC response indicates that crack propagation does not occur as a single final event. Instead, the process starts with frequent low-to-moderate energy acoustic activity associated with the first visible crack-near localization, then develops into a more continuous localization path, and finally reaches a severe propagation stage characterized by high-energy AE release and local loss of DIC correlation. This sequence shows that AE captures the timing and intensity of crack-related activity, while DIC reveals the corresponding spatial development of the crack path.

4.2.3.2 (0/90/0) Laminate with a 45º Initial Crack Specimen

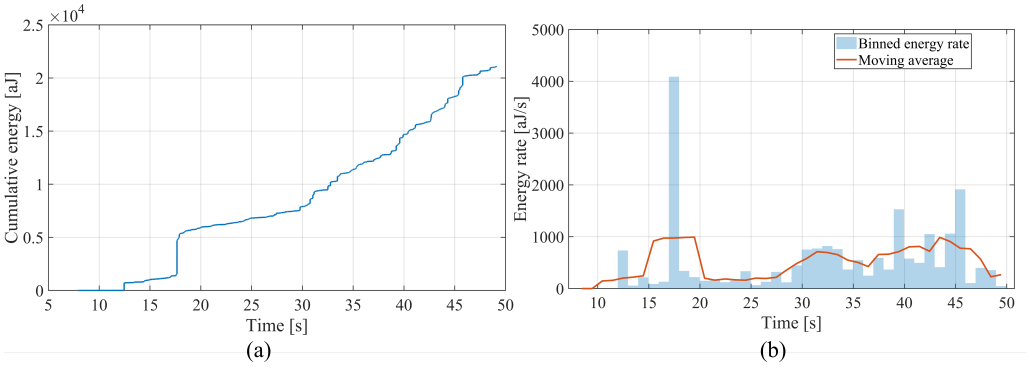

Figure 4.10 AE energy response of the (0/90/0) laminate with a 45º initial crack: (a) cumulative AE energy and (b) binned AE energy rate.

For the (0/90/0) laminate with a 45º initial crack, the AE response shows several distinct activity intervals rather than a single dominant acoustic event. The cumulative AE energy in Figure 4.10(a) starts to increase during the early part of the test, with a clear energy-rate peak around 17-19 s in Figure 4.10(b). However, this early energy release is not yet accompanied by a clearly developed surface localization

path in the DIC field. The first optically traceable localization is observed later, at 23 s, as shown in Figure 4.12(a), where strain concentration appears around the initial crack-tip region.

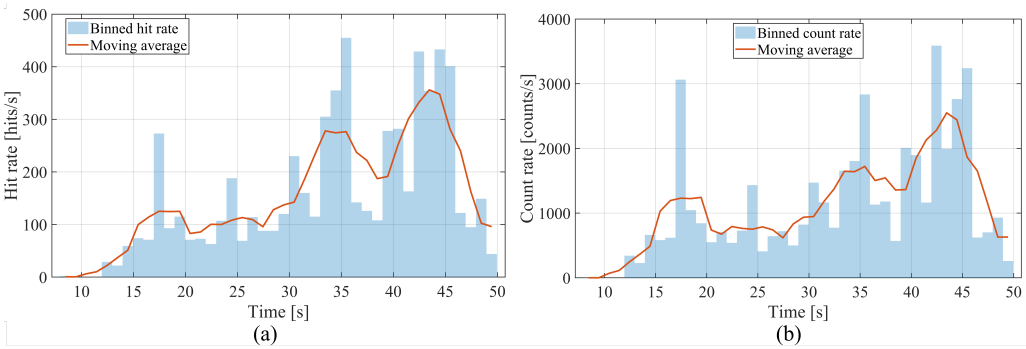

Figure 4.11 AE activity response of the (0/90/0) laminate with a 45º initial crack: (a) binned hit rate and (b) binned count rate.

Between 30 s and 36 s, the AE response becomes more active again. The energy-rate response in Figure 4.10(b) increases, while the hit rate and count rate in Figure 4.11(a,b) also show enhanced acoustic activity. The corresponding DIC field at t = 34 s in Figure 4.12(b) shows that the strain concentration around the crack tips becomes more pronounced. This indicates that the early acoustic activity has evolved into a more spatially organized crack-near deformation pattern.

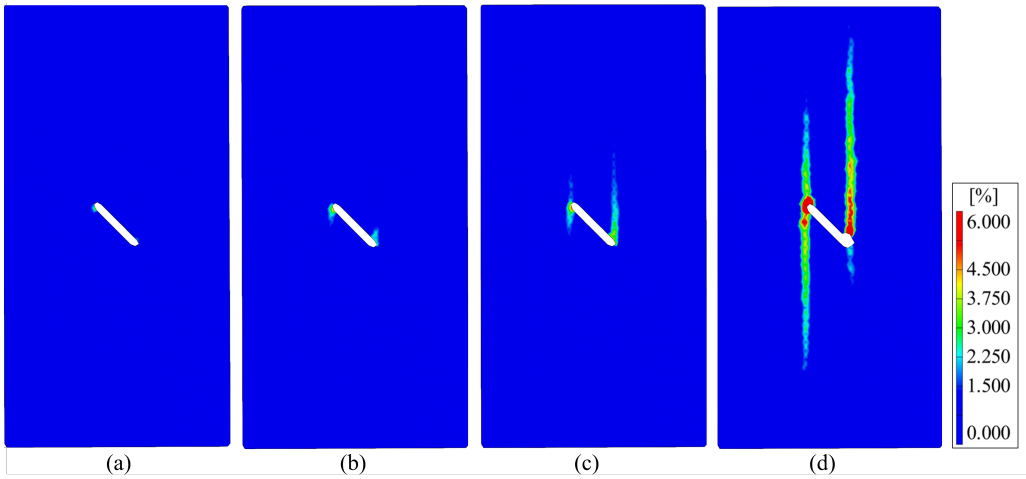

Figure 4.12 DIC-based von Mises equivalent strain fields corresponding to selected AE activity intervals: (a) t = 23 s, (b) t = 34 s, (c) t = 41 s, and (d) t = 49 s.

A stronger AE-DIC correspondence is observed during the interval between approximately 40 s and 45 s. In this range, the hit rate and count rate in Figure 4.11(a,b) reach their highest levels, and the energy-rate response in Figure 4.10(b) remains active. The DIC field at t = 41 s in Figure 4.12(c) shows a clearer crack-related

localization path extending from the crack-tip regions. Therefore, the increase in acoustic event density is accompanied by the visible development of the surface strain localization path.

At the final stage, around 49 s, the cumulative AE energy in Figure 4.10(a) reaches its final level, and the DIC field in Figure 4.12(d) shows the most developed localization pattern. The strain bands extend from the crack-tip regions and form a more continuous crack-related deformation path. Overall, Figures 4.10, 4.11, and 4.12 show that the AE response detects the onset of damage-related activity before a clearly developed DIC localization path becomes visible, while the later increases in energy rate, hit rate, and count rate coincide with the progressive development of crack-related strain localization.

4.2.3.3 (90/0/90) Laminate with a 45º Initial Crack Specimen

For the (90/0/90) laminate with a 45º initial crack, the initial AE activity becomes noticeable at approximately 60 s, as indicated by the early rise in cumulative AE energy and hit rate in Figures 4.13 and 4.14. The DIC field at t = 60 s in Figure 4.15(a) corresponds to the onset of this AE activity. At this stage, the von Mises equivalent strain field shows localized strain concentration around the crack-tip regions, while a fully developed localization path is not yet formed. This indicates that the first measurable AE activity coincides with the early development of crack-tip strain localization.

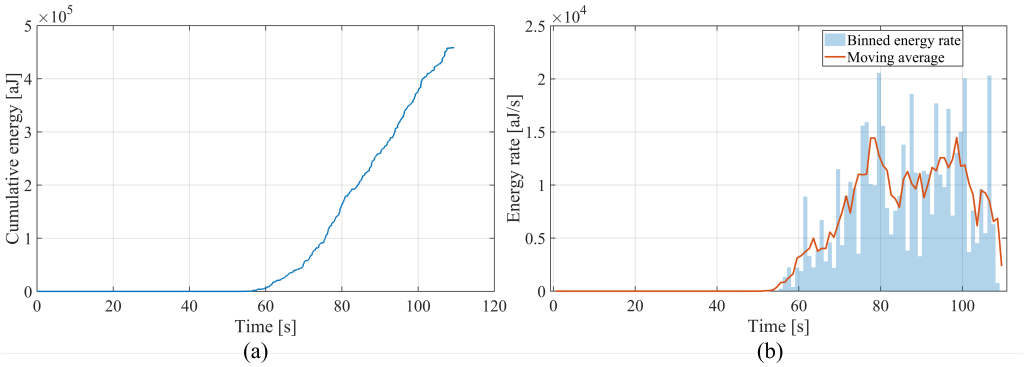

Figure 4.13 AE energy response of the (90/0/90) laminate with a 45º initial crack: (a) cumulative AE energy and (b) binned AE energy rate.

At t = 80 s, Figure 4.15(b) shows that the strain localization becomes more pronounced around both crack tips. This time corresponds to one of the most active

AE intervals, where the energy-rate response in Figure 4.13(b) increases strongly and the hit-rate and count-rate responses in Figure 4.14(a,b) also reach elevated levels. The simultaneous increase in AE activity and DIC-based strain localization indicates that the acoustic response is associated with the progressive development of crack-related deformation around the initial crack region.

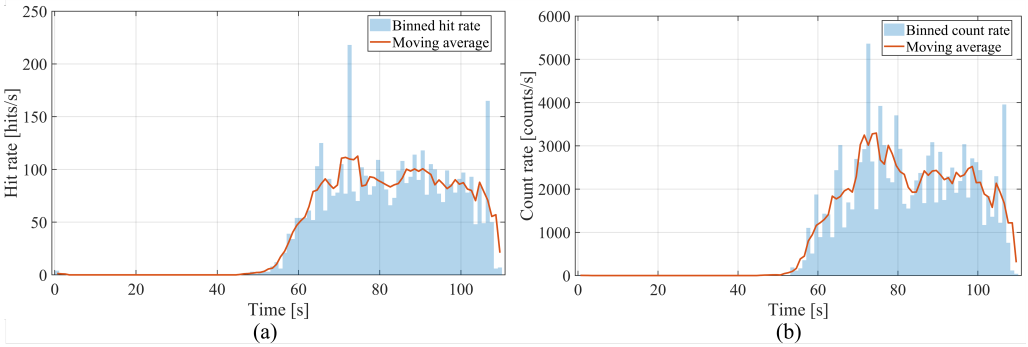

Figure 4.14 AE activity response of the (90/0/90) laminate with a 45º initial crack: (a) binned hit rate and (b) binned count rate.

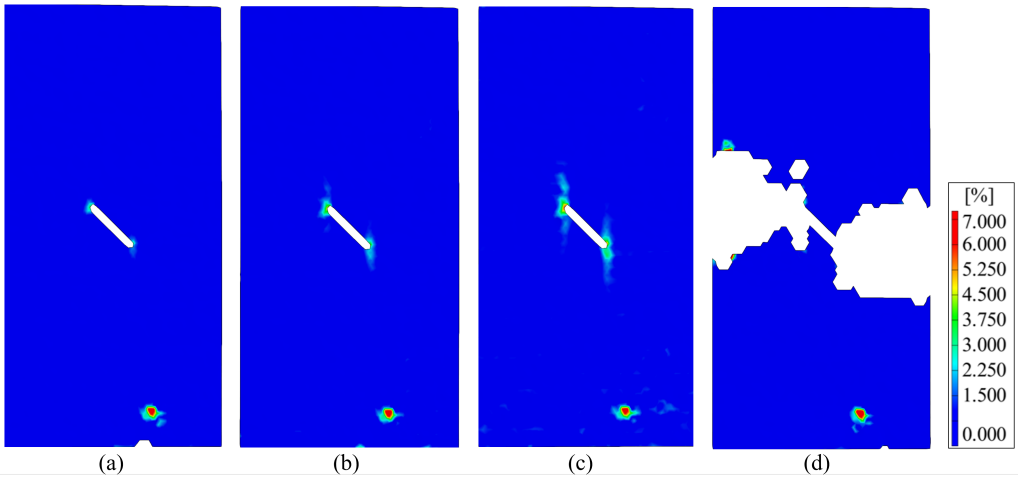

Figure 4.15 DIC-based von Mises equivalent strain fields corresponding to selected AE activity intervals: (a) t = 60 s, (b) t = 80 s, (c) t = 100 s, and (d) t = 107 s.

At t = 100 s, the DIC field in Figure 4.15(c) shows further intensification of the localized strain field. The localization extends more clearly from the crack-tip regions, following the direction of the developing crack path. This stage coincides with sustained AE activity in Figure 4.13(b) and Figure 4.14(a,b), as well as the continued increase of cumulative AE energy in Figure 4.13(a). Therefore, the AE response during this interval is consistent with an actively evolving crack-propagation process rather than an isolated acoustic burst.

At the final stage, t = 107 s, the DIC field in Figure 4.15(d) shows severe crack opening and extensive loss of valid DIC data around the propagated crack region.

This final fracture state coincides with the late-stage acoustic activity observed in Figure 4.13 and Figure 4.14. Although the cumulative AE energy has already increased substantially before this point, it continues to rise until the end of the test, indicating that additional acoustic energy is released during the final crack-opening process. At the same time, the hit-rate and count-rate responses remain active in the last loading interval, showing that the final fracture is accompanied not only by a large deformation event in the DIC field, but also by sustained acoustic activity. The white regions in Figure 4.15(d) therefore correspond to missing measurement zones caused by surface separation and detachment of the painted speckle layer during fracture, while the simultaneous AE response confirms that this stage represents an active fracture process rather than a purely optical measurement artifact.

Overall, Figures 4.13, 4.14, and 4.15 demonstrate a clear temporal consistency between AE activity and DIC-based crack localization for the (90/0/90) laminate with a 45º initial crack. The AE response begins when crack-tip localization first becomes visible, increases as the localized deformation develops, and remains active up to the fracture-dominated stage. This behavior indicates that the damage process in this specimen is governed by late-stage crack propagation, with AE activity closely following the progressive intensification and final breakdown of the DIC localization path.

4.2.3.4 (0/0/0) Laminate with a 90º Initial Crack Specimen

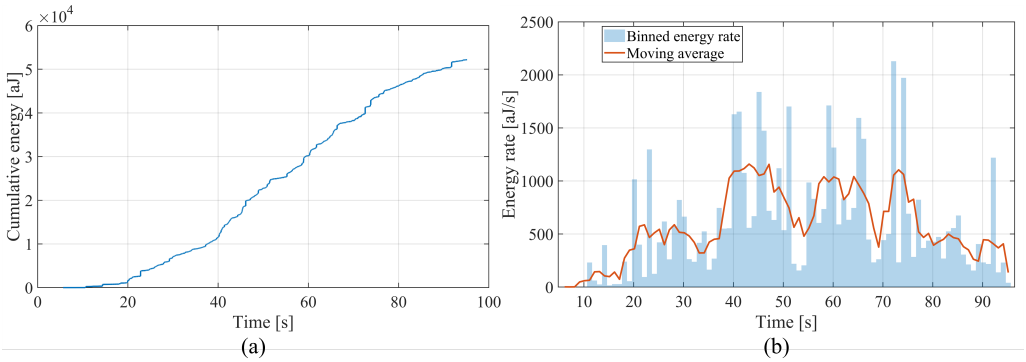

Figure 4.16 AE energy response of the (0/0/0) laminate with a 90º initial crack: (a) cumulative AE energy and (b) binned AE energy rate.

For the (0/0/0) laminate with a 90º initial crack, the combined AE, DIC, and strain gauge responses reveal a progressive crack-propagation process accompanied by a clear redistribution of the local strain field. The AE response in Figures 4.16

and 4.17 indicates that the acoustic activity is distributed over a broad portion of the test, rather than being limited to a single final fracture event. This behavior suggests a gradual accumulation of damage-related events, where the crack-related deformation evolves through successive stages of activity.

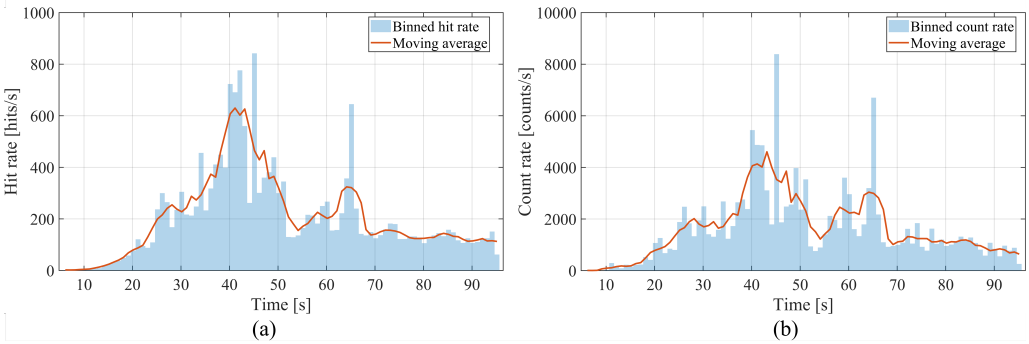

Figure 4.17 AE activity response of the (0/0/0) laminate with a 90º initial crack: (a) binned hit rate and (b) binned count rate.

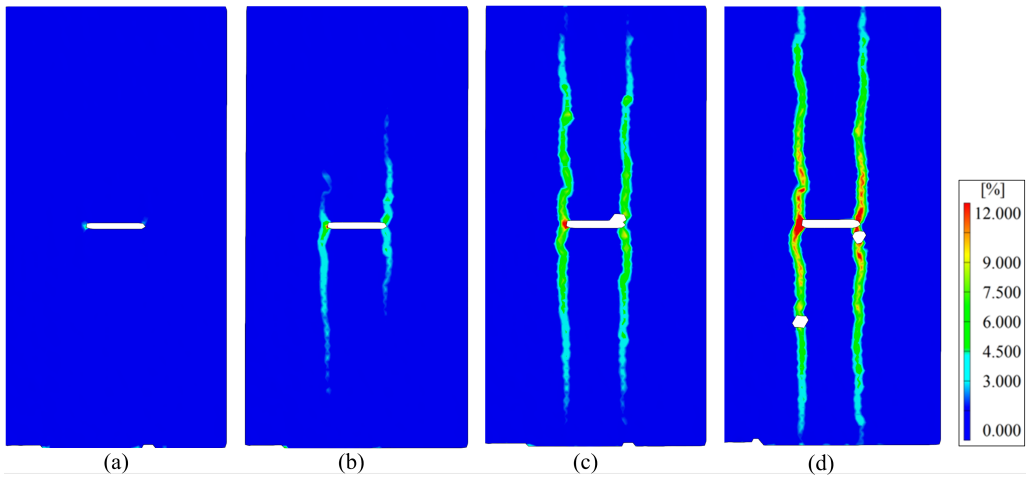

Figure 4.18 DIC-based von Mises equivalent strain fields corresponding to selected AE activity intervals for the (0/0/0) laminate with a 90º initial crack: (a) t = 28 s, (b) t = 43 s, (c) t = 65 s, and (d) t = 95 s.

The first mechanically significant transition occurs during the main acoustic activity interval around 40-50 s. In this interval, the high hit-rate and count-rate response in Figure 4.17 indicates a dense population of acoustic events, while the cumulative energy in Figure 4.16(a) continues to increase through discrete energy releases. This combination suggests that the specimen is not only producing isolated high-energy events, but also undergoing intense distributed acoustic activity. The corresponding DIC field in Figure 4.18(b) shows the emergence of an organized localization pattern around the initial crack region, indicating that the acoustic activity is associated with the transition from local crack-tip deformation to a spatially developed crack-propagation path.

The strain gauge response in Figure 4.19 provides local mechanical evidence for the same transition. SG1, SG3, and SG4 mainly follow the global tensile response in ε_{xx}, whereas SG7 and SG8, located in the upper crack-near region, show a marked reduction in longitudinal strain during the main AE activity interval. This indicates a local unloading or stiffness redistribution near the crack as the deformation path develops. The ε_{yy} response further supports this interpretation: the abrupt changes in SG7 and SG8 occur in the same time range in which AE activity is most intense and DIC localization becomes clearly organized. Therefore, the strain gauge response does not simply reproduce the global loading trend; it captures the local mechanical redistribution induced by crack growth.

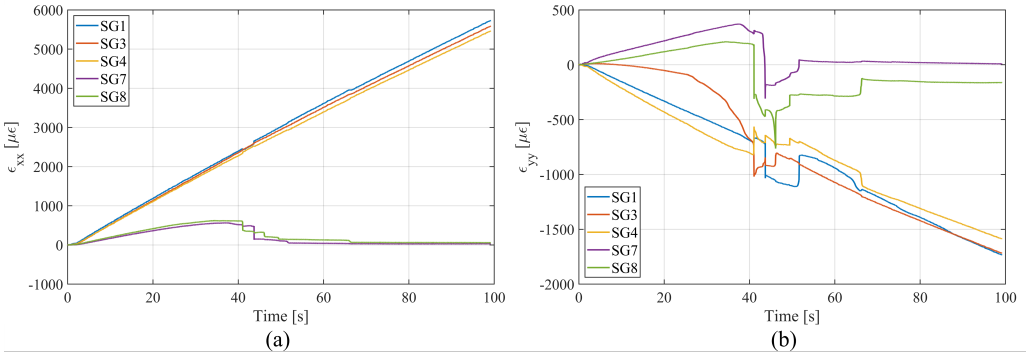

Figure 4.19 Strain gauge response of the (0/0/0) laminate with a 90º initial crack: (a) ε_{xx} and (b) ε_{yy} histories of SG1, SG3, SG4, SG7, and SG8.

After the main event-density interval, the damage process continues with a different acoustic character. The energy-rate response in Figure 4.16(b) remains active between approximately 60 s and 75 s, while the hit-rate and count-rate responses in Figure 4.17 decrease compared with the earlier peak. This indicates that the later stage is less dominated by event density and more associated with continued energy release from the already developed crack-localization path. Consistently, Figure 4.18(c) shows more continuous and intensified strain-localization bands, while Figure 4.19 shows that the crack-near strain gauges have already undergone pronounced redistribution. This suggests that the specimen has moved from the initiation and organization of the crack path toward further propagation along an established deformation band.

At the final stage, the DIC field in Figure 4.18(d) shows a fully developed localization pattern, while the cumulative AE energy in Figure 4.16(a) continues to rise up to the end of the test. The persistence of acoustic energy release after the main strain-gauge redistribution indicates that local gauge-level unloading does not mark the end of damage evolution; rather, it reflects a local redistribution event within a continuing crack-propagation process. In this sense, SG7 and SG8 identify the local

mechanical consequence of crack growth, whereas AE captures the continuing release of acoustic energy and DIC provides the spatial evolution of the localization path.

Overall, the specimen shows strong consistency between the three measurement systems. AE identifies the timing and intensity of damage-related activity, DIC reveals the spatial organization and growth of the crack-related localization path, and strain gauges capture the local redistribution of strain near the crack. The agreement between the main AE activity interval, the onset of organized DIC localization, and the abrupt strain changes in SG7 and SG8 demonstrates that the crack propagation process is progressive and mechanically accompanied by local unloading and strain redistribution around the crack-near region.

4.2.3.5 (0/0/0) Laminate with a 45º Initial Crack Specimen

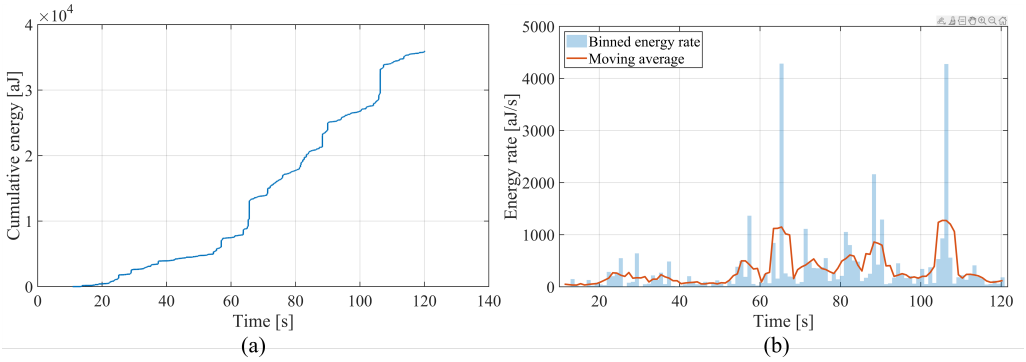

Figure 4.20 AE energy response of the (0/0/0) laminate with a 45º initial crack: (a) cumulative AE energy and (b) binned AE energy rate.

For the (0/0/0) laminate with a 45º initial crack, the combined AE, DIC, and rosette strain gauge responses indicate a progressive mixed-mode crack propagation process rather than a single abrupt fracture event. The cumulative AE energy in Figure 4.20(a) increases in a stepwise manner, with several distinct energy-release intervals distributed over the later part of the test. This response suggests that damage evolution is governed by successive crack-related events, where the acoustic activity becomes progressively stronger as the crack path develops.

The AE energy-rate response in Figure 4.20(b) shows that the most energetic intervals occur after the early loading stage, particularly around approximately 60-70 s, 80-90 s, and 105-110 s. These intervals correspond to discrete energy-release episodes rather than a smooth continuous accumulation. In contrast, the hit-rate and count-

rate responses in Figure 4.21(a,b) show a broader increase in event density, with a strong activity region around 80 s and another pronounced activity interval near 105-110 s. This difference between energy release and event density indicates that the specimen does not evolve through a single type of acoustic activity. Instead, some intervals are characterized by dense AE activity, whereas others are governed by fewer but more energetic events.

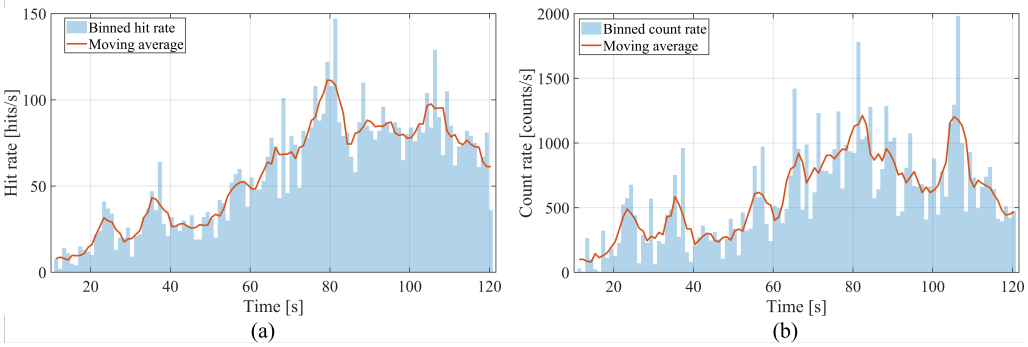

Figure 4.21 AE activity response of the (0/0/0) laminate with a 45º initial crack: (a) binned hit rate and (b) binned count rate.

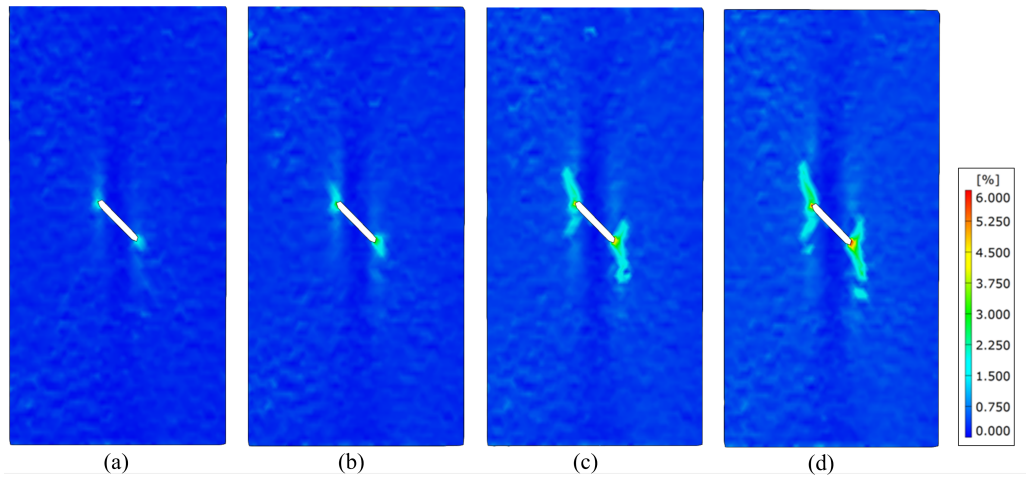

Figure 4.22 DIC-based von Mises equivalent strain fields corresponding to selected AE activity intervals for the (0/0/0) laminate with a 45º initial crack: (a) t = 65 s, (b) t = 82 s, (c) t = 106 s, and (d) t = 120 s.

The DIC fields in Figure 4.22 provide the spatial counterpart of this acoustic behavior. At the earlier selected stage, the strain localization is mainly confined to the crack-tip region, indicating the onset of crack-related deformation. As the AE activity becomes stronger, the localization pattern becomes more spatially organized around the inclined crack. The later DIC fields show a more developed localization path, consistent with the stepwise increase in cumulative AE energy. Therefore, the AE response identifies the temporal development of damage activity, while the DIC

field confirms that these acoustic intervals correspond to the growth and intensification of the crack-related strain-localization zone.

The rosette strain gauge response in Figure 4.23 further clarifies the local deformation character associated with this process. In Figure 4.23(a), the longitudinal strain component ε_{xx} increases monotonically for all selected gauges, indicating that the specimen continues to carry the global tensile deformation throughout the test. However, the strain levels are not uniform among the gauges. SG3 exhibits the highest ε_{xx} response, while SG7 and SG8 remain at lower longitudinal strain levels. This difference indicates that the inclined crack produces a non-uniform redistribution of the axial strain field around the crack-near region.

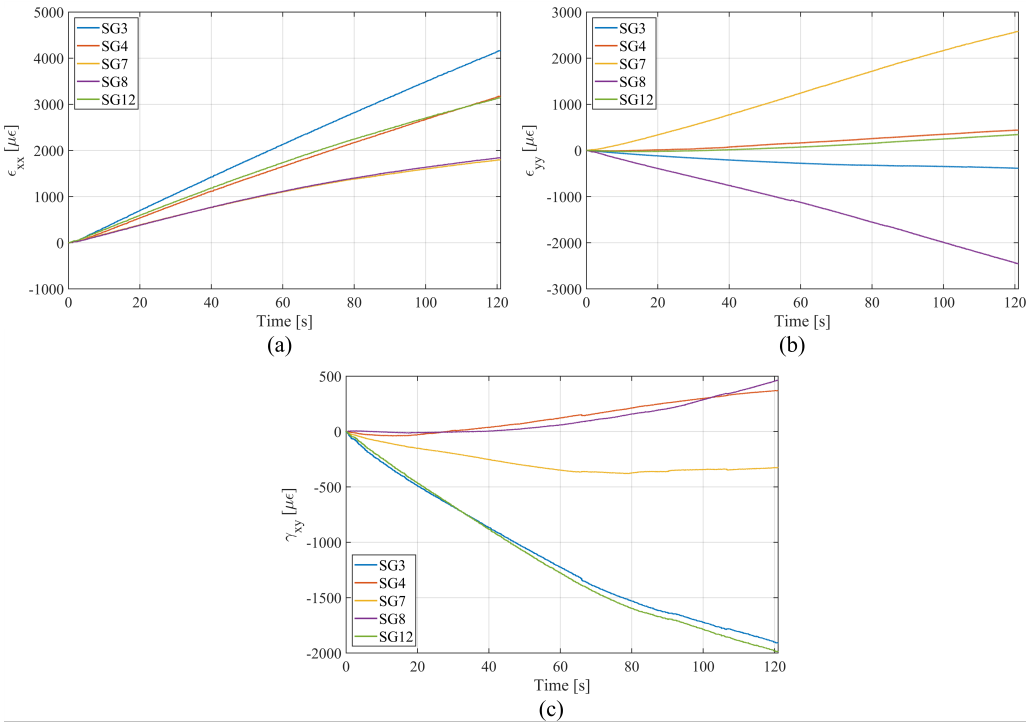

Figure 4.23 Rosette strain gauge response of the (0/0/0) laminate with a 45º initial crack: (a) ε_{xx}, (b) ε_{yy}, and (c) γ_{xy} histories of SG3, SG4, SG7, SG8, and SG12.

The transverse and shear components provide a more direct indication of the local mixed-mode character. In Figure 4.23(b), SG7 and SG8 exhibit opposite transverse strain trends, with SG7 developing a strong positive ε_{yy} response and SG8 developing a strong negative ε_{yy} response. This opposite-sign behavior indicates that the strain field around the inclined crack is not dominated by uniform axial stretching alone; instead, the crack-near region undergoes asymmetric transverse deformation. This interpretation is further supported by the γ_{xy} response in Figure 4.23(c), where SG3 and SG12 develop a pronounced negative shear strain, whereas SG4 and SG8 evolve toward positive shear values. The sign-dependent shear response among the rosette

gauges indicates a shear-coupled redistribution of the local strain field around the inclined crack.

The agreement between the AE, DIC, and rosette measurements is particularly important for interpreting the 45º crack configuration in the (0/0/0) laminate. The AE results identify the active damage intervals and show that the later stage involves both high event density and discrete energetic releases. The DIC fields show that these intervals correspond to the formation and growth of a localized crack-related deformation path. The rosette gauges demonstrate that this localization is accompanied by directional strain redistribution, especially through the transverse and shear components. Therefore, the specimen is characterized by progressive crack propagation with a strong mixed-mode deformation character, where the inclined crack geometry promotes both normal-strain localization and shear-coupled local strain redistribution.

Overall, the (0/0/0) laminate with a 45º initial crack shows that the use of rosette gauges provides additional mechanical information beyond the von Mises DIC field. While DIC identifies the spatial development of crack-related localization, the rosette strain components reveal how the local strain state evolves during this process. The simultaneous increase in AE activity, the development of the DIC localization path, and the sign-dependent γ_{xy} response indicate that the damage evolution of this specimen is governed by progressive mixed-mode crack propagation rather than purely tensile crack opening.

4.2.3.6 (90/90/90) Laminate with a 45º Initial Crack Specimen

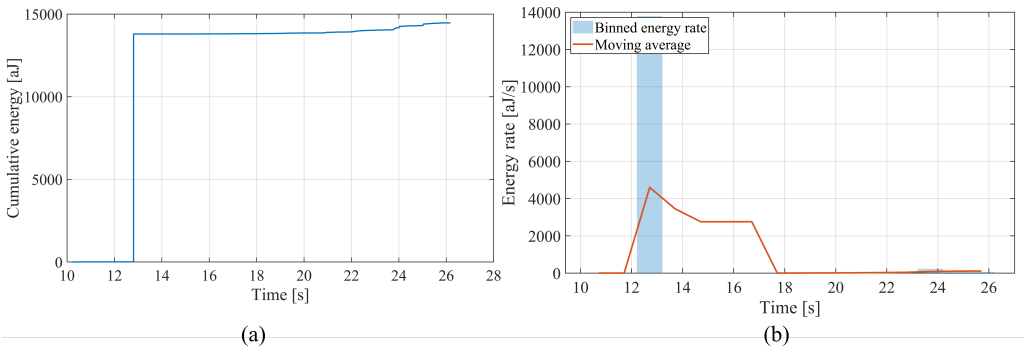

Figure 4.24 AE energy response of the (90/90/90) laminate with a 45º initial crack: (a) cumulative AE energy and (b) binned AE energy rate.

The (90/90/90) laminate with a 45º initial crack exhibits a markedly different response compared with the previously discussed configurations. Instead of a gradual development of crack-related localization over an extended time interval, the response is governed by an abrupt fracture event. This behavior is clearly reflected in the cumulative AE energy response in Figure 4.24(a), where a dominant energy jump occurs at the early stage of the test. The magnitude and suddenness of this jump indicate that a substantial portion of the acoustic energy is released within a very short time window, suggesting a rapid transition from the pre-fracture state to a fully developed crack-propagation condition.

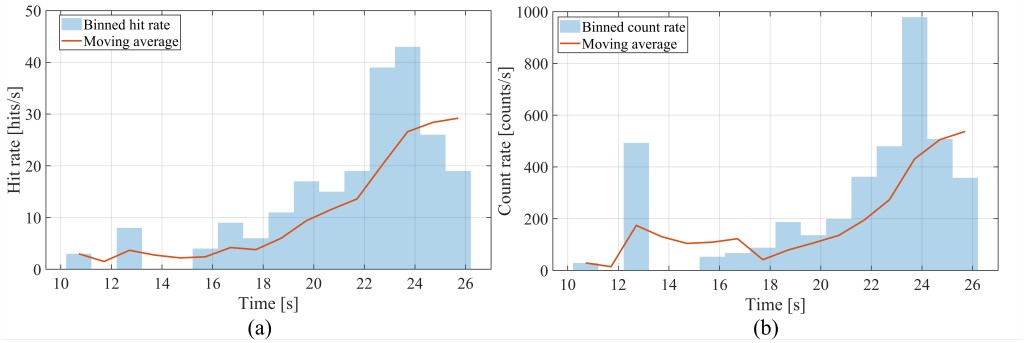

Figure 4.25 AE activity response of the (90/90/90) laminate with a 45º initial crack: (a) binned hit rate and (b) binned count rate.

The binned energy-rate response in Figure 4.24(b) further supports this interpretation. A single dominant energy-release event controls the acoustic energy evolution, whereas the subsequent energy-rate activity remains comparatively limited. Therefore, unlike the specimens showing several distributed energy-release intervals, the damage evolution of the (90/90/90) laminate with a 45º initial crack is mainly characterized by a concentrated fracture-related acoustic event. This indicates that the principal damage process is not progressively accumulated through multiple comparable energy bursts, but is instead dominated by a rapid fracture transition.

The hit-rate and count-rate responses in Figure 4.25(a,b) show increased acoustic activity at later times, particularly after the dominant cumulative energy jump. However, this later activity should not be interpreted as the onset of the primary crack-localization process. Since the cumulative energy has already reached most of its final value immediately after the early dominant event, the later increase in hit and count rates is more consistently associated with post-fracture acoustic activity. Such activity may originate from interactions along the already formed crack surfaces, local rubbing, secondary micro-events, or additional acoustic emissions generated during continued loading after the main fracture event.

The DIC fields in Figure 4.26 provide the spatial confirmation of this abrupt response. Immediately before the transition, the von Mises equivalent strain field does not show a fully developed crack-localization path. Between two consecutive DIC stages, corresponding to approximately t = 14.8 s and t = 14.9 s, a distinct strain-localization band appears abruptly along the crack-propagation direction. This rapid change demonstrates that the crack path becomes visible within a very narrow time interval in the DIC sequence. Therefore, the DIC response does not support a multi-stage gradual localization process for this specimen; rather, it captures the sudden surface manifestation of the fracture event. The small temporal offset between the dominant AE energy release and the abrupt DIC localization is physically reasonable. AE is highly sensitive to the initiation of fracture-related acoustic events, whereas DIC records the surface strain field after the deformation has become spatially localized and optically measurable. Thus, AE can detect the onset of the fracture event slightly before the localization path becomes fully visible in the DIC field. In this sense, the AE and DIC responses are temporally consistent within the same abrupt fracture window, even though they do not necessarily correspond to the exact same instant.

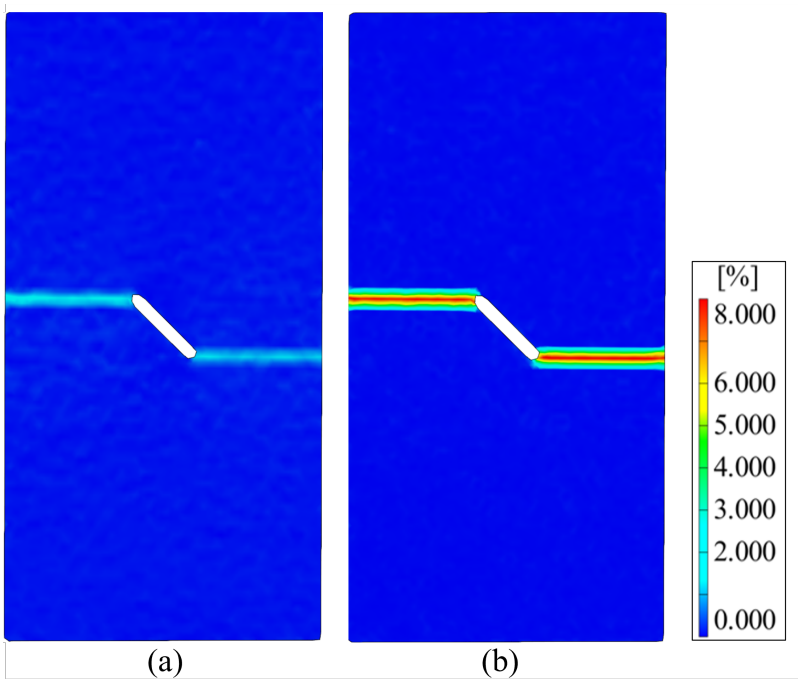

Figure 4.26 DIC-based von Mises equivalent strain fields of the (90/90/90) laminate with a 45º initial crack: (a) immediately before abrupt localization, t = 14.8 s, and (b) immediately after the formation of the crack-localization path, t = 14.9 s.

Overall, the (90/90/90) laminate with a 45º initial crack is characterized by a rapid fracture-dominated damage evolution. The AE response identifies the dominant en-

ergy release associated with the primary fracture event, while the DIC fields confirm the sudden formation of the crack-related localization path. The later hit-rate and count-rate activity represents continued acoustic emissions after the main fracture transition, rather than a separate progressive crack-initiation stage. This combined response indicates that the specimen fails through an abrupt localization and fracture process, in contrast to the more gradual crack-propagation behavior observed in the configurations with distributed AE energy release and progressive DIC localization.

4.2.3.7 (90/90/90) Laminate with a 90º Initial Crack Specimen

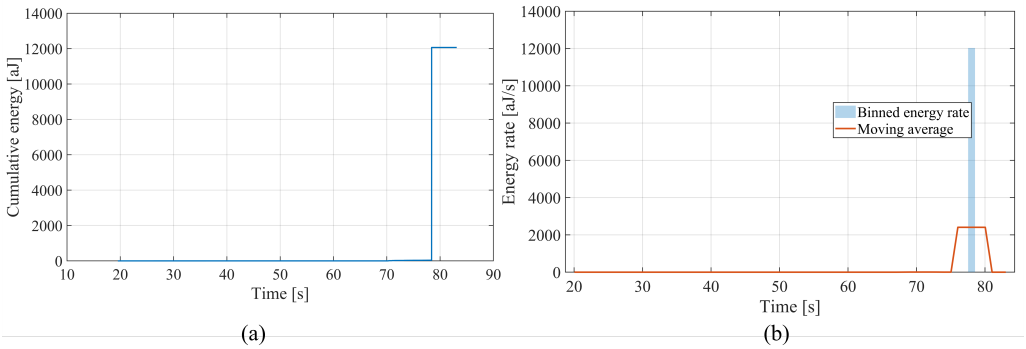

Figure 4.27 AE energy response of the (90/90/90) laminate with a 90º initial crack: (a) cumulative AE energy and (b) binned AE energy rate.

The (90/90/90) laminate with a 90º initial crack exhibits a delayed but abrupt fracture-dominated response. The cumulative AE energy in Figure 4.27(a) remains almost unchanged during most of the test and then increases sharply near the final loading interval. This sudden energy jump indicates that the dominant damage process is concentrated within a narrow time window, rather than being progressively accumulated through several comparable energy-release stages. The binned energy-rate response in Figure 4.27(b) confirms this behavior. A single dominant energy-release event controls the acoustic energy evolution, while the preceding part of the test shows only limited energy activity. The hit-rate and count-rate responses in Figure 4.28(a,b) provide complementary evidence, showing that acoustic event density is also concentrated mainly in the final interval. Therefore, the final fracture event is characterized not only by a large acoustic energy release, but also by a simultaneous increase in the number and intensity of acoustic events. This behavior differs from configurations in which AE activity is distributed over a longer propagation interval.

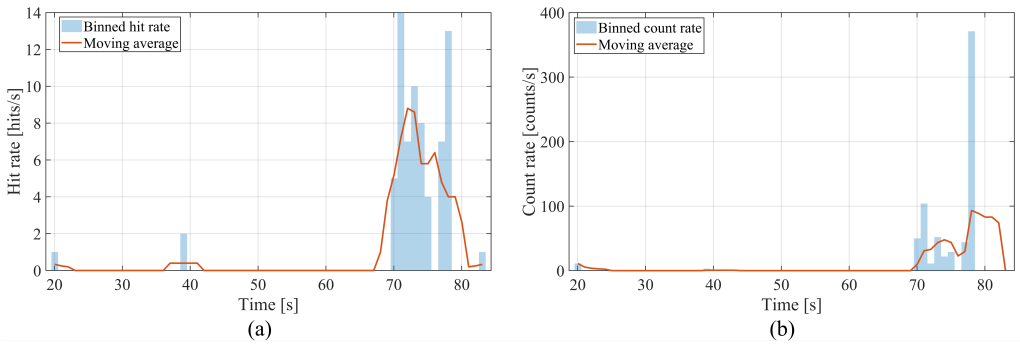

Figure 4.28 AE activity response of the (90/90/90) laminate with a 90º initial crack: (a) binned hit rate and (b) binned count rate.

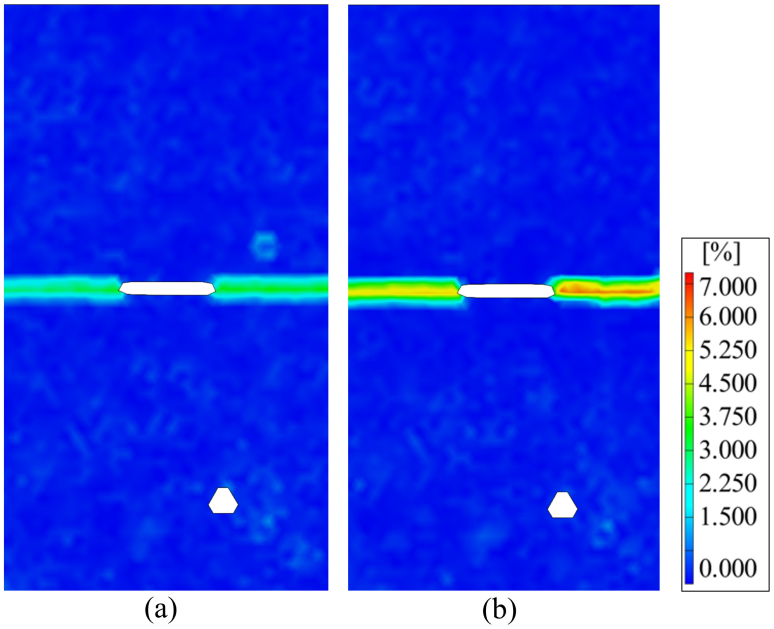

Figure 4.29 DIC-based von Mises equivalent strain fields of the (90/90/90) laminate with a 90º initial crack: (a) immediately before final localization, t = 77.2 s, and (b) immediately after the formation of the fracture-dominated localization band, t = 77.4 s.

The DIC fields in Figure 4.29 provide the spatial counterpart of the AE response. Immediately before the final fracture-dominated stage, the von Mises equivalent strain field already shows a localized deformation band along the crack path. Between two consecutive DIC stages, corresponding to approximately t = 77.2 s and t = 77.4 s, this localization band becomes sharply intensified, indicating the sudden development of the fracture-dominated crack-localization state. The close temporal agreement between the dominant AE energy release and the abrupt intensification of the DIC strain field demonstrates that the primary fracture event is captured consistently by both acoustic and optical measurements.

In the longitudinal strain response, shown in Figure 4.30(a), all selected gauges exhibit a gradual increase in ε_{xx} during loading, indicating that the specimen continues to carry tensile deformation until the final fracture stage. SG1 shows the largest longitudinal strain level, while SG2, SG4, SG7, and SG8 follow lower but consistently increasing trends. This indicates that the crack-near region experiences a distributed axial strain increase prior to final fracture, rather than an early local unloading process. Near the final fracture interval, abrupt changes in the strain gauge signals are observed, consistent with the sudden AE energy release and the rapid intensification of the DIC localization band.

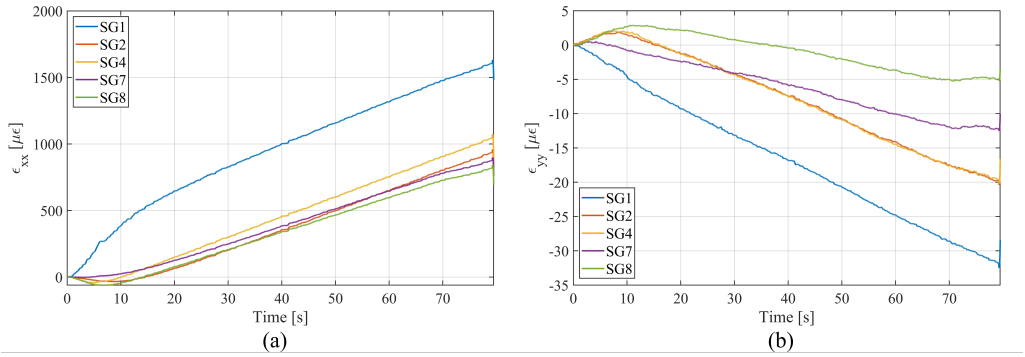

Figure 4.30 Strain gauge response of the (90/90/90) laminate with a 90º initial crack: (a) ε_{xx} and (b) ε_{yy} histories of SG1, SG2, SG4, SG7, and SG8.

The transverse strain response in Figure 4.30(b) shows a different trend. Most selected gauges develop negative ε_{yy} values during loading, indicating transverse contraction associated with the global tensile response and local strain redistribution around the crack region. The magnitude of this transverse response varies among the gauges, showing that the local strain field is not uniform across the specimen. The stronger negative response observed in SG1 and the more moderate responses of the crack-near gauges suggest that the final fracture event is preceded by a non-uniform redistribution of transverse strain around the crack path.

The combined AE, DIC, and strain gauge evidence therefore indicates that the (90/90/90) laminate with a 90º initial crack does not undergo a clearly progressive crack-growth process over a long time interval. Instead, the specimen remains relatively stable during most of the test and then transitions rapidly into a fracture-dominated state. AE identifies the timing and intensity of the final damage event, DIC reveals the sudden spatial intensification of the crack-localization band, and the strain gauges capture the accompanying local strain redistribution immediately before and during final fracture.

4.2.4 Global AE Population Analysis and Cluster-Based Interpretation

4.2.4.1 Global Cluster Definition and Cross-specimen Distribution

The number of AE clusters is first evaluated using the mean silhouette value and the sum of squared errors (SSE), as summarized in Table 4.1. Although the SSE decreases from K = 2 to K = 4, this decrease is expected because increasing the number of clusters naturally reduces the within-cluster distance. Therefore, the mean silhouette value is used as the primary criterion for selecting the cluster number. The highest mean silhouette value is obtained for K = 2, with a value of 0.672. Since K = 3 and K = 4 give lower silhouette values of 0.538 and 0.528, respectively, a two-cluster representation is selected for the global AE population analysis.

Table 4.1 Evaluation of the number of AE clusters based on mean silhouette value and sum of squared errors SSE.

k	Mean Silhouette	SSE
2	0.672	779601.770
3	0.538	573221.126
4	0.528	484790.551

The centroid values of the selected clusters are given in Table 4.2. The first AE population is characterized by higher RA, lower average frequency, lower peak frequency, higher amplitude, higher energy, higher counts, and longer duration. Therefore, this group is referred to as the low-AF / high-RA AE population. In contrast, the second group has lower RA, higher average frequency, higher peak frequency, lower amplitude, lower energy, lower counts, and shorter duration; therefore, it is referred to as the high-AF / low-RA AE population.

The global RA-AF distribution in Figure 4.31 visually supports the centroid-based interpretation. The high-AF / low-RA population is concentrated in the low-RA and relatively high-frequency region, whereas the low-AF / high-RA population extends toward higher RA values and lower average frequencies. This separation indicates that the selected two-cluster representation captures two distinct acoustic event populations in terms of waveform rise behavior and frequency content.

Table 4.2 Centroid characteristics of the selected AE populations.

Cluster	Centroid of RA [ms/V]	Centroid of AF [kHz]	Centroid of Peak Frequency [kHz]	Centroid of Amplitude [dB]	Centroid of Energy [aJ]	Centroid of Counts	Centroid of Duration [μs]	AF/RA Score
Low-AF / high-RA	1.213	82.223	140.348	63.756	8.528	18.823	219.309	67.785
High-AF / low-RA	0.103	268.308	380.132	52.787	0.635	4.240	15.487	2596.520

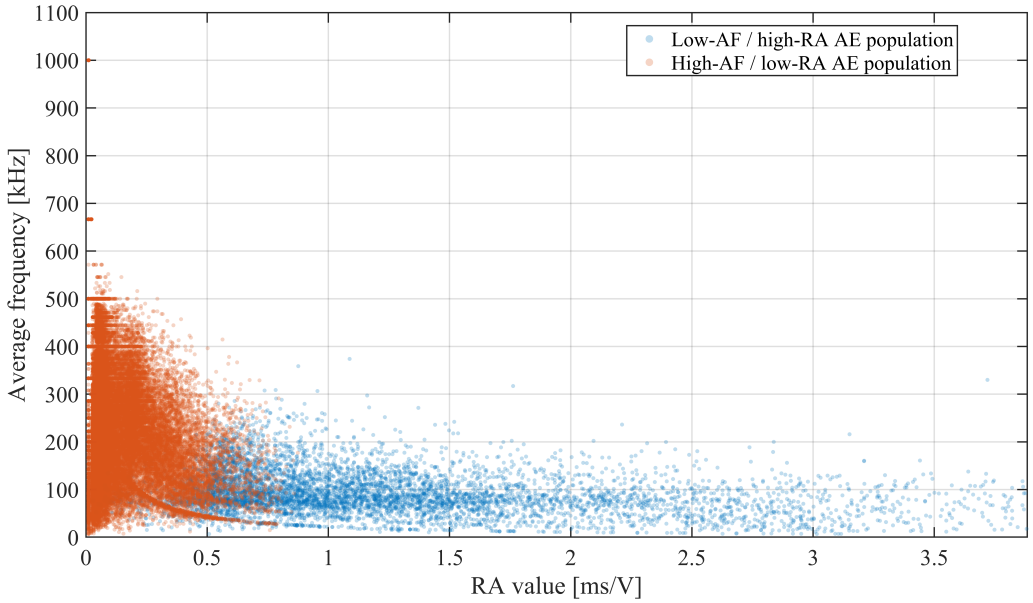

Figure 4.31 Global RA vs. average frequency distribution of the selected AE populations.

The energy-based cluster distribution in Figure 4.32 should be interpreted together with the centroid characteristics in Table 4.2. Although the high-AF / low-RA population represents a short-rise-time and high-frequency AE population, its centroid energy is much lower than that of the low-AF / high-RA population. In contrast, the low-AF / high-RA population has a considerably higher centroid energy, higher counts, longer duration, and higher amplitude. Therefore, when this population dominates the energy distribution, the AE response is not merely characterized by frequent acoustic hits; it is governed by events that carry a larger portion of the released acoustic energy.

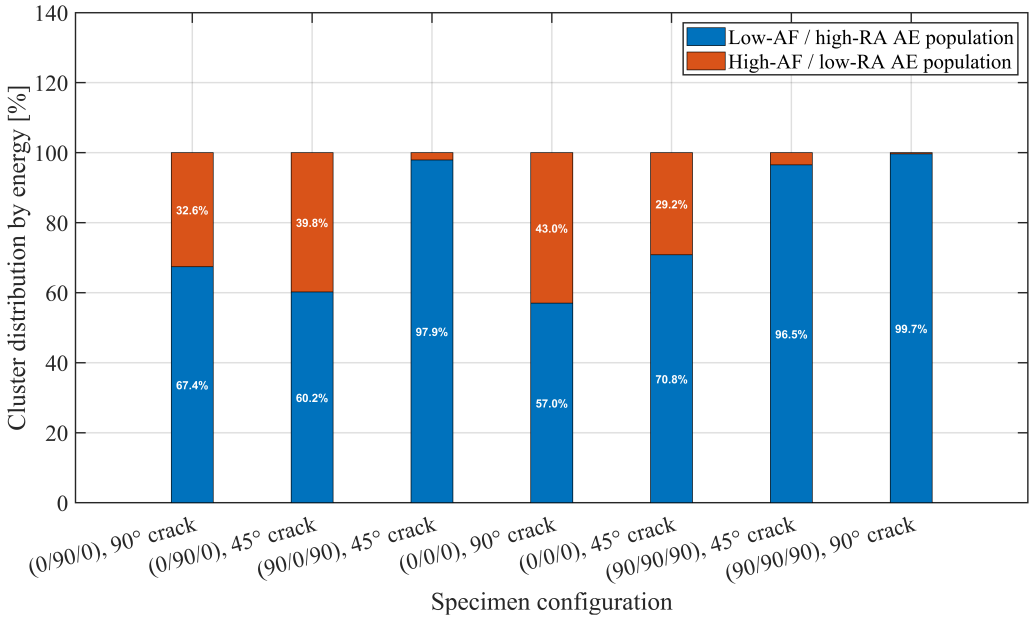

Figure 4.32 Energy-based distribution of the selected AE populations across the cracked laminate configurations.

This distinction is particularly clear for the (90/0/90) laminate with a 45° crack and the two (90/90/90) configurations, where the total AE energy is almost entirely carried by the low-AF / high-RA population. This suggests that, in these configurations, the dominant acoustic response is controlled by high-energy event populations rather than by a balanced contribution from both clusters. Such a response is consistent with a more abrupt or concentrated release of acoustic energy during advanced crack growth.

In contrast, the (0/90/0) and (0/0/0) configurations show a more mixed energy contribution between the two AE populations. This indicates that their crack propagation response involves both the high-energy low-AF / high-RA population and the high-AF / low-RA population. In other words, these specimens do not exhibit a purely single-population AE energy response; instead, the energy release is distributed between event populations with different waveform and frequency characteristics. This agrees with the specimen-wise AE-DIC observations, where early activity is associated with frequent acoustic events and visible crack-near localization, while later intervals are associated with stronger energy release and more developed DIC localization paths.

Overall, the energy-based cluster distribution shows that the laminate sequence and crack orientation affect not only the timing of AE activity, but also the type of AE population that carries the dominant acoustic energy. The clustering results therefore provide a population-level interpretation of specimen-wise observations:

progressive crack localization may begin with frequent lower-energy activity, whereas advanced crack propagation is increasingly governed by energetic AE populations with lower frequency content, higher RA, longer duration, and higher counts.

4.2.5 Temporal Evolution of Cluster-Wise Cumulative Energy

After identifying the two AE populations in Section 4.2.4.1, their temporal contribution is examined through cluster-wise cumulative energy curves to determine whether each population evolves gradually or becomes dominant through sudden high-energy releases. This time-resolved analysis complements the energy-based cluster distribution and helps clarify the role of each AE population during crack propagation. Representative DIC-based γ_{xy} fields are also evaluated at selected times corresponding to the main AE activity intervals of each specimen, allowing the temporal AE response to be linked with the spatial development of shear-coupled crack localization.

4.2.5.1 (0/90/0) Laminate with a 90º Initial Crack Specimen

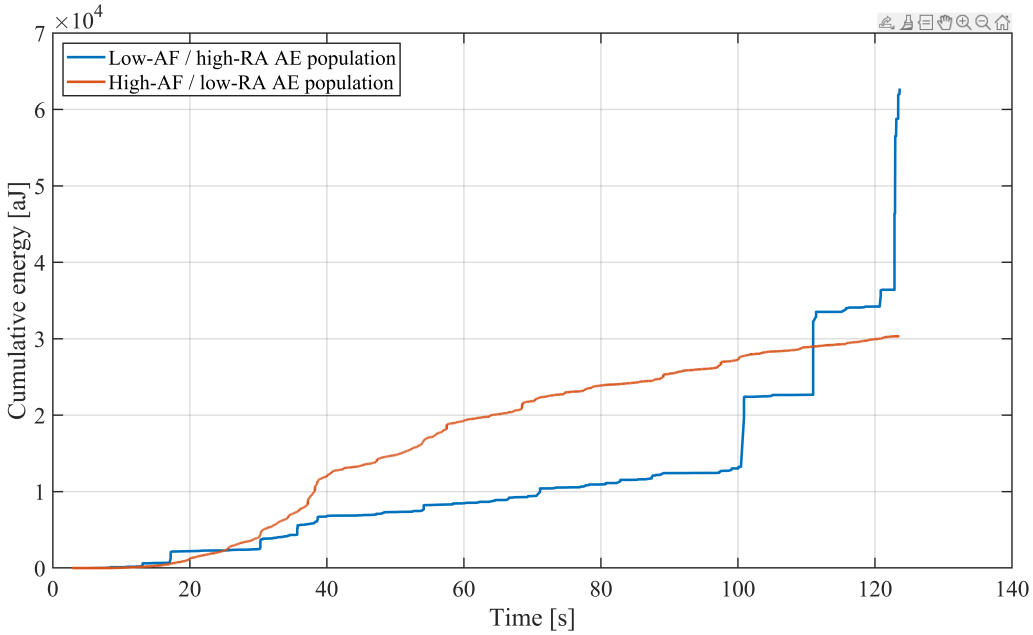

Figure 4.33 Cluster-wise cumulative AE energy evolution for the (0/90/0) laminate with a 90º initial crack.

For the (0/90/0) laminate with a 90º initial crack, the energy-based cluster distribution in Figure 4.32 shows that the low-AF / high-RA population accounts for 67.4% of the total AE energy, while the high-AF / low-RA population contributes 32.6%. This indicates that the overall acoustic response is dominated by the more energetic low-AF / high-RA population. However, the cluster-wise cumulative energy curves in Figure 4.33 show that this dominance does not develop uniformly throughout the test. The high-AF / low-RA population increases gradually during the early and intermediate loading stages, whereas the low-AF / high-RA population becomes dominant through abrupt energy releases after approximately t = 100 s and near the final loading interval.

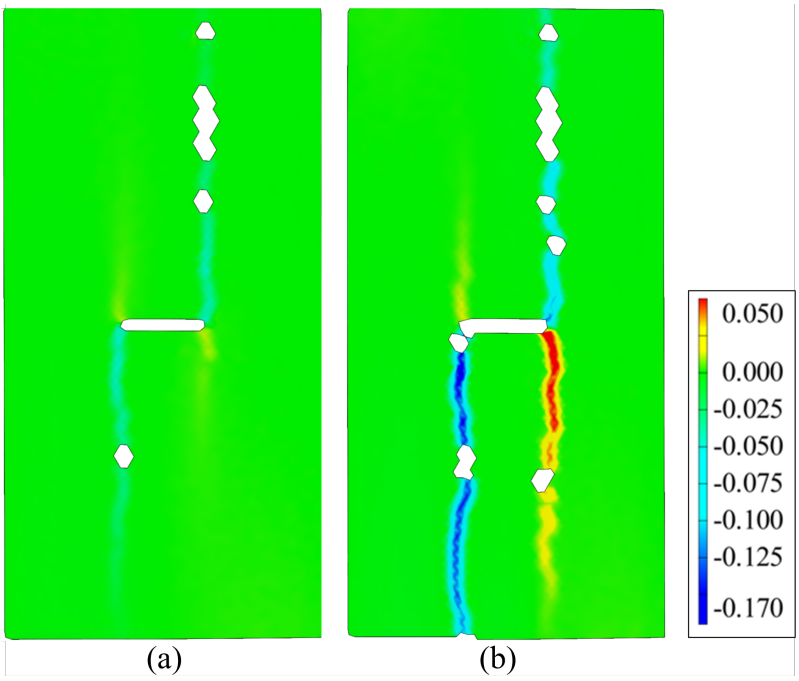

Figure 4.34 DIC-based γ_{xy} fields for the (0/90/0) laminate with a 90º initial crack: (a) t = 40 s and (b) t = 100 s.

The gradual increase of the high-AF / low-RA population in Figure 4.33 is consistent with rapid-rise acoustic activity associated with early tensile-dominated crack-tip processes, such as matrix cracking, local crack opening, and fiber/matrix debonding around the pre-cracked region. This interpretation is supported by the DIC-based γ_{xy} field at t = 40 s in Figure 4.34(a), where localized shear-strain concentration is already visible around the crack-tip region. Although the localization is still limited at this stage, its position around the crack path indicates that the early damage process involves local crack-near strain redistribution rather than a purely uniform tensile response.

After approximately t = 100 s, the abrupt increase of the low-AF / high-RA cu-

mulative energy in Figure 4.33 marks the transition to a more severe damage stage. In light of the global AE characteristics identified in Section 4.2.4.1, this later response is associated with higher-energy damage mechanisms involving mixed-mode crack propagation, delamination-related deformation, crack-face friction, sliding, and fiber-dominated damage contributions. The corresponding DIC field in Figure 4.34(b) provides the spatial counterpart of this transition. Compared with Figure 4.34(a), the γ_{xy} localization at t = 100 s becomes more developed and more continuous along the crack-propagation path, confirming that the later AE energy release is accompanied by stronger shear-coupled deformation around the propagated crack branches.

Therefore, Figures 4.32, 4.33, and 4.34 provide complementary evidence for the same damage-evolution sequence. Figure 4.32 identifies the low-AF / high-RA population as the dominant energy carrier for this specimen; Figure 4.33 shows that this dominance emerges mainly during the later high-energy propagation intervals; and Figure 4.34 demonstrates that this temporal transition is accompanied by the spatial development of shear localization around the crack path. Together, these results indicate that the (0/90/0) laminate with a 90º initial crack initially undergoes tensile-dominated crack-tip damage and then progressively shifts toward a more energetic mixed-mode crack-propagation stage involving shear interaction, delamination, frictional sliding, and fiber-related failure contributions.

4.2.5.2 (0/90/0) Laminate with a 45º Initial Crack Specimen

For the (0/90/0) laminate with a 45º initial crack, the energy-based cluster distribution in Figure 4.32 shows that the low-AF / high-RA population accounts for 60.2% of the total AE energy, while the high-AF / low-RA population contributes 39.8%. Compared with the 90º crack case of the same laminate family, this distribution indicates a more balanced contribution of the two AE populations, suggesting that the damage process involves both rapid tensile crack-tip activity and more energetic shear-related mechanisms. The cluster-wise cumulative energy response in Figure 4.35 further shows that the low-AF / high-RA population exhibits an early energy jump around t = 18 s and continues to increase through stepwise releases, whereas the high-AF / low-RA population grows more progressively throughout the test. This temporal pattern indicates that the inclined crack promotes mixed-mode damage evolution from the early stage of loading rather than producing a purely tensile-dominated crack-opening response.

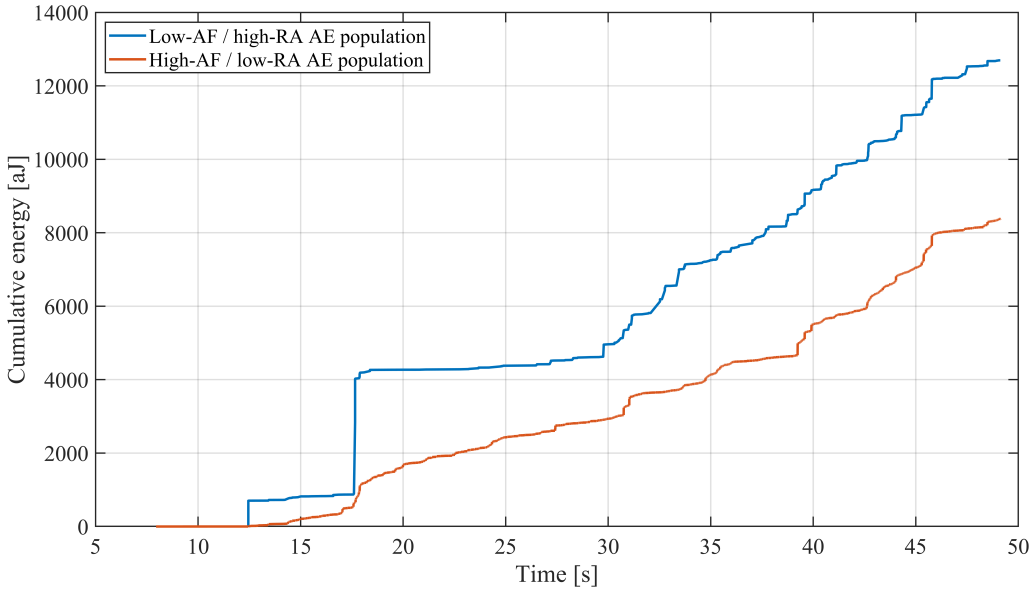

Figure 4.35 Cluster-wise cumulative AE energy evolution for the (0/90/0) laminate with a 45º initial crack.

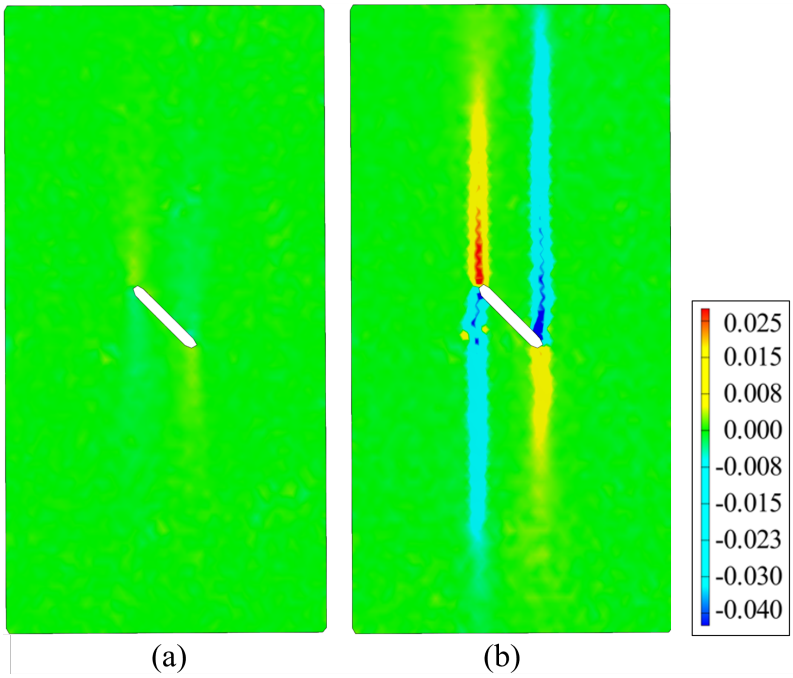

Figure 4.36 DIC-based γ_{xy} fields for the (0/90/0) laminate with a 45º initial crack: (a) t = 18 s and (b) t = 46 s.

The DIC-based γ_{xy} field at t = 18 s in Figure 4.36(a) supports this interpretation by showing the initial formation of shear-strain localization around the inclined crack region. Although the localization is still limited, its alignment with the crack path indicates that shear-coupled deformation is already active during the early AE energy development. At t = 46 s, Figure 4.36(b) shows a much more pronounced γ_{xy}

localization pattern, with opposite-sign shear bands developing along the propagated crack path. This spatial evolution is consistent with the continued increase of both AE populations in Figure 4.35: the high-AF / low-RA activity reflects repeated rapid crack-tip events, while the low-AF / high-RA contribution represents the more energetic component associated with mixed-mode crack propagation, crack-face sliding, frictional interaction, and delamination-related deformation.

Therefore, the combined AE-DIC evidence indicates that the (0/90/0) laminate with a 45º initial crack does not follow a simple tensile-opening dominated damage sequence. Instead, the inclined crack geometry activates shear-coupled deformation from the early stage, as confirmed by the γ_{xy} localization at t = 18 s, and this response becomes more spatially developed by t = 46 s. The relatively balanced energy contribution of the two AE populations in Figure 4.32, together with their simultaneous temporal development in Figure 4.35, suggests that tensile crack-tip processes and mixed-mode shear-driven mechanisms evolve together during crack propagation in this specimen.

4.2.5.3 (90/0/90) Laminate with a 45º Initial Crack Specimen

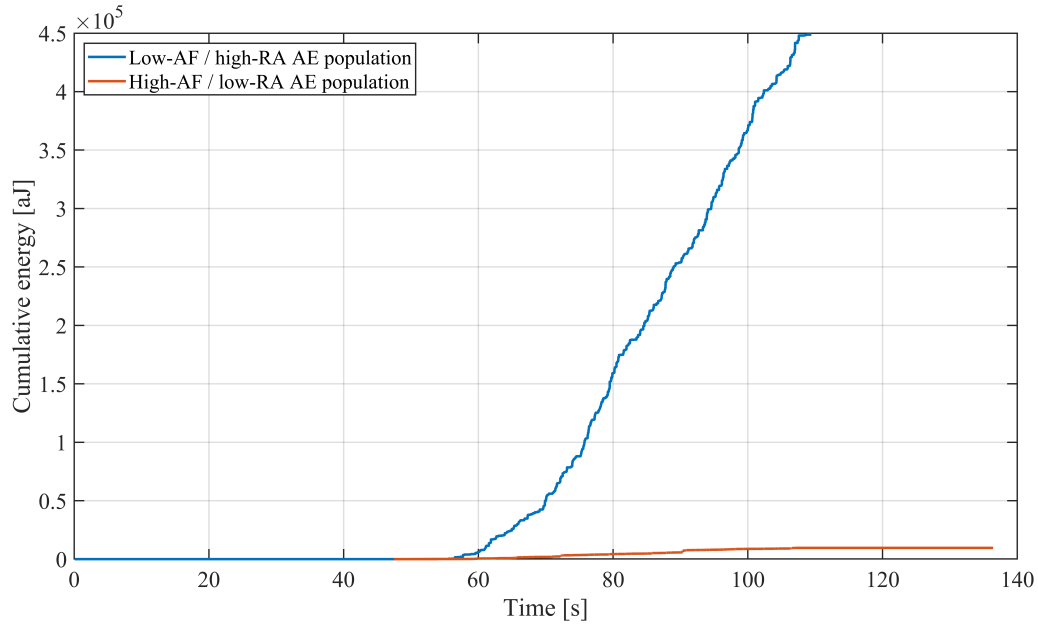

Figure 4.37 Cluster-wise cumulative AE energy evolution for the (90/0/90) laminate with a 45º initial crack.

For the (90/0/90) laminate with a 45º initial crack, the energy-based cluster distribution in Figure 4.32 shows a strong dominance of the low-AF / high-RA AE

population, which accounts for 97.9% of the total AE energy. This indicates that the acoustic response of this specimen is governed almost entirely by the more energetic AE population, while the high-AF / low-RA population contributes only marginally. The cluster-wise cumulative energy evolution in Figure 4.37 confirms this behavior, since the low-AF / high-RA population starts to increase rapidly after approximately t = 60 s and continues to accumulate energy until the final loading stage. In contrast, the high-AF / low-RA population remains nearly inactive over the same interval. This response suggests that the damage evolution is not dominated by repeated low-energy tensile crack-tip events, but by a progressive high-energy damage process associated with mixed-mode crack propagation and delamination-related mechanisms.

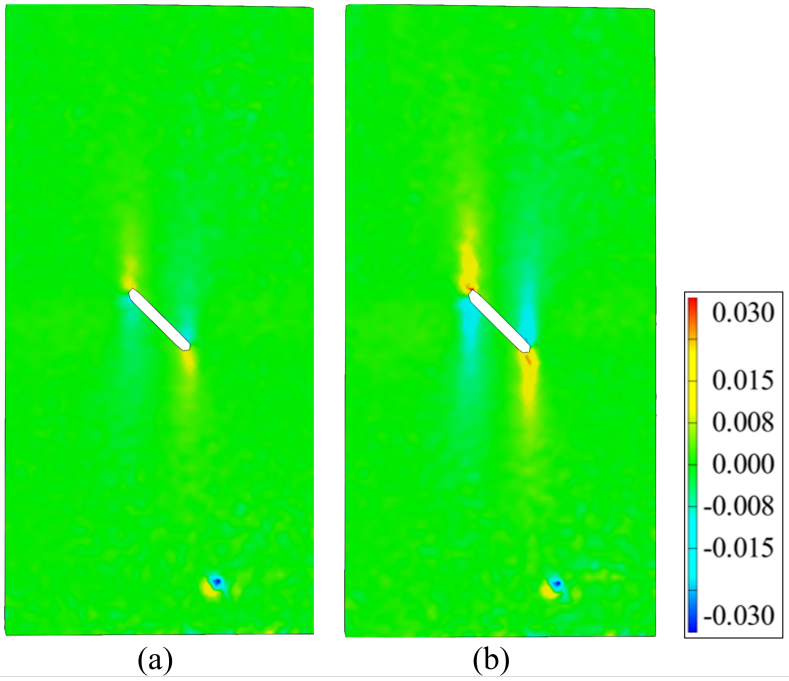

Figure 4.38 DIC-based γ_{xy} fields for the (90/0/90) laminate with a 45° initial crack: (a) t = 60 s and (b) t = 100 s.

The DIC-based γ_{xy} fields provide the spatial counterpart of this AE response. At t = 60 s, Figure 4.38(a) already shows localized shear-strain concentration around the inclined crack-tip region, indicating the onset of shear-coupled deformation along the potential crack path. At t = 100 s, Figure 4.38(b) shows that this localization becomes more developed around the crack region, with a clearer γ_{xy} concentration extending from the inclined crack. This evolution is consistent with the rapid growth of the low-AF / high-RA cumulative energy in Figure 4.37. The correspondence between the dominant energetic AE population and the development of γ_{xy} localization indicates that the crack-growth process involves strong mixed-mode

deformation, crack-face interaction, delamination-related strain redistribution, and fiber-related damage contributions.

Therefore, the combined AE-DIC evidence indicates that the (90/0/90) laminate with a 45º initial crack is controlled by a high-energy damage mode from the main crack-propagation stage onward. The energy distribution in Figure 4.32 identifies the low-AF / high-RA population as the dominant acoustic source, the cumulative energy curve in Figure 4.37 shows that this dominance develops rapidly after the onset of major AE activity, and the γ_{xy} fields in Figure 4.38 demonstrate the accompanying spatial development of shear-coupled localization around the inclined crack. This confirms that the damage process in this specimen is mainly governed by mixed-mode propagation and delamination-related deformation rather than by a gradual tensile-opening dominated sequence.

4.2.5.4 (0/0/0) Laminate with a 90º Initial Crack Specimen

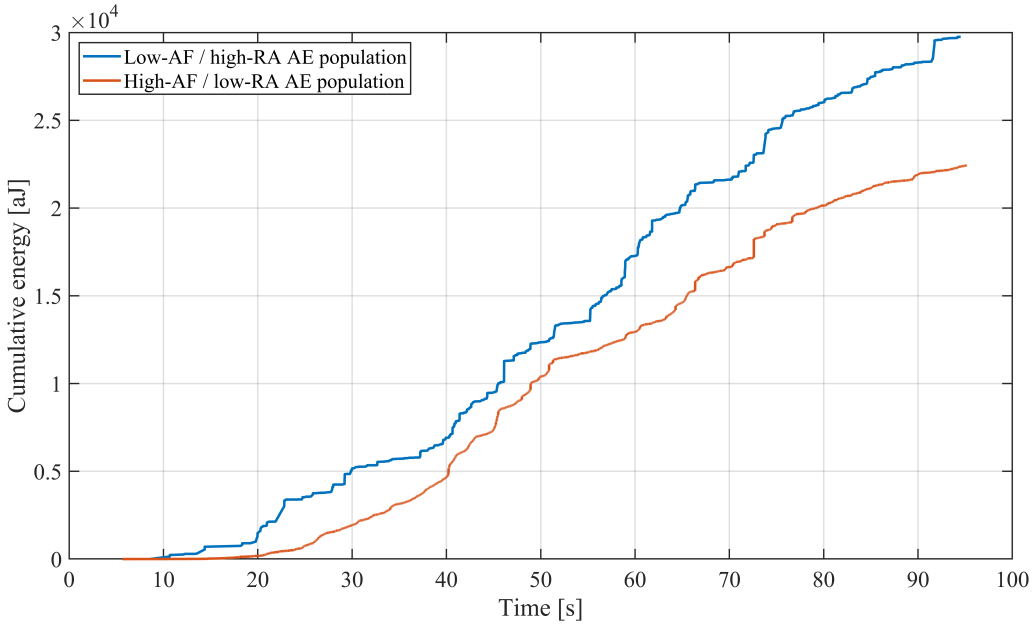

Figure 4.39 Cluster-wise cumulative AE energy evolution for the (0/0/0) laminate with a 90º initial crack.

For the (0/0/0) laminate with a 90º initial crack, the energy-based cluster distribution in Figure 4.32 shows that the low-AF / high-RA population accounts for 57.0% of the total AE energy, while the high-AF / low-RA population contributes 43.0%. This relatively balanced distribution indicates that the damage process is not governed by a single acoustic population, but involves both rapid crack-tip events and

more energetic damage mechanisms. The cluster-wise cumulative energy curves in Figure 4.39 support this interpretation, as both AE populations increase throughout the test, particularly after approximately t = 40 s. The high-AF / low-RA population grows progressively, reflecting repeated tensile-dominated crack-tip activity, whereas the low-AF / high-RA population shows stepwise energy increases associated with more severe crack-growth events.

The DIC-based γ_{xy} fields provide the spatial counterpart of this coupled AE response. At t = 43 s, Figure 4.40(a) already shows a clear shear-localization band developing around the initial crack region, indicating that local shear-coupled strain redistribution is active during the early crack-growth stage. This agrees with the simultaneous increase of both AE populations in Figure 4.39 and suggests that tensile crack opening is accompanied by local shear deformation around the crack path. At t = 65 s, Figure 4.40(b) shows a more developed γ_{xy} pattern, with stronger and more continuous opposite-sign shear bands extending from the crack region. This evolution indicates the intensification of mixed-mode deformation and is consistent with the continued accumulation of the low-AF / high-RA energy contribution.

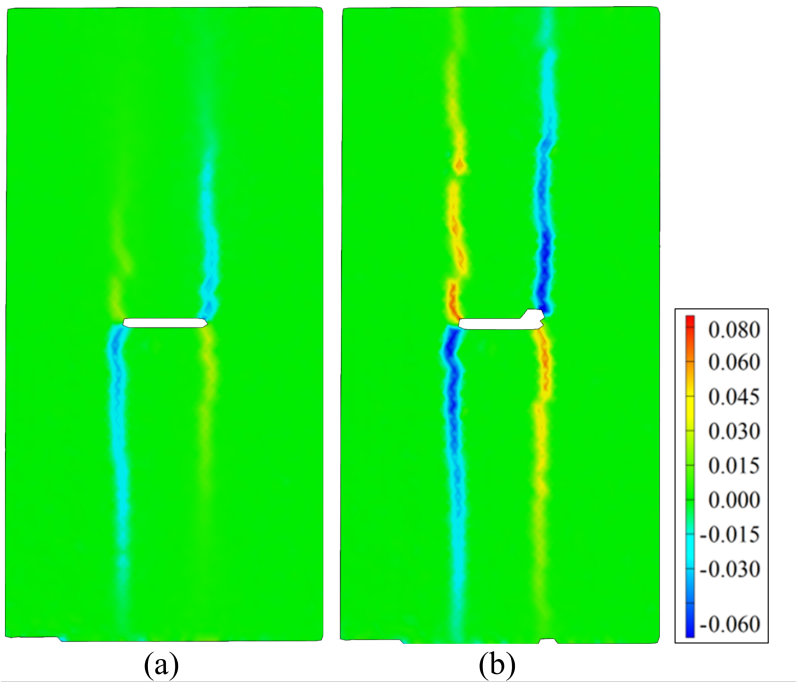

Figure 4.40 DIC-based γ_{xy} fields for the (0/0/0) laminate with a 90º initial crack: (a) t = 43 s and (b) t = 65 s.

Therefore, the combined AE-DIC response indicates that the (0/0/0) laminate with a 90º initial crack undergoes a coupled damage process in which tensile crack-tip activity and shear-related crack propagation evolve together. The balanced energy contribution in Figure 4.32 highlights the relevance of both AE populations, while

the temporal curves in Figure 4.39 show that their contributions develop over the same main damage interval. The γ_{xy} fields in Figure 4.40 confirm that this acoustic activity corresponds spatially to the development of shear-coupled localization around the crack path. This suggests that crack propagation in this specimen involves local crack opening together with mixed-mode shear interaction, crack-face sliding, frictional effects, and progressive fiber-related damage.

4.2.5.5 (0/0/0) Laminate with a 45º Initial Crack Specimen

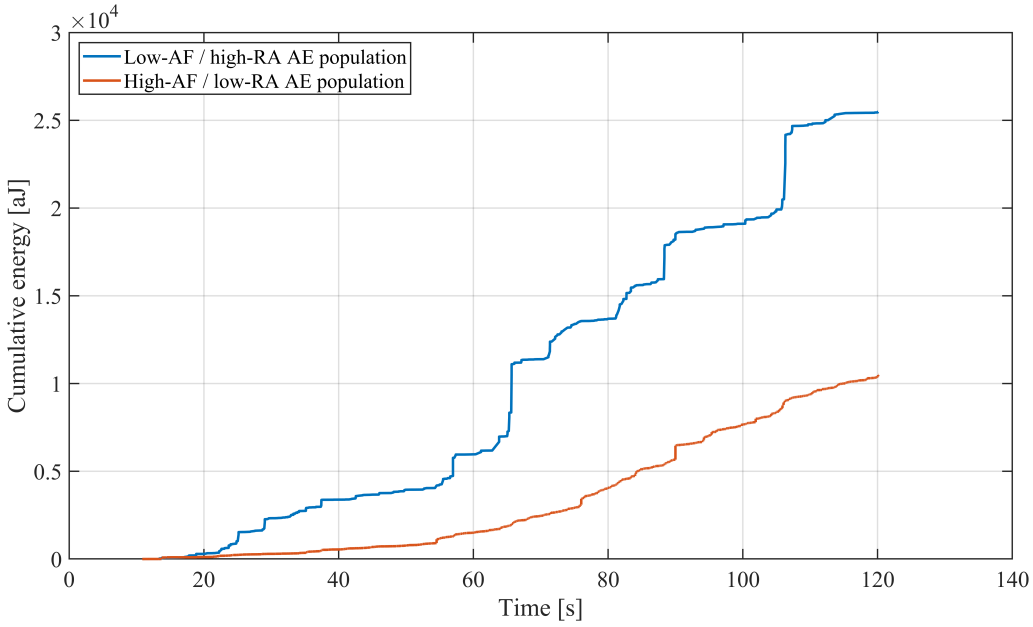

Figure 4.41 Cluster-wise cumulative AE energy evolution for the (0/0/0) laminate with a 45º initial crack.

For the (0/0/0) laminate with a 45º initial crack, the energy-based cluster distribution in Figure 4.32 shows that the low-AF / high-RA population accounts for 70.8% of the total AE energy, whereas the high-AF / low-RA population contributes 29.2%. This distribution indicates that the acoustic response is mainly governed by the low-AF / high-RA population, although the high-AF / low-RA population still provides a measurable contribution associated with rapid crack-tip events. The cluster-wise cumulative energy curves in Figure 4.41 show that the low-AF / high-RA population develops through distinct stepwise increases, particularly during the main crack-growth intervals, while the high-AF / low-RA population evolves more gradually. This behavior suggests that the inclined crack does not produce a purely tensile-opening response; instead, the damage process is mainly associated with mixed-mode

crack propagation accompanied by intermittent high-energy AE releases.

The DIC-based γ_{xy} fields in Figure 4.42 provide direct spatial support for this interpretation. At t = 65 s, Figure 4.42(a) shows the initial development of localized shear strain around the inclined crack, indicating that shear-coupled deformation is already active during the early crack-growth stage. This agrees with the onset of cumulative AE energy increase in Figure 4.41 and suggests that local crack opening is accompanied by shear redistribution around the crack tip. At t = 106 s, Figure 4.42(b) shows a more pronounced γ_{xy} localization pattern around the propagated crack region, with stronger positive and negative shear concentrations near the crack path. The presence of these opposite-sign shear regions indicates relative sliding and local shear interaction around the crack faces, which is consistent with mixed-mode crack propagation, frictional interaction, delamination-related deformation, and fiber-related damage contributions.

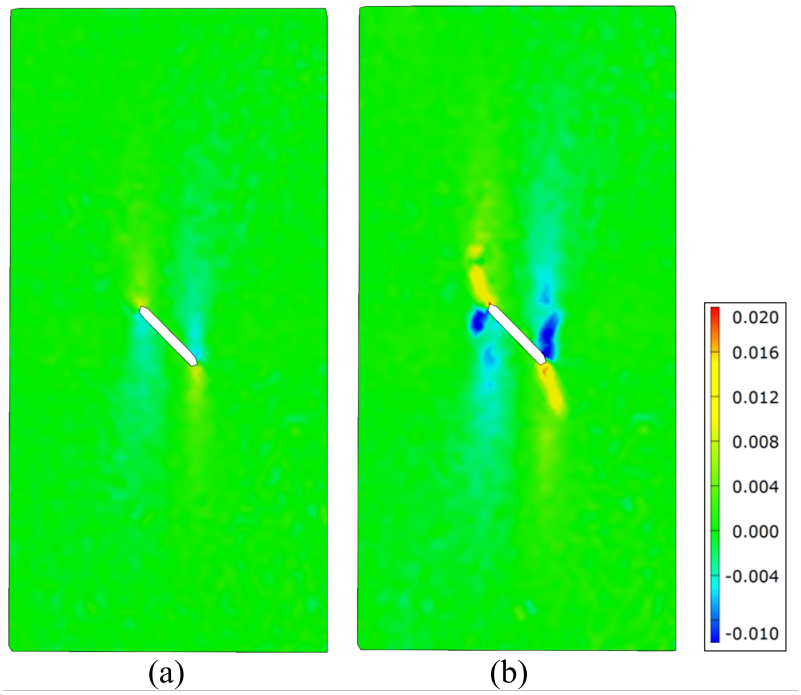

Figure 4.42 DIC-based γ_{xy} fields for the (0/0/0) laminate with a 45º initial crack: (a) t = 65 s and (b) t = 106 s.

Therefore, the combined AE-DIC evidence indicates that the (0/0/0) laminate with a 45º initial crack undergoes a damage process strongly influenced by shear-coupled crack growth. The energy distribution in Figure 4.32 identifies the low-AF / high-RA population as the dominant energy carrier, while the cumulative energy response in Figure 4.41 shows that this dominance develops through stepwise high-energy releases. The γ_{xy} fields in Figure 4.42 confirm that these acoustic events

correspond spatially to the development of localized shear deformation around the inclined crack path. This combined response supports the interpretation that the specimen evolves from early crack-tip activity toward mixed-mode crack propagation involving crack-face sliding, delamination-related deformation, and progressive fiber-dominated damage.

4.2.5.6 (90/90/90) Laminate with a 45º Initial Crack Specimen

For the (90/90/90) laminate with a 45º initial crack, the energy-based cluster distribution in Figure 4.32 indicates that the AE response is overwhelmingly controlled by the low-AF / high-RA population, which accounts for 96.5% of the total AE energy. This strong dominance is not the result of a gradual accumulation over the entire loading history. Instead, the cluster-wise cumulative energy response in Figure 4.43 reveals that most of the energy associated with this population is released suddenly at approximately t = 13 s, after which only minor additional increases are observed. This behavior points to a rapid fracture-controlled damage process rather than a progressive sequence of distributed crack-tip events.

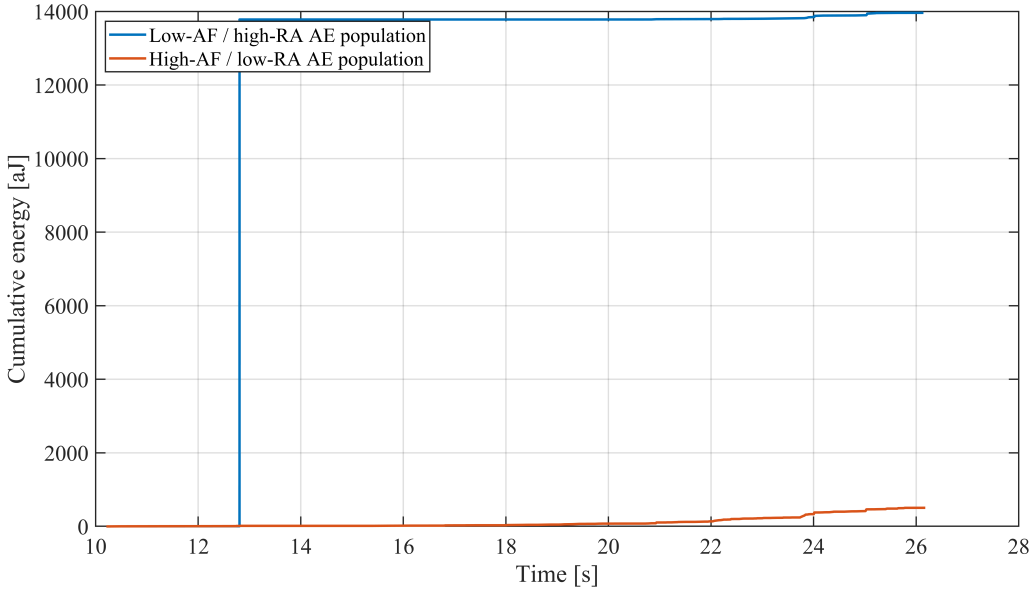

Figure 4.43 Cluster-wise cumulative AE energy evolution for the (90/90/90) laminate with a 45º initial crack.

The DIC-based γ_{xy} fields provide the full-field counterpart of this abrupt acoustic response. At t = 14.8 s, Figure 4.44(a) shows only weak and scattered shear-strain localization around the inclined crack, indicating that the deformation field has

not yet developed into a distinct crack-propagation pattern. A markedly different response is observed at t = 14.9 s, where Figure 4.44(b) shows the sudden formation of a localized γ_{xy} band extending from the crack region. The emergence of this shear-localized path within two consecutive DIC times demonstrates that the dominant AE energy release is accompanied by a rapid spatial reorganization of the strain field.

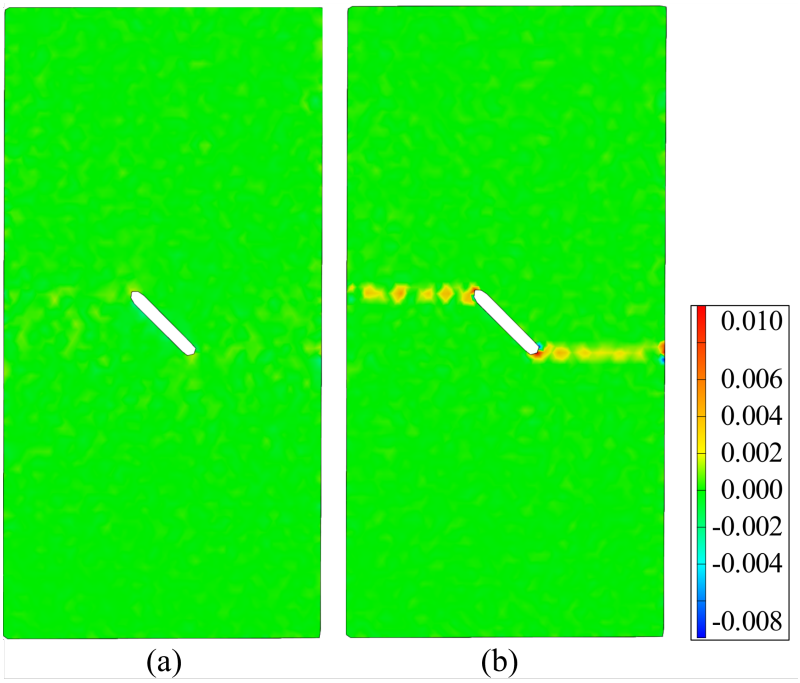

Figure 4.44 DIC-based γ_{xy} fields for the (90/90/90) laminate with a 45^{o} initial crack: (a) t = 14.8 s and (b) t = 14.9 s.

This direct temporal and spatial correspondence suggests that the main damage event in this specimen is governed by unstable mixed-mode crack propagation. The low-AF / high-RA dominance reflects a high-energy acoustic response associated with shear-related and longer-duration damage mechanisms, while the sudden γ_{xy} localization confirms that the fracture process involves strong shear-coupled deformation around the crack path. Therefore, the combined AE-DIC evidence supports the interpretation that the damage mechanism is associated with rapid crack-face interaction, delamination-related deformation, frictional sliding, and fiber-related fracture contributions, rather than with a gradual tensile-opening dominated crack-growth sequence.

4.2.5.7 (90/90/90) Laminate with a 90º Initial Crack Specimen

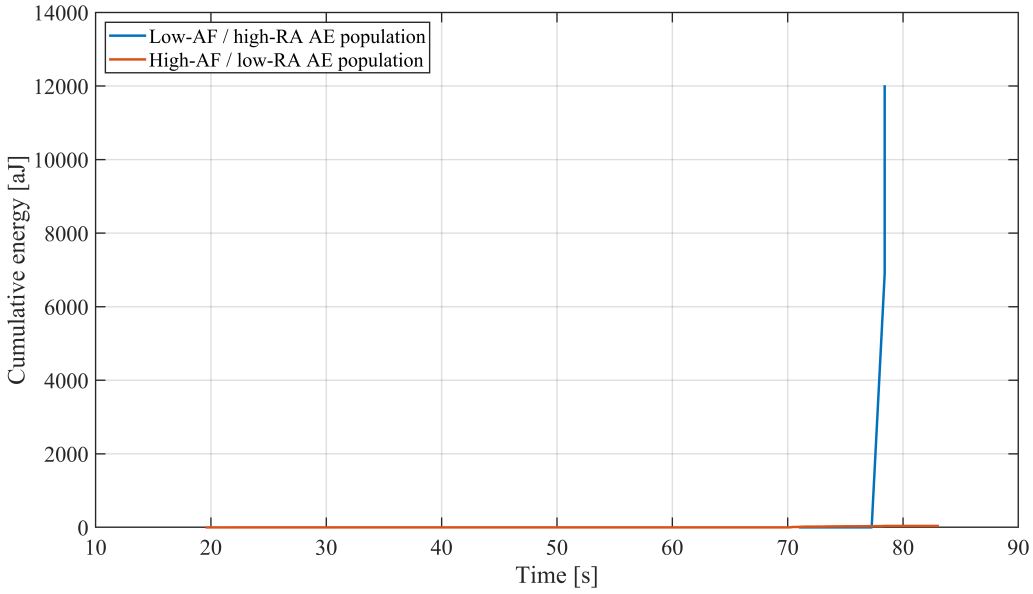

Figure 4.45 Cluster-wise cumulative AE energy evolution for the (90/90/90) laminate with a 90º initial crack.

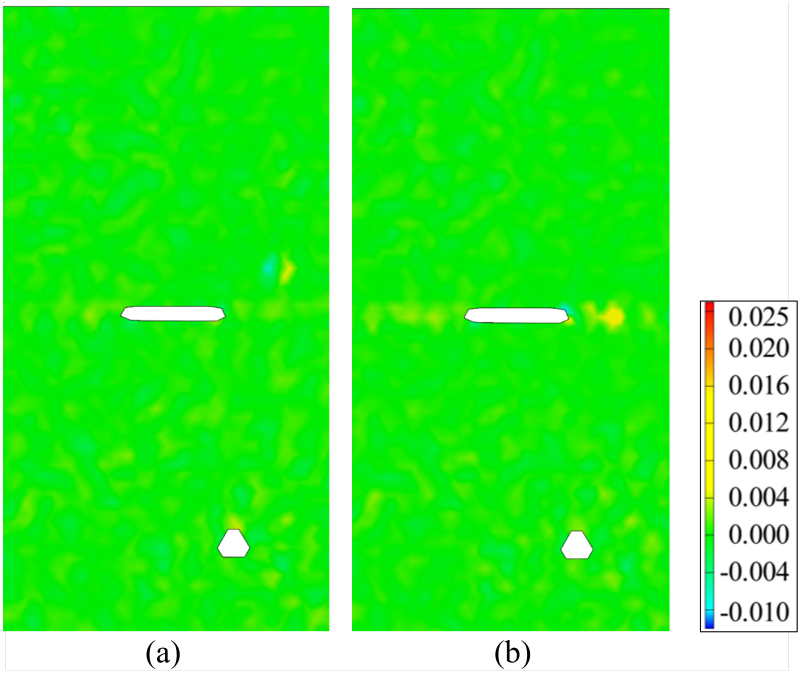

Figure 4.46 DIC-based γ_{xy} fields for the (90/90/90) laminate with a 90º initial crack: (a) t = 77.2 s and (b) t = 77.4 s.

For the (90/90/90) laminate with a 90º initial crack, the energy-based cluster distribution in Figure 4.32 indicates an almost complete dominance of the low-AF / high-RA population, which accounts for 99.7% of the total AE energy. Unlike the

specimens showing gradual or stepwise energy accumulation over a wider loading interval, the cluster-wise cumulative energy response in Figure 4.45 remains nearly inactive until the final stage of the test and then exhibits a sharp energy jump at approximately t = 78 s. This delayed and abrupt release indicates that the main acoustic activity is associated with a sudden fracture event rather than progressive crack-tip damage accumulation throughout the loading history.

The DIC-based γ_{xy} fields in Figure 4.46 provide the corresponding full-field evidence for this final transition. At t = 77.2 s, Figure 4.46(a) shows only weak shear-strain localization around the pre-cracked region, suggesting that the crack-related deformation is still limited immediately before the final event. By t = 77.4 s, Figure 4.46(b) reveals the rapid development of a localized γ_{xy} band along the horizontal crack path. The emergence of this shear-coupled localization over a very short time interval is consistent with the sudden low-AF / high-RA energy release in Figure 4.45 and indicates that the final fracture is accompanied by localized shear redistribution around the crack faces.

Taken together, the AE and DIC results show that the (90/90/90) laminate with a 90^{o} initial crack is governed by a delayed but unstable fracture process. The near-exclusive low-AF / high-RA energy contribution reflects a high-energy damage event, while the rapid formation of γ_{xy} localization demonstrates the spatial development of shear-coupled deformation during final crack propagation. This response is consistent with a fracture process involving mixed-mode crack growth, crack-face interaction, delamination-related deformation, frictional sliding, and fiber-related failure contributions, rather than a gradual tensile-opening dominated damage sequence.

4.2.6 Cross-Specimen Interpretation of Cluster-Wise AE-DIC Response

The specimen-wise results presented in Section 4.2.5 show that the cluster-wise AE response is strongly affected by both laminate sequence and initial crack orientation. Although the same two AE populations are used for all specimens, their relative energy contribution and temporal evolution differ considerably from one configuration to another. This confirms that the clusters should not be interpreted as fixed damage modes. Instead, they provide a comparative acoustic signature that reflects how crack-tip activity, mixed-mode deformation, crack-face interaction, delamination-related strain redistribution, and fiber-related damage contribute

to the overall crack-propagation process under different laminate and crack configurations.

For the two (0/90/0) specimens, the effect of initial crack orientation is clearly observed. In the 90º crack case, the low-AF / high-RA population is dominant in terms of total energy, but this dominance becomes more pronounced mainly during the later high-energy propagation intervals. The early and intermediate stages still include a gradual contribution from the high-AF / low-RA population, suggesting that the crack initially develops through rapid crack-tip activity before transitioning toward a more energetic mixed-mode propagation stage. In contrast, the 45º crack case shows a more balanced contribution between the two AE populations. The inclined crack activates shear-coupled deformation from the early stage, as supported by the γ_{xy} localization around the crack path. Therefore, even within the same laminate family, the 90º crack configuration follows a more staged transition from crack-tip activity to mixed-mode propagation, whereas the 45º crack configuration promotes simultaneous tensile crack-tip activity and shear-related deformation from earlier loading stages.

The comparison between the (0/90/0) and (90/0/90) laminates with the same 45º initial crack further highlights the influence of stacking sequence. Although both specimens contain the same ply orientations, the reversal of the laminate sequence changes the relative dominance of the AE populations. The (0/90/0) laminate with a 45º crack exhibits a relatively balanced acoustic response, indicating that both rapid crack-tip events and more energetic mixed-mode mechanisms contribute to the damage process. However, the (90/0/90) laminate with a 45º crack is governed almost entirely by the low-AF / high-RA population. This indicates that the acoustic energy release in this specimen is mainly carried by longer-duration, higher-energy events associated with shear-coupled propagation and delamination-related deformation. The corresponding γ_{xy} fields also show that the crack-related localization develops more strongly as a shear-dominated path after the onset of major AE activity. Therefore, the ply sequence does not only affect the observed localization direction, but also changes whether the crack-propagation process is acoustically balanced or dominated by a single energetic event population.

A similar crack-orientation effect is observed in the (0/0/0) laminate family. For the 90º initial crack, the energy contribution of the two AE populations is relatively balanced, indicating a coupled damage process in which tensile crack-tip activity and shear-related crack propagation evolve together. The γ_{xy} fields confirm that shear localization develops around the crack region even though the initial crack is perpendicular to the loading direction. This suggests that local crack opening is ac-

companied by shear redistribution and mixed-mode interaction during propagation. When the crack is inclined at 45º, the low-AF / high-RA population becomes more dominant and develops through stepwise high-energy releases. The corresponding γ_{xy} fields show stronger opposite-sign shear concentrations around the inclined crack path. Therefore, in the (0/0/0) laminates, changing the crack orientation from 90º to 45º shifts the response from a relatively balanced tensile-shear interaction toward a more shear-coupled and intermittently energetic crack-growth process.

The (90/90/90) laminates show a different behavior compared with the 0º-dominated configurations. For both the 45º and 90º initial cracks, the AE energy is almost completely governed by the low-AF / high-RA population. This indicates that the crack-propagation process is not characterized by a long sequence of gradually accumulating high-AF / low-RA crack-tip events. Instead, the dominant acoustic response is associated with abrupt or highly concentrated high-energy releases. However, the timing of this response depends on the initial crack orientation. In the 45º crack case, the main acoustic energy release occurs very early and is accompanied by the rapid formation of a localized γ_{xy} band. In the 90º crack case, the specimen remains comparatively quiet until the final stage, where a sudden energy jump coincides with the rapid development of shear-coupled localization along the horizontal crack path. Thus, the 90/90/90 family is consistently dominated by an energetic AE population, but the inclined crack triggers an earlier unstable mixed-mode response, whereas the 90º crack produces a delayed fracture-dominated transition.

Considering all specimens together, three characteristic crack-propagation behaviors can be distinguished. The first is a progressive and coupled response, observed most clearly in the (0/90/0) and (0/0/0) specimens where both AE populations contribute meaningfully and the DIC-based γ_{xy} localization develops gradually or stepwise. The second is a delayed but energetically dominated response, represented by the (90/0/90) laminate with a 45º crack, where the AE activity starts later but is then governed by the low-AF / high-RA population together with clear shear-coupled localization. The third is an abrupt fracture-dominated response, observed in the (90/90/90) specimens, where the main acoustic energy release is concentrated within a short time interval and coincides with the sudden formation of a localized γ_{xy} band.

These cross-specimen comparisons demonstrate that crack propagation in pre-cracked composite laminates cannot be interpreted only from the initial crack orientation or only from the laminate sequence. The same crack angle may lead to different AE population dominance depending on the stacking sequence, while the same laminate family may exhibit different temporal and spatial damage evolution when

the crack orientation changes. The integrated cluster-wise AE and DIC-based γ_{xy} interpretation therefore provides a more complete basis for distinguishing progressive crack growth, delayed high-energy propagation, and abrupt fracture-dominated localization. This reinforces the main objective of the multi-instrument framework: AE identifies when and how strongly acoustic damage activity evolves, while DIC shows whether this activity corresponds to spatially developing shear-coupled crack localization.

5. CONCLUSION

5. CONCLUSION

This thesis investigated damage localization and crack propagation monitoring in pre-cracked carbon/epoxy composite laminates by integrating full-field optical measurements, numerical post-processing, acoustic emission monitoring, and local strain measurements. The work was built around two complementary contributions. The first contribution focused on improving the numerical reliability of DIC-based crack-sensitive localization by developing a dual-stage smoothing element analysis assisted post-processing framework. The second contribution focused on improving the physical interpretation of crack propagation by combining DIC, AE, and strain gauge measurements within a stage-wise multi-instrument assessment strategy. Together, these two contributions provide a more complete basis for evaluating not only where damage localizes, but also when damage activity intensifies and how local mechanical strain redistribution accompanies crack growth.

In the first part of the thesis, a dual-stage SEA-assisted DIC framework was developed to address the numerical sensitivity of full-field crack localization. Since DIC directly measures displacement while strain and strain-gradient quantities are obtained through differentiation, the localization process is affected by two critical numerical transitions: the displacement-to-strain transition and the equivalent-strain-to-gradient transition. The proposed framework treated these transitions separately. In the first stage, the measured in-plane DIC displacement fields were regularized before strain reconstruction. In the second stage, the reconstructed von Mises equivalent strain field was smoothed before spatial-gradient evaluation. This staged strategy provided a controlled route from raw experimental displacement measurements to stable crack-sensitive localization maps.

Based on this regularized full-field response, a gradient-enhanced, thresholded, and nonlinearly normalized damage-sensitive localization index, D3, was formulated. The index was derived directly from experimental DIC measurements and did not require a constitutive damage law, finite element damage simulation, or material degradation parameters. This is an important outcome of the thesis because it shows that crack-sensitive localization can be evaluated using experimentally measured deformation fields without relying on assumed damage evolution models. The SEA-reconstructed displacement fields remained consistent with the original DIC measurements, while the reconstructed strain fields showed agreement with the available strain-gauge responses. Therefore, the proposed post-processing framework preserved the experimentally measured deformation behavior while improving the stability and interpretability of the localization analysis.

The D3-based localization results demonstrated that the evolution of crack-sensitive regions is strongly governed by the combined effect of laminate architecture and initial crack orientation. In the 0^{o}-dominated laminates, particularly the 0/90/0 and 0/0/0 configurations, the high-D3 regions generally developed from compact crack-tip zones into extended horizontal localization bands. This behavior indicates that longitudinal load transfer through the 0^{o} plies promotes progressive crack-related deformation along the loading direction. In contrast, the 90/90/90 laminates exhibited delayed and more abrupt localization. Since these specimens were dominated by matrix-controlled transverse loading, the crack-sensitive regions did not develop gradually during the earlier loading stages; instead, stronger localization appeared close to the final reliable stages and followed a more vertical or fracture-dominated pattern. The 90/0/90 laminate with a 45^{o} crack showed an intermediate response, reflecting the combined influence of the central 0^{o} ply and the outer 90^{o} plies.

The quantitative pre-failure localization assessment further supported the visual interpretation of the D3 maps. The high-index regions consistently formed near mechanically critical crack-tip zones, and their dominant orientations showed good agreement with the experimentally observed crack-propagation directions. This confirms that the D3 index is not only a qualitative contour visualization, but also a measurable indicator of crack-sensitive localization before final fracture. At the same time, the results showed that localization maps near the final fracture stage must be interpreted together with DIC data quality, especially when severe crack opening, paint detachment, or local decorrelation occurs. This observation highlights an important experimental limitation of surface-based optical measurements and reinforces the need for complementary measurement techniques.

In the second part of the thesis, the same cracked laminate configurations were

evaluated using an integrated multi-instrument framework combining DIC, AE, and strain gauges. This framework was developed because crack propagation in composite laminates cannot be fully understood using a single measurement technique. DIC provides spatial evidence of surface strain localization, but it cannot independently determine the timing or intensity of active damage events. AE provides temporal and energetic information about damage activity, but it cannot directly describe the spatial crack path. Strain gauges provide local mechanical confirmation, but only at selected measurement points. By combining these three forms of evidence, the proposed framework enabled a more physically consistent interpretation of crack propagation stages.

The global stress-strain results confirmed that both stacking sequence and initial crack orientation strongly influence the mechanical response of pre-cracked composite laminates. The 0^{o}-dominated configurations exhibited higher tensile resistance and more progressive damage development, while the 90^{o}-dominated configurations showed lower strength and more brittle, fracture-dominated behavior. The mixed-orientation laminates produced intermediate responses depending on the relative arrangement of the 0^{o} and 90^{o} plies. These global trends provided the mechanical background for interpreting the DIC, AE, and strain-gauge observations.

The DIC-based strain fields showed how crack-related deformation developed spatially around the initial crack and propagated through the specimen. The AE time-history indicators complemented this spatial information by identifying when acoustic damage activity initiated, accumulated, and intensified. In several specimens, increases in AE hit rate and count rate were associated with the early development of strain localization, while sharp increases in cumulative energy and energy rate corresponded to severe crack propagation or final fracture. The strain gauges, where available, provided additional local confirmation by capturing slope changes, unloading behavior, and abrupt strain redistribution during critical intervals. These results demonstrate that the convergence of DIC, AE, and strain-gauge evidence provides a stronger basis for identifying crack-growth stages than any individual measurement alone.

The AE clustering analysis identified two characteristic acoustic event populations across the specimens. The high-AF / low-RA population was associated with shorter rise times, higher frequency content, and lower centroid energy, while the low-AF / high-RA population was associated with higher energy, longer duration, higher counts, and larger amplitude. These populations were interpreted as acoustic event groups rather than directly assigned fixed damage modes, since AE features can be affected by source characteristics, wave propagation, attenuation, and sensor re-

sponse. This cautious interpretation is important because it avoids over-attributing AE clusters to specific microscopic damage mechanisms without independent physical validation.

The combined AE-DIC interpretation revealed three characteristic crack-propagation behaviors. The first behavior was a progressive and coupled response, observed most clearly in the 0/90/0 and 0/0/0 laminates, where both AE populations contributed and the DIC-based localization developed gradually or stepwise. The second behavior was a delayed but energetically dominated response, represented by the 90/0/90 laminate with a 45^{o} crack, where the specimen remained relatively quiet during the early stage but later exhibited high-energy acoustic activity together with clear shear-coupled localization. The third behavior was an abrupt fracture-dominated response, observed in the 90/90/90 specimens, where the main acoustic energy release was concentrated in a short time interval and coincided with rapid localization or final fracture. These results show that crack propagation cannot be explained only by the initial crack angle or only by the laminate stacking sequence; instead, it is controlled by their combined influence on load transfer, strain redistribution, and damage evolution.

Overall, this thesis provides a unified experimental and numerical framework for crack propagation monitoring in pre-cracked composite laminates. The SEA-assisted DIC contribution improves the reliability of full-field localization by stabilizing the strain and gradient reconstruction process. The multi-instrument contribution improves the physical interpretation of crack propagation by linking spatial deformation patterns, temporal AE activity, and local strain response. The integration of these two contributions is the central outcome of the thesis. It demonstrates that reliable crack monitoring in composite laminates requires both numerically stable full-field localization and physically consistent multi-sensor interpretation.

The findings of this thesis contribute to the broader field of structural health monitoring and experimental damage mechanics by providing a data-driven, model-independent, and experimentally validated approach for identifying crack-sensitive regions and interpreting crack-growth stages. The proposed framework is particularly useful for composite structures where damage evolution is anisotropic, localized, and strongly dependent on ply architecture. By distinguishing progressive crack growth, delayed high-energy propagation, and abrupt fracture-dominated transitions, the thesis establishes a more comprehensive basis for evaluating damage evolution in pre-cracked laminated composites.

Future work should extend the proposed framework to larger specimen sets, repeated

tests, additional stacking sequences, and more complex loading conditions such as fatigue, impact, and mixed-mode loading. The physical interpretation of AE populations could be strengthened by integrating AE source localization, high-speed imaging, post-mortem microscopy, X-ray micro-computed tomography, or three-dimensional DIC. In addition, future studies may develop more detailed crack-path overlap metrics when reliable DIC data remain available up to complete fracture. Such developments would further improve the connection between full-field deformation, acoustic damage activity, and underlying micro-damage mechanisms, ultimately supporting the application of the proposed framework to more complex composite structural components.

BIBLIOGRAPHY

Adams, D. F., Carlsson, L. A., & Pipes, R. B. (2003). *Experimental characterization of advanced composite materials* (3rd). CRC Press.

Ahmadi, H., Aghdam, M. M., & Li, S. (2022). A computational study about the effects of ply cracking and delaminations on the effective thermo-elastic constants of damaged composite laminates. *International Journal of Damage Mechanics*, *31*(8), 1186–1229.

Ajovalasit, A. (2010). Advances in strain gauge measurement on composite materials. *Strain*, *46*(4), 313–325.

Ajovalasit, A., & Pitarresi, G. (2011). Strain measurement on composites: Effects due to strain gauge misalignment. *Strain*, *47*(s1), e84–e92.

Ali, H. Q., Tabrizi, I. E., Khan, R. M. A., & Yildiz, M. (2019). Microscopic analysis of failure in woven carbon fabric laminates coupled with digital image correlation and acoustic emission. *Composite Structures*, *230*, 111515.

Alimirzaei, S., Ahmadi Najafabadi, M., Nikbakht, A., & Pahlavan, L. (2022). Damage mechanism characterization of $\pm 35^\circ$ and $\pm 55^\circ$ fw composite tubes using acoustic emission method. *International Journal of Damage Mechanics*, *31*(8), 1230–1253.

Andraju, L. B., & Raju, G. (2023). Damage characterization of cfrp laminates using acoustic emission and digital image correlation: Clustering, damage identification and classification. *Engineering Fracture Mechanics*, *277*, 108993.

Arena, M., Viscardi, M., Barra, G., Guadagno, L., & Vertuccio, L. (2020). Strain state detection in composite structures: Review and new challenges. *Journal of Composites Science*, *4*(2), 60.

Askes, H., & Sluys, L. J. (2002). Explicit and implicit gradient series in damage mechanics. *European Journal of Mechanics - A/Solids*, *21*(3), 379–390.

Assarar, M., Bentahar, M., & El Mahi, A. (2015). Monitoring of damage mechanisms in sandwich composite material using acoustic emission. *International Journal of Damage Mechanics*, *24*(6), 787–804.

Barbero, E. J., & De Vivo, L. (2001). A constitutive model for elastic damage in fiber-reinforced pmc laminae. *International Journal of Damage Mechanics*, *10*(1), 73–93.

Becker, T. H., Mostafavi, M., Tait, R. B., & Marrow, T. J. (2012). An approach to calculate the J-integral by digital image correlation displacement field measurement. *Fatigue & Fracture of Engineering Materials & Structures*, *35*(10), 971–984.

Bilgin, M. H., & Kefal, A. (2025). Deformation reconstruction and crack monitoring in composites using a novel particle inverse method with experimental validation. *Mechanics of Advanced Materials and Structures*. https://doi.org/10.1080/15376494.2025.2581832

Bohse, J. (2000). Acoustic emission characteristics of micro-failure processes in polymer blends and composites. *Composites Science and Technology*, *60*(8), 1213–1226.

Bruck, H. A., McNeill, S. R., Sutton, M. A., & Peters, W. H. (1989). Digital image correlation using Newton-Raphson method of partial differential correction. *Experimental Mechanics*, *29*(3), 261–267.

Brunbauer, J., & Pinter, G. (2014). On the strain measurement and stiffness calculation of carbon fiber reinforced composites under quasi-static tensile and tension-tension fatigue loads. *Polymer Testing*, *40*, 256–264.

Bussiba, A., Kupiec, M., Ifergane, S., Piat, R., & Böhlke, T. (2008). Damage evolution and fracture events sequence in various composites by acoustic emission technique. *Composites Science and Technology*, *68*(5), 1144–1155.

Calvo, J. V., Feito, N., Miguélez, M. H., & Giner, E. (2022). Modeling the delamination failure under compressive loads in cfrp laminates based on digital image correlation analysis. *Composite Structures*, *287*, 115265.

Camanho, P. P., & Matthews, F. L. (1999). A progressive damage model for mechanically fastened joints in composite laminates. *Journal of Composite Materials*, *33*(24), 2248–2280.

Caminero, M. A., Lopez-Pedrosa, M., Pinna, C., & Soutis, C. (2013). Damage monitoring and analysis of composite laminates with an open hole and adhesively bonded repairs using digital image correlation. *Composites Part B: Engineering*, *53*, 76–91.

Chang, F. K., & Chang, K. Y. (1987). A progressive damage model for laminated composites containing stress concentrations. *Journal of Composite Materials*, *21*(9), 834–855.

Chu, T. C., Ranson, W. F., Sutton, M. A., & Peters, W. H. (1985). Applications of digital-image-correlation techniques to experimental mechanics. *Experimental Mechanics*, *25*(3), 232–244.

Dai, X., Yang, F., Chen, Z., Shao, X., & He, X. (2015). Strain field estimation based on digital image correlation and radial basis function. *Optics and Lasers in Engineering*, *65*, 64–72.

Dally, J. W., & Riley, W. F. (2005). *Experimental stress analysis* (4th). College House Enterprises.

Daniel, I. M., & Ishai, O. (2006). *Engineering mechanics of composite materials* (2nd). Oxford University Press.

de Borst, R., Pamin, J., Peerlings, R. H. J., & Sluys, L. J. (1995). On gradient-enhanced damage and plasticity models for failure in quasi-brittle and frictional materials. *Computational Mechanics*, *17*(1-2), 130–141.

de Groot, P. J., Wijnen, P. A. M., & Janssen, R. B. F. (1995). Real-time frequency determination of acoustic emission for different fracture mechanisms in carbon/epoxy composites. *Composites Science and Technology*, *55*(4), 405–412.

del Rey Castillo, E., Henry, R., Griffith, M. C., Ingham, J. M., & Allen, T. (2019). Digital image correlation for measurement of strains and displacements in coarse, low volume-fraction frp composites used in civil infrastructure. *Composite Structures*, *212*, 43–57.

Farrar, C. R., & Worden, K. (2007). An introduction to structural health monitoring. *Philosophical Transactions of the Royal Society A*, *365*(1851), 303–315.

Flament, C., Salvia, M., Berthel, B., & Crosland, G. (2016). Local strain and damage measurements on a composite with digital image correlation and acoustic emission. *Journal of Composite Materials*, *50*(14), 1989–1996.

Gholizadeh, S. (2016). A review of non-destructive testing methods of composite materials. *Procedia Structural Integrity*, *1*, 50–57.

Godin, N., Huguet, S., & Gaertner, R. (2005). Integration of the kohonen's self-organising map and k-means algorithm for the segmentation of ae data collected during tensile tests on cross-ply composites. *NDT & E International*, *38*(4), 299–309.

Godin, N., Huguet, S., Gaertner, R., & Salmon, L. (2004). Clustering of acoustic emission signals collected during tensile tests on unidirectional glass/polyester composite using supervised and unsupervised classifiers. *NDT & E International*, *37*(4), 253–264.

Goidescu, C., Welemane, H., Garnier, C., Fazzini, M., Brault, R., Péronnet, E., & Mistou, S. (2013). Damage investigation in cfrp composites using full-field measurement techniques: Combination of digital image stereo-correlation, infrared thermography and x-ray tomography. *Composites Part B: Engineering*, *48*, 95–105.

Grediac, M. (2004). The use of full-field measurement methods in composite material characterization: Interest and limitations. *Composites Part A: Applied Science and Manufacturing*, *35*(7-8), 751–761.

Greenhalgh, E. S. (2009). *Failure analysis and fractography of polymer composites*. Woodhead Publishing.

Grosse, C. U., & Ohtsu, M. (2008). *Acoustic emission testing*. Springer.

Groth, C., Chiappa, A., Porziani, S., Biancolini, M. E., Marotta, E., & Salvini, P. (2022). A post-processing method based on radial basis functions for the fast

retrieval of the strain field in digital image correlation methods. *Materials*, *15*(22), 7936.

Güemes, A., Fernández-López, A., Pozo, A. R., & Sierra-Pérez, J. (2020). Structural health monitoring for advanced composite structures: A review. *Journal of Composites Science*, *4*(1), 13.

Gutkin, R., Green, C. J., Vangrattanachai, S., Pinho, S. T., Robinson, P., & Curtis, P. T. (2011). On acoustic emission for failure investigation in cfrp: Pattern recognition and peak frequency analyses. *Mechanical Systems and Signal Processing*, *25*(4), 1393–1407.

Habibi, M., & Laperrière, L. (2023). Combining digital image correlation and acoustic emission to characterize the flexural behavior of flax biocomposites. *Applied Mechanics*, *4*(1), 371–388.

Hamdi, K., Moreau, G., & Aboura, Z. (2021). Digital image correlation, acoustic emission and in-situ microscopy in order to understand composite compression damage behaviour. *Composite Structures*, *258*, 113424.

Han, W. Q., et al. (2020). Damage evolution analysis of open-hole tensile laminated composites using a progress damage model verified by ae and dic. *Composite Structures*, *247*, 112452.

Hashin, Z. (1980). Failure criteria for unidirectional fiber composites. *Journal of Applied Mechanics*, *47*(2), 329–334.

Herakovich, C. T. (1998). *Mechanics of fibrous composites*. Wiley.

Hild, F., & Roux, S. (2006). Digital image correlation: From displacement measurement to identification of elastic properties — a review. *Strain*, *42*(2), 69–80.

Hoffmann, K. (1989). *An introduction to measurements using strain gages*. Hottinger Baldwin Messtechnik.

Holmes, J., Sommacal, S., Das, R., Stachurski, Z., & Compston, P. (2023). Digital image and volume correlation for deformation and damage characterisation of fibre-reinforced composites: A review. *Composite Structures*, *315*, 116994.

Huguet, S., Godin, N., Gaertner, R., Salmon, L., & Villard, D. (2002). Use of acoustic emission to identify damage modes in glass fiber reinforced polyester. *Composites Science and Technology*, *62*(10-11), 1433–1444.

Hull, D., & Clyne, T. W. (1996). *An introduction to composite materials* (2nd). Cambridge University Press.

International Digital Image Correlation Society, Jones, E. M. C., & Iadicola, M. A. (2018). A good practices guide for digital image correlation.

Janeliukstis, R., & Chen, X. (2021). Review of digital image correlation application to large-scale composite structure testing. *Composite Structures*, *271*, 114143.

Jones, R. M. (1999). *Mechanics of composite materials* (2nd). Taylor & Francis.

Kefal, A., Bilgin, M. H., & Kendibilir, A. (2024). Particle inverse method for full-field displacement and crack propagation monitoring from discrete sensor measurements. *Computer Methods in Applied Mechanics and Engineering*, *432*, 117369.

Kefal, A., Tabrizi, I. E., Yildiz, M., & Tessler, A. (2021). A smoothed iFEM approach for efficient shape-sensing applications: Numerical and experimental validation on composite structures. *Mechanical Systems and Signal Processing*, *152*, 107486.

Lagattu, F., Brillaud, J., & Lafarie-Frenot, M. C. (2004). High strain gradient measurements by using digital image correlation technique. *Materials Characterization*, *53*(1), 17–28.

Lapczyk, I., & Hurtado, J. A. (2007). Progressive damage modeling in fiber-reinforced materials. *Composites Part A: Applied Science and Manufacturing*, *38*(11), 2333–2341.

Li, S., Wang, M., Jeanmeure, L. F. C., & Zhao, X. (2019). Damage related material constants in continuum damage mechanics for unidirectional composites with matrix cracks. *International Journal of Damage Mechanics*, *28*(5), 690–707.

McCrory, J. P., Al-Jumaili, S. K., Crivelli, D., Pearson, M. R., Eaton, M. J., Featherston, C. A., Guagliano, M., Holford, K. M., & Pullin, R. (2015). Damage classification in carbon fiber composites using acoustic emission: A comparison of three techniques. *Composites Part B: Engineering*, *68*, 424–430.

McNeill, S. R., Peters, W. H., & Sutton, M. A. (1987). Estimation of stress intensity factor by digital image correlation. *Engineering Fracture Mechanics*, *28*(1), 101–112.

Mehdikhani, M., Steensels, E., Standaert, A., Vallons, K. A. M., Gorbatikh, L., & Lomov, S. V. (2018). Multi-scale digital image correlation for detection and quantification of matrix cracks in carbon fiber composite laminates in the absence and presence of voids controlled by the cure cycle. *Composites Part B: Engineering*, *154*, 138–147.

Memmolo, V., Monaco, E., Boffa, N. D., Maio, L., & Ricci, F. (2018). Guided wave propagation and scattering for structural health monitoring of stiffened composites. *Composite Structures*, *184*, 568–580.

Miller, R. K., Hill, E. v. K., & Moore, P. O. (2005). *Nondestructive testing handbook, vol. 6: Acoustic emission testing*. ASNT.

Nuismer, R. J., & Whitney, J. M. (1975). Uniaxial failure of composite laminates containing stress concentrations. In *Fracture mechanics of composites* (pp. 117–142, Vol. 593). ASTM International.

Okabe, T., Onodera, S., Kumagai, Y., & Nagumo, Y. (2018). Continuum damage mechanics modeling of composite laminates including transverse cracks. *International Journal of Damage Mechanics*, *27*(6), 877–895.

Onodera, S., & Okabe, T. (2020). Analytical model for determining effective stiffness and mechanical behavior of polymer matrix composite laminates using continuum damage mechanics. *International Journal of Damage Mechanics*, *29*(10), 1512–1542.

Öz, F. E., Ersoy, N., & Lomov, S. V. (2017). Do high frequency acoustic emission events always represent fiber failure in cfrp laminates? *Composites Part A: Applied Science and Manufacturing*, *103*, 230–235.

Öz, F. E., Ersoy, N., Mehdikhani, M., & Lomov, S. V. (2018). Multi-instrument in-situ damage monitoring in quasi-isotropic cfrp laminates under tension. *Composite Structures*, *196*, 163–180.

Oz, F. E., Mehdikhani, M., Ersoy, N., & Lomov, S. V. (2020). In-situ imaging of inter- and intra-laminar damage in open-hole tension tests of carbon fibre-reinforced composites. *Composite Structures*, *244*, 112302.

Özaslan, E., Yetgin, A., Acar, B., & Güler, M. A. (2021). Damage mode identification of open hole composite laminates based on acoustic emission and digital image correlation methods. *Composite Structures*, *274*, 114299.

Pan, B., Qian, K., Xie, H., & Asundi, A. (2009). Two-dimensional digital image correlation for in-plane displacement and strain measurement: A review. *Measurement Science and Technology*, *20*(6), 062001.

Pan, B., Xie, H., Guo, Z., & Hua, T. (2007). Full-field strain measurement using a two-dimensional Savitzky-Golay digital differentiator in digital image correlation. *Optical Engineering*, *46*(3), 033601.

Peerlings, R. H. J., de Borst, R., Brekelmans, W. A. M., & de Vree, J. H. P. (1996). Gradient-enhanced damage for quasi-brittle materials. *International Journal for Numerical Methods in Engineering*, *39*(19), 3391–3403.

Peters, W. H., & Ranson, W. F. (1982). Digital imaging techniques in experimental stress analysis. *Optical Engineering*, *21*(3), 427–431.

Pierron, F., Green, B., Wisnom, M. R., & Hallett, S. R. (2007a). Full-field assessment of the damage process of laminated composite open-hole tensile specimens. Part I: Methodology. *Composites Part A: Applied Science and Manufacturing*, *38*(11), 2307–2320.

Pierron, F., Green, B., Wisnom, M. R., & Hallett, S. R. (2007b). Full-field assessment of the damage process of laminated composite open-hole tensile specimens. Part II: Experimental results. *Composites Part A: Applied Science and Manufacturing*, *38*(11), 2321–2332.

Puck, A., & Schürmann, H. (1998). Failure analysis of frp laminates by means of physically based phenomenological models. *Composites Science and Technology*, *58*(7), 1045–1067.

Purslow, D. (1986). Matrix fractography of fiber-reinforced epoxy composites. *Composites*, *17*(4), 289–303.

Qiu, J., et al. (2022). Strain induced crack initiation and the subsequent crack propagation of fiber-reinforced resin composites. *Composites Part A: Applied Science and Manufacturing*, *155*, 106836.

Ramirez-Jimenez, C. R., Papadakis, N., Reynolds, N., Gan, T. H., Purnell, P., & Pharaoh, M. (2004). Identification of failure modes in glass/polypropylene composites by means of the primary frequency content of the acoustic emission event. *Composites Science and Technology*, *64*(12), 1819–1827.

Riggs, H. R., Tessler, A., & Chu, H. (1997). C1-continuous stress recovery in finite element analysis. *Computer Methods in Applied Mechanics and Engineering*, *143*(3-4), 299–316.

Rocha, H., Semprimoschnig, C., & Nunes, J. P. (2021). Sensors for process and structural health monitoring of aerospace composites: A review. *Engineering Structures*, *237*, 112231.

Romhány, G., Czigány, T., & Karger-Kocsis, J. (2017). Failure assessment and evaluation of damage development and crack growth in polymer composites via localization of acoustic emission events: A review. *Polymer Reviews*, *57*(3), 397–439.

Rouwane, A., et al. (2022). Architecture-driven digital image correlation technique assisted with weak regularization. *International Journal of Solids and Structures*, *234-235*, 111223.

Saeedifar, M., & Zarouchas, D. (2020). Damage characterization of laminated composites using acoustic emission: A review. *Composites Part B: Engineering*, *195*, 108039.

Sause, M. G. R. (2016). *In situ monitoring of fiber-reinforced composites: Theory, basic concepts, methods, and applications*. Springer.

Soutis, C. (2005). Fibre reinforced composites in aircraft construction. *Progress in Aerospace Sciences*, *41*(3-4), 143–151.

Standard test method for tensile properties of polymer matrix composite materials (Standard No. D3039/D3039M). (n.d.). ASTM International.

Su, Z., Ye, L., & Lu, Y. (2006). Guided lamb waves for identification of damage in composite structures: A review. *Journal of Sound and Vibration*, *295*(3-5), 753–780.

Sutton, M. A., Orteu, J.-J., & Schreier, H. W. (2009). *Image correlation for shape, motion and deformation measurements: Basic concepts, theory and applications*. Springer.

Sutton, M. A., Wolters, W. J., Peters, W. H., Ranson, W. F., & McNeill, S. R. (1983). Determination of displacements using an improved digital correlation method. *Image and Vision Computing*, *1*(3), 133–139.

Tabrizi, I. E., Kefal, A., Zanjani, J. S. M., Akalin, C., & Yildiz, M. (2019). Experimental and numerical investigation on fracture behavior of glass/carbon fiber hybrid composites using acoustic emission method and refined zigzag theory. *Composite Structures*, *223*, 110971.

Tabrizi, I. E., Kefal, A., Zanjani, J. S. M., & Yildiz, M. (2022). Damage growth and failure detection in hybrid fiber composites using experimental in-situ optical strain measurements and smoothing element analysis. *International Journal of Damage Mechanics*, *31*(4), 479–507.

Tabrizi, I. E., Khan, R. M. A., Massarwa, E., Zanjani, J. S. M., Ali, H. Q., Demir, E., & Yildiz, M. (2019). Determining tab material for tensile test of cfrp laminates with combined usage of digital image correlation and acoustic emission techniques. *Composites Part A: Applied Science and Manufacturing*, *127*, 105623.

Talreja, R. (1994). *Damage mechanics of composite materials*. Elsevier.

Talreja, R., & Singh, C. V. (2012). *Damage and failure of composite materials*. Cambridge University Press.

Tan, S. C. (1991). A progressive failure model for composite laminates containing openings. *Journal of Composite Materials*, *25*(5), 556–577.

Tessler, A., Riggs, H. R., & Dambach, M. (1999). A novel four-node quadrilateral smoothing element for stress enhancement and error estimation. *International Journal for Numerical Methods in Engineering*, *44*(10), 1527–1558.

Tessler, A., Riggs, H. R., Freese, C. E., & Cook, G. M. (1998). An improved variational method for finite element stress recovery and a posteriori error estimation. *Computer Methods in Applied Mechanics and Engineering*, *155*(1-2), 15–30.

Tessler, A., Riggs, H. R., & Macy, S. C. (1994). A variational method for finite element stress recovery and error estimation. *Computer Methods in Applied Mechanics and Engineering*, *111*(3-4), 369–382.

Tuttle, M. E., & Brinson, H. F. (1984). Resistance-foil strain-gage technology as applied to composite materials. *Experimental Mechanics*, *24*(1), 54–65.

Ubaid, J., Kashfuddoja, M., & Ramji, M. (2014). Strength prediction and progressive failure analysis of carbon fiber reinforced polymer laminate with multiple interacting holes involving three-dimensional finite element analysis and dig-

ital image correlation. *International Journal of Damage Mechanics*, *23*(5), 609–635.

Wang, B., Zhong, S., Lee, T.-L., Fancey, K. S., & Mi, J. (2020). Non-destructive testing and evaluation of composite materials/structures: A state-of-the-art review. *Advances in Mechanical Engineering*, *12*(4).

Wang, M., He, M., Liang, Z., Wu, D., Wang, Y., Qing, X., & Wang, Y. (2023). Fatigue damage monitoring of composite laminates based on acoustic emission and digital image correlation techniques. *Composite Structures*, *321*, 117239.

Wang, Z., Zhu, P., Liu, L., & Zhou, X. (2024). An accurate and robust strain field smoothing method based on polynomial fitting and anisotropic diffusion in digital image correlation. *Measurement*, *225*, 113947.

Wattrisse, B., Chrysochoos, A., Muracciole, J. M., & Némoz-Gaillard, M. (2001). Analysis of strain localization during tensile tests by digital image correlation. *Experimental Mechanics*, *41*(1), 29–39.

Whitney, J. M., & Nuismer, R. J. (1974). Stress fracture criteria for laminated composites containing stress concentrations. *Journal of Composite Materials*, *8*(3), 253–265.

Willberry, J. O., et al. (2020). Structural health monitoring using fibre optic acoustic emission sensors: A review. *Sensors*, *20*(22), 6369.

Wisnom, M. R. (2012). The role of delamination in failure of fibre-reinforced composites. *Philosophical Transactions of the Royal Society A*, *370*(1965), 1850–1870.

Yuan, Z., Niu, M. Q., Zang, J., Ma, H., Huang, L., Zhang, Y., & Chen, L. Q. (2025). Integration of acoustic emission and digital image correlation for damage of composite panels with different layup sequences. *Applied Acoustics*, *231*, 110476.

Zhu, M., Gorbatikh, L., Fonteyn, S., et al. (2020). Digital image correlation assisted characterization of Mode I fatigue delamination in composites. *Composite Structures*, *253*, 112746.